Novel Direct Field and Torque Control of Six-Phase Induction Machine with Special Phase Current Waveform

Yong-le Ai

Dissertation presented for the degree of Doctor of Philosophy in

Electrical Engineering at the University of Stellenbosch

Promoter:

Prof. Maarten J. Kamper

August 2006

Declaration

The work presented in this dissertation was carried out in the Department of the Electrical and Electronic Engineering University of Stellenbosch, during the period March 2002 to January 2006 under the supervision of Prof. Maarten J. Kamper.

The author wishes to declare that, except for commonly understood and accepted ideas, or where specific references in made to the work of other, the work in this dissertation is his own and includes nothing which is the outcome of other work done in collaboration. It has not been submitted, in part or in whole, to any university for a degree, diploma or other qualification.

Yong-le Ai
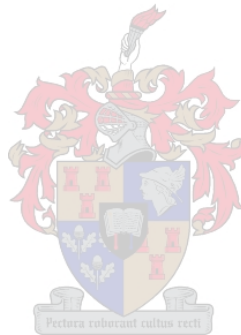
Signature   Date:

Abstract

This study focuses on the drive control system of a novel direct field and torque current control applied to a six-phase induction motor. Special phase current waveforms that make it possible to have separate field and torque windings and currents in the motor are proposed. In this thesis the control of these field and torque windings to control directly the flux and torque of the motor is investigated.

With the special phase current waveforms the performance of the six-phase induction motor is evaluated through theoretical and finite element analysis. In the analysis the air gap resultant field intensity and flux density produced by the stator field, stator torque and rotor currents are investigated. It is shown that with the special current waveforms a quasi-square shaped, smooth rotating air gap flux density is generated. This smooth rotating flux is important for proper induction motor operation.

An equation for the electromagnetic torque is derived and used in the theoretical calculations. The ease of the torque performance calculations is conspicuous. An approximate magnetic circuit calculation method is developed to calculate the air gap flux density versus field current relationship taking magnetic saturation into account. The air gap MMF harmonics and the per phase self and mutual inductances are analysed and calculated using, amongst other things, winding functions. In the finite element analysis specific attention is given to the MMF balanced condition (zero quadrature flux condition) in the motor and the development of a per phase equivalent model.

The drive system's performance with the proposed direct control technique is verified by a developed Matlab simulation model and measurements on a small (2 kW) two-pole, six-phase induction motor drive under digital hysteresis current control. It is shown in the thesis that the calculated results from theoretical derived equations are in good agreement with finite element and measured results. This is particularly the case for the formulas of the MMF balanced constant (zero quadrature flux linkage constant) used in the control software. The results of the simulated and measured linear relationship between the torque and torque current show that MMF balance is maintained in the motor by the drive controller independent of the load condition. The direct control of the torque also explains the good measured dynamic performance found for the proposed drive.

Sinopsis

Die studie fokus op die aandryf beheerstelsel van 'n nuwe direkte veld en draaimoment stroombeheer van 'n ses-fase induksiemotor. Spesiale fase stroomgolfvorms wat dit moontlik maak om aparte veld en draaimoment wikkelinge en strome in die motor te hê, word voorgestel. In hierdie tesis word die beheer van hierdie veld en draaimoment wikkelinge om direk die vloed en draaimoment van die motor te beheer ondersoek.

Met die spesiale fase stroomgolfvorms word die werkverrigting van die ses-fase induksiemotor deur teoretiese en eindige element analise geëvalueer. In die analise word die luggaping veldintensiteit en vloeddigtheid wat deur die statorveld, stator-draaimoment en rotor strome opgewek word, ondersoek. Daar word getoon dat met die spesiale stroomgolfvorms 'n kwasi-vierkant-golfvormige, glad-roterende luggaping vloeddigtheid opgewek word. Die glad-roterende vloed is belangrik vir korrekte induksiemotor werking.
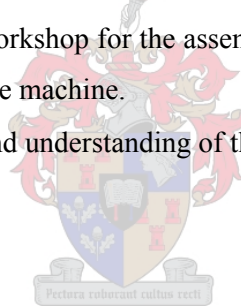
'n Vergelyking vir die elektromagnetiese draaimoment word afgelei en in die teoretiese berekeninge gebruik. Die eenvoudigheid van die draaimoment berekeninge is opvallend. 'n Benaderde magnetiese stroombaan berekeningsmetode is ontwikkel om die verhouding van die luggaping vloeddigtheid teenoor veldstroom te bereken; hierdie metode neem magnetiese versadiging in ag. Die luggaping MMK harmonieke en die per fase self en wedersydse induktansies word geanaliseer en bereken deur gebruik te maak van onder andere, wikkelingsfunksies. In die eindige element analise word spesifiek aandag gegee aan die MMK gebalanseerde toestand (zero dwarsvloed toestand) in die motor en die ontwikkeling van 'n per fase ekwivalente model.

Die aandryfstelsel se werkverrigting met die voorgestelde direkte beheertegniek word bevestig deur 'n Matlab simulasie model wat ontwikkel is en deur metings wat op 'n klein (2 kW) twee-pool, ses-fase induksiemotor gedoen is met digitale histerese stroombeheer. Daar word in die tesis getoon dat die berekende resultate van die teoretiese afgeleide vergelykings ooreenstem met die eindige element en gemete resultate. Dit is spesifiek die geval vir die vergelykings van die vloedkoppeling balanseringskonstante (zero dwarsvloed vloed-omsluitingskontante) wat gebruik is in die beheer sagteware. Die resultate van die gesimuleerde en gemete lineêre verhouding tussen die draaimoment en die stator draaimomentstroom bewys dat MMK balans in stand gehou word in die motor deur die aandryfbeheerder, onafhanklik van die lastoestand. Die direkte beheer van die draaimoment verduidelik ook die goeie gemete dinamiese werksverrigting wat verkry is met die voorgestelde aandrywing.

Acknowledgements

I would like to express my sincere appreciation to:

Table of Contents

Glossary of Symbols

Symbol	Description	Unit
α	angle displacement of the rotor phases	[rad]
B	Flux density	[T]
B_m	peak value of the sinusoidal of air gap flux density	[T]
β	angle displacement of the stator phases	[rad]
β_{eq}	equivalent viscous friction constant of the load motor	[Nm/(rad/s)]
e_j	stator or rotor per phase induced voltage	[V]
e_{mj}	stator per phase mutual induced voltage	[V]
E	rotor per phase induced voltage	[V]
F_f	field MMF	[At]
F_t	torque MMF	[At]
F_r	rotor MMF	[At]
H_{tf}	resultant field intensity produced by field currents	[At/m]
H_{tt}	resultant field intensity produced by torque currents	[At/m]
H_{tr}	resultant field intensity produced by rotor currents	[At/m]
I_f	field winding current in the dc motor	[A]
I_c	compensating winding current in the dc motor	[A]
I_a	armature winding current in the dc motor	[A]
I_F	field current amplitude	[A]
I_T	torque current amplitude	[A]
$\vec{i}_s$	stator current space phasor	[A]
$\vec{i}'_r$	rotor current space phasor	[A]
i_{ds}, i_{qs}	stator d-axis and q-axis current component in synchronous frame	[A]
i_{dr}, i_{qr}	rotor d-axis and q-axis current component in synchronous frame	[A]
J	polar moment of inertia	[kg m^2]
k	ratio of the slip speed over the torque current	[(rad/s)/A]
k_{ej}	mutual voltage constant	[V/(rad/s)]
k_{rj}	slotted air gap voltage constant	[V/(rad/s)]
k_c	Carter's factor	
k_T	torque coefficient	[Nm/A]
l	axial length of the stator/rotor stack	[m]
l'	length of rotor per phase wire	[m]
l_g	air gap length	[m]
L_s, L_m, L_r	stator, air gap and rotor inductance	[H]

m	number of the phases	
N_s	number turns of stator per phase	
N_r	number turns of rotor per phase	
p	number of pole pairs	
r_s	Stator per phase resistance	[Ω]
r_{eq}	rotor per phase resistance	[Ω]
T_e	electromagnetic torque	[Nm]
T_L	Load torque	[Nm]
T_r	rotor time constant	[s]
μ_0	absolute permeability ($4\pi\,10^{-7}$)	[H/m]
v_{s1}	stator group 1 phase voltage	[V]
v_{s2}	stator group 2 phase voltage	[V]
λ_f	excitation flux linkage	[Wb-turn]
$\lambda_s, \lambda'_m, \lambda'_r$	stator, air gap and rotor flux linkage	[Wb-turn]
φ_f	field flux	[Wb]
φ_a	armature flux	[Wb]
X_{ll}	stator leakage reactance	[Ω]
X_{lm}	stator mutual leakage reactance	[Ω]
X_{lr}	rotor leakage reactance	[Ω]
X_m	stator magnetizing reactance	[Ω]
$\omega_e, \omega_{sl}, \omega_r$	synchronous speed, slip speed and rotor speed	[rad/s]

Abbreviations

MMF	Magnetomotive Force
EMF	Electromotive Force
DSP	Digital Signal Processor
VSI	Voltage Source Inverter
CSI	Current Source Inverter
dc	Direct Current
ac	Alternative Current
IDCM	Induction dc Motor
FE	Finite Element
AMC	Approximate Magnetic Circuit
VSD	Variable Speed Drive
BDCM	Brushless dc Motor

DTC	Direct Torque Control
HPO	High Phase Order
FOC	Field Orientation Control
FPGA	Field Programmable Gate Array
IGBT	Insulated Gate Bipolar Transistor
PWM	Pulse Width Modulation
PI	Proportional Integral
IPM	Intelligent Power Module

List of Figures

List of Tables

1.   INTRODUCTION

Amongst the many types of electrical motors, induction motors still enjoy the same popularity as they did a century ago. At least 90% of industrial drive systems employs induction motors [1]. Why is the induction motor still the favourite for electromechanical energy conversion in industry today? Several factors that include robustness, reliability, low cost and low maintenance have made them popular for industrial application when compared to dc and other ac machines.

1.1   Evaluation of variable speed drives

The basic function of a variable speed drive (VSD) is to control the flow of energy from the mains supply to the mechanical system process. Energy is supplied to the mechanical system through the motor shaft. Two physical quantities are associated with the shaft namely *torque* and *speed*. In practice, either one of them is controlled and referred to as torque control or speed control. When the VSD operates in torque control mode, the load determines the speed. Likewise, when operated in speed control mode the torque is determined by the load [2, 3].

1.1.1   *Conventional motor drives*

Initially, direct current (dc) motor drives [4] were used for variable speed control because the flux and torque of dc motors can be controlled independently, and the electromagnetic torque is linearly proportional to the armature current. Thus desirable speed or position output performance can easily be achieved. However, dc drives have certain disadvantages due to the existence of the commutators and brushes [5, 6]. Firstly, the mechanical commutation brushes require periodical maintenance; secondly, owing to the sparks created by the commutators, dc motors cannot be used in potentially explosive environments. Finally, the mechanical contacts of the commutators and brushes limit high speed operation. These problems can be overcome by the application of ac motors, which have simple and rugged structures. Their small dimensions compared to dc motors allow ac motors to be designed with substantially higher output rating, low weight and low rotating mass. Hence, much attention was paid to ac variable speed drives to emulate the performance of the dc drive. The ac motor variable speed drive has experienced two major development strategies, namely, scalar control and vector control.

Scalar-control [7] is used in low-cost and low-performance variable speed drives. This control method does not guarantee good dynamic performance, because transient states of the motor are not considered in the control algorithm. Though some efforts were made to improve the scalar-control performance, the effect is still unsatisfactory. So the vector-control theory was introduced by Hasse and Blaschke [8] in order to achieve the performance comparable to that of dc drives. The goal of this method is to make the induction motor emulate the dc motor control by transforming the stator currents to a specific coordinate system where one coordinate is related to the torque production and the other to the rotor flux [5].

Vector control has the major advantage that good dynamic performance is obtained from the drive. The main disadvantage, however, of vector control is the complex computation required to perform the coordinate transformation.

The fast progress in the development of ac motor drives in the past two decades was mainly due to the development of power electronic devices, powerful and inexpensive microprocessors and modern ac motor control technologies. These modern control techniques include, amongst other things, direct torque control (DTC) [9, 10], fuzzy logic control [11] and neural network control [12, 13].

1.1.2   *Multiphase induction motor drives*
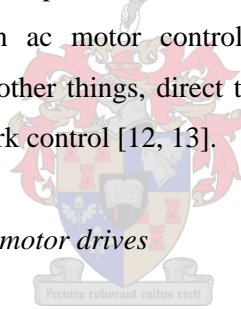
Another direction in ac motor drives, which has been developed recently is the use of multiphase drives where the number of stator phases is more than three. The type of motor used in the multiphase drive is referred to as a high phase order (HPO) motor. The power required from the motor as well as the voltage and current limits of the switching devices led to the emergence of the HPO motor.

Ward and Harer [14] investigated the performance of a five-phase, ten-step voltage-fed induction motor drive system. The dominant torque ripple frequency in this system was the tenth harmonic. Its amplitude is one-third of that of the sixth harmonic produced torque in the three-phase motor drive systems. However, the line current was rich in third and higher order harmonics which resulted in higher motor losses.

Many scholars have studied multiphase drives with dual three-phase motors. The results of these research show that the output torque of these motors is superior to that of normal three-phase motors. However, the 5th and 7th current harmonics are far more substantial in

these multiphase drives. These harmonics generate additional losses in the machine resulting in the increase of the size and cost of both machine and inverter. In order to reduce these harmonics, a variety of approaches in current harmonic minimization through motor design and control were proposed [17 – 26].

Toliyat *et a*l [29, 30] investigated a direct torque control method for 5-phase VSI induction machine drives. The conclusion is that fast torque response with low ripple torque can be obtained.

Xu *et al* [31] and Lyra *et al* [32] carried out research on the torque density improvement of respectively five and six-phase induction motors by injecting third harmonic currents and using field oriented control (FOC). The conclusion drawn from this research is that by injecting third harmonic currents into the machine the production of the electromagnetic torque of the drive can be improved.

Researchers [19, 28] demonstrated that HPO drives possess many advantages over conventional three-phase motor drives. These advantages include the reduction of the amplitude and increase of the frequency of the torque pulsation, the reduction of rotor harmonic currents, the reduction of the current per phase without increasing the voltage per phase and the provision of a higher reliability.

1.2   Problem statement
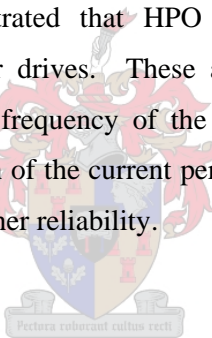
It is clear from literature that vector control of multi-phase induction motor drives is quite complex to implement; the vector control needs complex coordinate transformations and accurate flux linkage estimators. To address this problem a novel current control scheme for six-phase induction motor drives is proposed. In this control scheme the six-phase induction machine is controlled by using special phase current waveforms to realize direct field and torque current control without complex coordinate transformation. These special phase current waveforms produce a rotating, near square flux density waveform in the air gap to induce square-shaped phase currents in the rotor, just like the armature phase winding current in dc motors. From a dc motor point of view, thus, this six-phase induction motor with its square-shaped flux density and rotor current waveforms is referred to in this thesis as an induction dc motor (IDCM).

The principle of the IDCM drive has, hitherto, not been proposed and investigated. Hence, there is not any published work on this drive with its special phase current waveforms. There is thus a need for in-depth research on the proposed IDCM drive system.

Regarding the IDCM drive proposed above the following work should be addressed in this thesis:

(i)   Extensively describe and analyse the operational principle of the IDCM drive.

(ii)   Investigate in all detail the per phase modelling of the IDCM for the purpose of simulation.

(iii) Show through simulation and practical measurements the torque and dynamic performance of the IDCM drive.

1.3   Approach to the problem

In this thesis the operational principle of the six-phase IDCM drive is extensively investigated through theoretical and finite element (FE) analysis. In the theoretical analysis the air gap field intensity is analysed and an electromagnetic torque formula for the IDCM is derived and used to calculate the motor torque. An approximate magnetic circuit (AMC) method is adopted to determine accurately the field current versus air gap flux density relationship of the machine; this method, thus, takes magnetic saturation into account. To determine time and space harmonics in the machine a harmonics analysis of the air gap MMF is carried out.

For the research the source code of a FE program developed at the University of Cambridge is used [33]. This FE software is adapted by the author and applied to the IDCM to investigate its performance.

The IDCM drive is investigated by simulating the whole drive system using the Matlab/simulink software package. An experimental investigation is carried out in the laboratory to determine the accuracy and validity of the torque and dynamic performance of the IDCM drive. Note that as a first study on the IDCM drive this thesis does not focus on other performance aspects of the drive like power factor, efficiency and iron losses.

1.4   Thesis layout

The layout of this thesis is briefly described as follows:

Chapter 2: Review of Motor Drive Analysis and Control

In this chapter the background knowledge of vector control and six-phase induction machine control is briefly presented.

Chapter 3: Novel Current Control Theory for Six-Phase Induction Machine

The principle and model of the IDCM drive are described in this chapter. The electromagnetic torque of the six-phase IDCM is also evaluated theoretically

Chapter 4: FE Analysis

FE software is employed to analyse the performance of the six-phase IDCM.

Chapter 5: Matlab Simulation of IDCM Drive System

A simulation model is developed in this chapter for the complete simulation of the six-phase IDCM drive. Matlab/Simulink software is used for the simulation.

Chapter 6: Experimental Evaluation

The performance of a small IDCM drive system is measured and the results are compared with calculated and simulated results.

Chapter 7: Conclusions and Recommendations

In this chapter the original work performed in this project is summarised and relevant conclusions are given. Recommendations pertaining to future research are also made.

2   REVIEW OF MOTOR DRIVE ANALYSIS AND CONTROL

In this chapter a description of the mechanism of the torque production in dc and ac motors as found in literature is presented. Three torque equations of the vector control of ac motors are derived by selecting the different reference frames. It is shown that when a special reference frame is used, which is fixed to either the rotor flux, the air gap flux or the stator flux space phasors, the expression of the electromagnetic torque contains a flux-producing current component and a torque-producing current. This description is followed by a discussion of the six-phase induction motor analysis and its vector control.

2.1   Mechanism of electromagnetic torque production

In this section the mechanism of electromagnetic torque production in dc and ac motors will be discussed. For simplicity the effects of magnetic non-linearity will be neglected. To enhance the analogy between the mechanism of torque production in dc and ac motors, the space-phasor formulation of the electromagnetic torque will be presented for both types of motors.

2.1.1   Electromagnetic torque production in dc motors

Fig. 2.1(a) shows a schematic diagram of compensated dc motors. In the stator of the dc motor there is a field winding (f) and a compensating winding (c), and in the rotor there is an armature winding (a). The current in the field winding i_f produces an excitation flux linkage λ_f. If the current i_a flows in the armature winding, the interaction of the armature current and the excitation flux-linkage will result in force acting on the conductors, as shown in Fig.2.1 (a). Since the excitation flux linkage is in space quadrature to the armature current phasor [Fig. 2.1(b)], maximum force is applied to the shaft and therefore the position of the armature winding is optimal for electromagnetic torque production.

It can be seen from Fig.2.1 that the armature winding also produces a field, which is superimposed on the field produced by the field winding, but it is in space quadrature with respect to the excitation flux. Thus the resultant field will be displaced from its optimal position. However, this effect can be cancelled by the application of the compensating winding (c), which carries current I_c equal to $-I_a$.

6
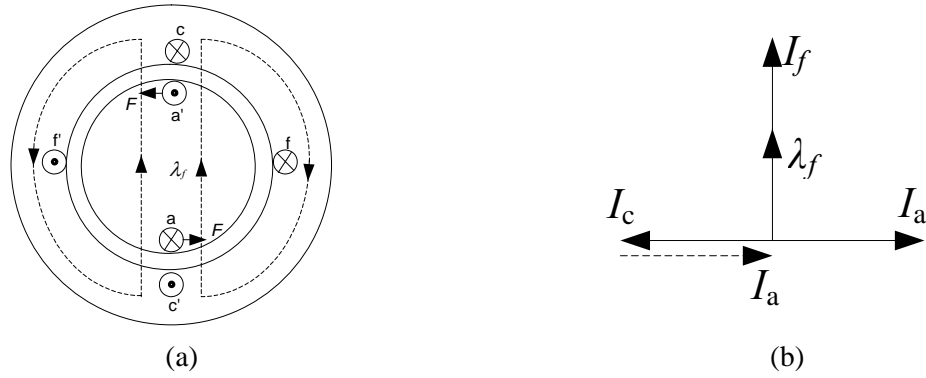
Fig. 2.1. Electromagnetic torque production in a dc motor.

The amplitudes of the space phasors of the currents in the field winding, compensating winding and armature winding, I_f, I_c, I_a and the amplitude of the space phasor of the excitation flux linkage, λ_f, are shown in Fig. 2.1(b).

The interaction of the excitation flux with the current in the armature winding produces the electromagnetic torque. Under linear magnetic conditions the instantaneous electromagnetic torque can be expressed as a vector (cross) product of the excitation flux linkage and armature current space phasors [5],

$$T_e = c\, \vec{\lambda}_f \times \vec{I}_a \tag{2.1}$$

In eqn (2.1) c is a constant and $\times$ denotes the vector product. Since the two space phasors are in space quadrature, eqn (2.1) can be put into the following form,

$$T_e = c\, \lambda_f\, I_a \tag{2.2}$$

If the excitation flux is maintained constant, the electromagnetic torque can be controlled by varying the armature current and a change in the armature current will result in a rapid change in the torque. It is the purpose of vector control of ac motors to have a similar technique of rapid torque control.

2.1.2   *Electromagnetic torque production in ac motors*

In an ac motor it is much more difficult to realize the dc motor torque control principle, because the currents and flux linkages are coupled. In an attempt to decouple the currents and the flux linkages, the research has been done which has led to the development of the so called vector-control schemes, which is to obtain two current components, one of which is a flux-producing current component and the other is a torque-producing current component.

The electromagnetic torque of an ac induction motor [3, 4] can be expressed as

$$T_e = -\frac{3}{2}\vec{\lambda}'_r \times \vec{i}'_r \;;$$

(2.3)

eqn (2.3) is the foundation of rotor field oriented control.

For a machine with p pole pairs eqn (2.3) has to be multiplied by p. It is possible to derive a number of alternative expressions for the torque of an induction machine by aligning the d-axis to stator flux linkage, rotor flux linkage or air gap flux linkage in the synchronous reference frame as shown in Fig. 2.2.
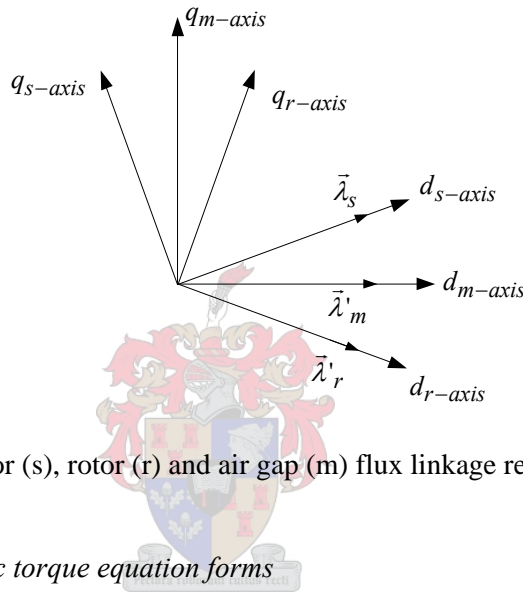
Fig. 2.2. Stator (s), rotor (r) and air gap (m) flux linkage reference frames.

2.1.3   *Electromagnetic torque equation forms*

As mentioned in the previous section, the electromagnetic torque is invariant to the reference frame selected. However from the viewpoint of control theory, how does the selection of the different reference frames affect the torque equation? This section describes the different torque equations by selecting the different reference frames.

• Rotor flux oriented control

If the d-axis of the reference frame is aligned with the rotor flux linkage, this is referred to as rotor flux oriented control. In rotor flux oriented control, $\vec{\lambda}'_{dr} = \vec{\lambda}'_r$, $\vec{\lambda}'_{qr} = 0$ and

$i'_{qr} = -\frac{L_m}{L_r}i_{qs}$ [2, 5, 34].

By using eqn (2.3) the torque equation can be deduced as

$$
\begin{aligned}
T_e &= -\frac{3}{2}\vec{\lambda}'_r \times \vec{i}'_r \\
&= -\frac{3}{2}\vec{\lambda}'_{dr} \times (i'_{dr} + ji'_{qr}) \\
&= -\frac{3}{2}\vec{\lambda}'_{dr} \times (i'_{dr} + j(-\frac{L_m}{L_r}i_{qs})) \\
&= \frac{3}{2}\frac{L_m}{L_r}\lambda'_{dr}\, i_{qs}
\end{aligned}
\qquad (2.4)
$$

The rotor flux oriented control strategy offers high performance as well as independent control of torque and flux. So this control strategy has been widely used in induction motor drives.

- Stator flux oriented control

If the d-axis of the synchronous reference frame is aligned with the stator flux linkage, this is referred to as stator flux oriented control. In stator flux oriented control, $\vec{\lambda}_{ds} = \vec{\lambda}_s$, $\vec{\lambda}_{qs} = 0$ and $i'_{qr} = -\frac{L_s}{L_m}i_{qs}$ [7, 35-36].

By using eqn (2.3) the torque equation can be deduced as

$$
\begin{aligned}
T_e &= -\frac{3}{2}\vec{\lambda}'_r \times \vec{i}'_r \quad = -\frac{3}{2}(L_r\vec{i}'_r + L_m\vec{i}_s) \times \vec{i}'_r \\
&= -\frac{3}{2}L_m\vec{i}_s \times \vec{i}'_r \quad = -\frac{3}{2}\frac{L_m}{L_s}(L_s\vec{i}_s + L_m\vec{i}'_r) \times \vec{i}'_r \\
&= -\frac{3}{2}\frac{L_m}{L_s}\vec{\lambda}_s \times \vec{i}'_r = -\frac{3}{2}\frac{L_m}{L_s}\vec{\lambda}_{ds} \times (i'_{dr} + ji'_{qr}) \\
&= -\frac{3}{2}\frac{L_m}{L_s}\vec{\lambda}_{ds} \times (i'_{dr} + j(-\frac{L_s}{L_m}i_{qs})) \\
&= \frac{3}{2}\lambda_{ds}\, i_{qs}
\end{aligned}
\qquad (2.5)
$$

The advantage of this control strategy is that the stator flux linkage can be obtained accurately.

- Air gap flux oriented control

If the d-axis of the synchronous reference frame is aligned with the air gap flux linkage, this is referred to as air gap flux oriented control. In air gap flux oriented control, $\vec{\lambda}_{dm} = \vec{\lambda}'_m$, $\vec{\lambda}_{qm} = 0$ and $i'_{qr} = -i_{qs}$ [34, 37, 38].

By using eqn (2.3) the torque equation can be deduced as

$$
\begin{aligned}
T_e &= -\frac{3}{2}\vec{\lambda}'_r \times \vec{i}'_r &&= -\frac{3}{2}(L_r\vec{i}'_r + L_m\vec{i}_s) \times \vec{i}'_r \\
&= -\frac{3}{2}L_m\vec{i}_s \times \vec{i}'_r &&= -\frac{3}{2}L_m(\vec{i}'_m - \vec{i}'_r) \times \vec{i}'_r \\
&= -\frac{3}{2}L_m\vec{i}'_m \times \vec{i}'_r &&= -\frac{3}{2}\vec{\lambda}'_m \times \vec{i}'_r \\
&= -\frac{3}{2}\vec{\lambda}'_{dm} \times (i'_{dr} + j(-i_{qs})) \\
&= \frac{3}{2}\lambda'_{dm}\, i_{qs}
\end{aligned}
\tag{2.6}
$$

The advantage of this control strategy is that the air gap flux linkage can be measured directly, and hence a controller based on the air gap flux is suitable for treating the effect of saturation.

2.1.4   Summary

The mechanism of the torque production in electrical motors has been described and various forms of expression for induction motor torque have been presented in this section. It has been shown that with the special reference frame fixed to the rotor flux linkage, stator flux linkage and air gap flux linkage spaces phasors, the expression of the torque is similar to the expression of the torque for the separately excited dc motor. This suggests that torque control of an induction motor can be performed by decoupled control of the flux- and torque-producing components of the stator currents, which is similar to controlling the field and armature current in the separately excited dc motor. The stator currents of an induction motor can be separated into flux- and torque-producing components by utilizing the park transformation described in [7, 36]. Also, research has shown that the implementation of flux oriented control (or vector control) requires information on the modulus and space angle of the rotor flux, stator flux and air gap flux space phasors respectively. However, the mathematical models for these oriented flux calculations are complex due to the non-linear parameters [5, 34, 36].

The rotor flux oriented control is usually employed in induction motor drives due to the fact that the slip and flux linkage relationship is decoupled, and is relatively simple when compared to the stator and airgap flux oriented control strategies. However, the stator and air gap flux oriented systems have the advantage that stator and air gap flux quantities can be measured directly. Especially for air gap flux oriented control as shown in Fig. 2.3, the air gap flux is relative to the saturation level in the motor and, hence, a controller based on the air gap flux oriented strategy is suitable to treat the effect of saturation.
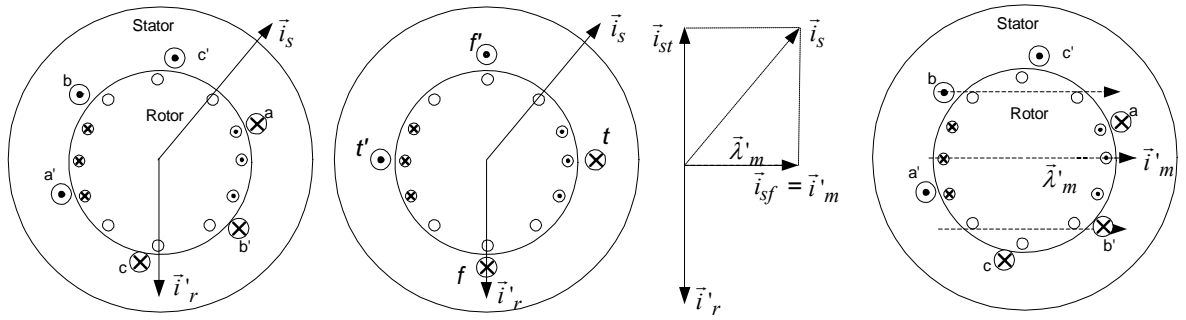
Fig. 2.3. Phasor diagram of the air gap flux oriented control.

Finally, the implementation of the three flux oriented control strategies is complex due to both the control models and the current and voltage transformations.

2.2   Six-Phase Induction machine and control system

When facing the limitation of the power ratings of supplies and semiconductors, the drive system can be performed by using high order phase (HPO) [that is more than three phases] ac motors and respective inverters with proper control systems. This section, therefore, presents a simple analysis of the six-phase induction motor and a field oriented control scheme for this motor.
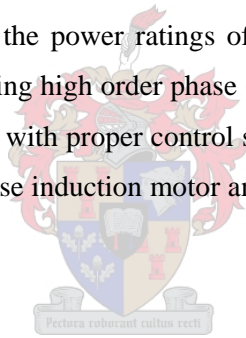
2.2.1   HPO drive system

The need to reach higher power levels with limited power ratings of semiconductor components leads the researchers to investigate HPO machines and their respective drive systems [14-17]. In the HPO drive system the machine output power can then be divided into two or more solid-state inverters that can be kept within the prescribed power limits. An HPO drive system block diagram is shown in Fig. 2.4 [39].

In Fig. 2.4, the *n* sets of three-phase windings are spatially phase shifted by 60°/*n* electrical degrees as shown in Fig. 2.5; each set of the three-phase stator windings is fed by a six-pulse voltage source inverter (VSI). These VSIs may operate according to trigger signals produced by the controller and generate voltages phase shifted by 60º/*n*. The controller can be a digital signal processor (DSP).

Among the different HPO drive systems, one of the most interesting and widely researched in literature is the six-phase drive system with a 6-phase induction motor.
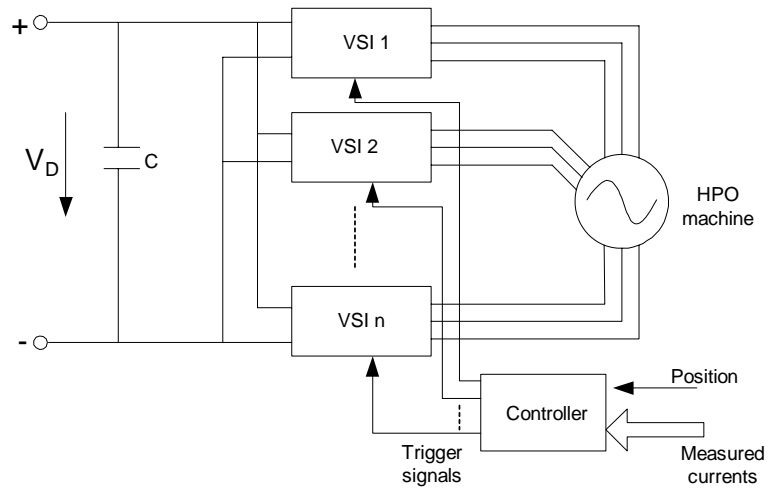
Fig. 2.4. HPO electric machine and drive system.
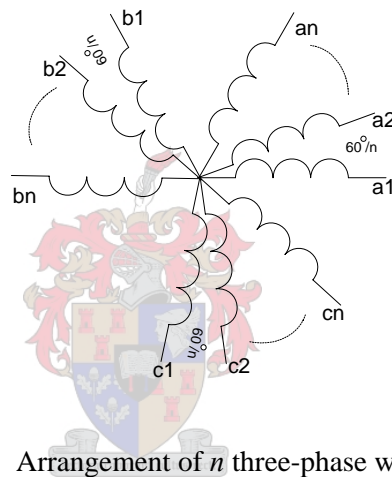
Fig. 2.5. Arrangement of *n* three-phase windings.

2.2.2   *Classification of 6-phase induction motors*

According to the layout of the stator windings the six-phase induction motor can be classified as (i) a split-phase motor as shown in Fig. 2.6(a), which consists of two similar stator windings. A typical split-phase motor is built by splitting the phase belt of a conventional three-phase machine into two parts with a spatial phase separation of 30° electrical. A split-phase induction motor was used in [40] to improve the fault protection in PWM inverter drives; (ii) a dual-stator motor as shown in Fig. 2.6(b), which consists of two independent stator winding groups. A dual-stator motor does not necessarily have similar winding groups. As an example, a different number of poles and different parameters could be used for each winding group. This typical six-phase induction machine can be used in generator systems [23, 41] and in sensorless speed control at low speeds [23]; (iii) a six-phase motor as shown in Fig. 2.6(c), which is a particular case of the split-phase or dual-stator motor. This typical motor consists of two identical stator winding groups, which means that the stator winding

groups have the same number of poles and have identical parameters [27, 28]. In this thesis, the motor investigated belongs to this particular six-phase machine group.

(a) split-phase   (b) dual-stator   (c) six-phase
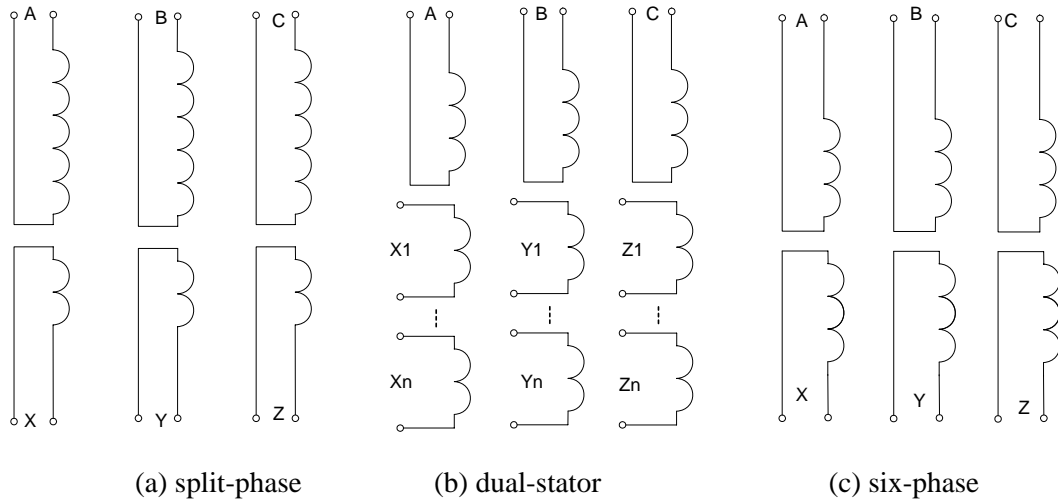
Fig. 2.6. Illustration of six-phase stator windings.

2.2.3   *Six-phase induction machine model*

It is evident that the six-phase induction machine has six phase windings in the stator. But regarding rotor, some arguments exist about how many phases should be used in the analysis and modelling. In the modelling some scholars [27] used six rotor phase windings, while others adopted three rotor phase windings [23, 28, 41]. In this thesis, the author prefers the latter, that is using a three-phase rotor in a six-phase induction machine. Using a three-phase rotor in the modelling gives a clear concept of the per phase equivalent circuit or arbitrary rotating reference frame equivalent circuit. Fig. 2.7 shows the representation of the machine stator windings as well as the set of three rotor phase windings.

To develop the six-phase induction machine model, the following assumptions are made:

- The air gap is uniform and the windings are sinusoidally distributed around the air gap.
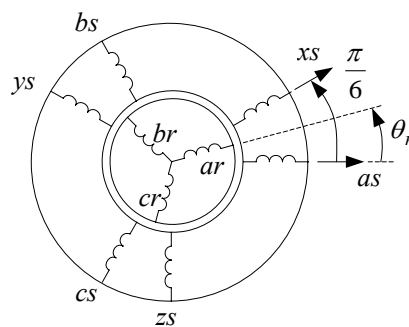
Fig. 2.7. Stator and rotor windings of the six-phase induction machine.

- Magnetic saturation and core losses are neglected.

Therefore, for sinusoidal excitation, the steady state equivalent circuit in the natural reference frame, as shown in Fig. 2.8, is similar to that of a conventional three-phase machine, except for an extra stator circuit. With the above assumptions, the voltage equations [42] in the natural reference frame can be expressed as.

$$[v_s] = [R_s] \cdot [i_s] + p[\lambda_s] \tag{2.7}$$

$$[0] = [R_r] \cdot [i_r'] + p[\lambda_r'], \tag{2.8}$$

where

$$[v_s] = [v_{as} \ v_{bs} \ v_{cs} \ v_{xs} \ v_{ys} \ v_{zs}]^T \tag{2.9}$$

$$[i_s] = [i_{as} \ i_{bs} \ i_{cs} \ i_{xs} \ i_{ys} \ i_{zs}]^T \tag{2.10}$$

$$[i_r'] = [i_{ar}' \ i_{br}' \ i_{cr}']^T \tag{2.11}$$

$$[\lambda_s] = [L_{ss}] \cdot [i_s] + [L_{sr}] \cdot [i_r'] \tag{2.12}$$

$$[\lambda_r'] = [L_{rs}] \cdot [i_s] + [L_{rr}] \cdot [i_r'] \tag{2.13}$$

$[L_{ss}]$ and $[L_{rr}]$ are the matrices of self-inductance of the stator and rotor. These are

$$[L_{ss}] = L_{sl} \begin{bmatrix} 1 & 0 & 0 & 0 & 0 & 0 \\ 0 & 1 & 0 & 0 & 0 & 0 \\ 0 & 0 & 1 & 0 & 0 & 0 \\ 0 & 0 & 0 & 1 & 0 & 0 \\ 0 & 0 & 0 & 0 & 1 & 0 \\ 0 & 0 & 0 & 0 & 0 & 1 \end{bmatrix} + L_{ms} \begin{bmatrix} 1 & -1/2 & -1/2 & \sqrt{3}/2 & -\sqrt{3}/2 & 0 \\ -1/2 & 1 & -1/2 & 0 & \sqrt{3}/2 & -\sqrt{3}/2 \\ -1/2 & -1/2 & 1 & -\sqrt{3}/2 & 0 & \sqrt{3}/2 \\ \sqrt{3}/2 & 0 & -\sqrt{3}/2 & 1 & -1/2 & -1/2 \\ -\sqrt{3}/2 & \sqrt{3}/2 & 0 & -1/2 & 1 & -1/2 \\ 0 & -\sqrt{3}/2 & \sqrt{3}/2 & -1/2 & -1/2 & 1 \end{bmatrix} \tag{2.14}$$

and

$$[L_{rr}] = L_{rl} \begin{bmatrix} 1 & 0 & 0 \\ 0 & 1 & 0 \\ 0 & 0 & 1 \end{bmatrix} + L_{mr} \begin{bmatrix} 1 & -1/2 & -1/2 \\ -1/2 & 1 & -1/2 \\ -1/2 & -1/2 & 1 \end{bmatrix}. \tag{2.15}$$
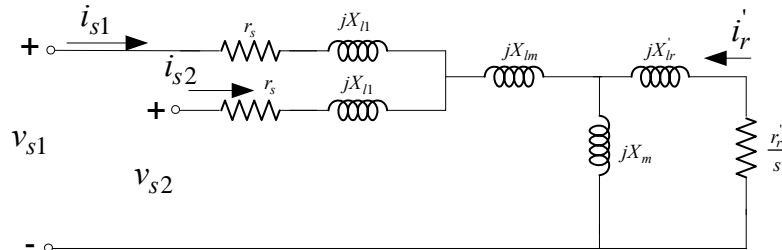
Fig. 2.8. Six-phase induction machine equivalent circuit.

$[L_{rs}] = [L_{sr}]^T = L_m \cdot [\theta_{sr}]$ are the mutual inductances between the stator and rotor, and

$$[\theta]_{sr} = \begin{bmatrix} \cos\theta_1 & \cos\theta_2 & \cos\theta_3 \\ \cos\theta_3 & \cos\theta_1 & \cos\theta_2 \\ \cos\theta_2 & \cos\theta_3 & \cos\theta_1 \\ \cos\theta_4 & \cos\theta_5 & \cos\theta_6 \\ \cos\theta_6 & \cos\theta_4 & \cos\theta_5 \\ \cos\theta_5 & \cos\theta_6 & \cos\theta_4 \end{bmatrix}, \tag{2.16}$$

where

$\theta_1 = \theta_r$, $\theta_2 = \theta_r + 4\pi/6$, $\theta_3 = \theta_r + 8\pi/6$,

$\theta_4 = \theta_r + \pi/6$, $\theta_5 = \theta_r + 9\pi/6$, $\theta_6 = \theta_r + 5\pi/6$.

As for the three-phase ac motor, where the well-known dq0 rotating reference is used in analysis and control, a dq reference frame is also used for the six-phase induction motor. A vector representation of the stator and rotor phase windings for a two-pole, six-phase induction machine is shown in Fig. 2.9 [28]. The six-phase induction machine can be modelled with the following voltage equations in an arbitrary reference frame:

$$v_{qs1} = r_{s1} i_{qs1} + p\lambda_{qs1} + \omega\lambda_{ds1} \tag{2.17}$$

$$v_{ds1} = r_{s1} i_{ds1} + p\lambda_{ds1} - \omega\lambda_{qs1} \tag{2.18}$$

$$v_{qs2} = r_s i_{qs2} + p\lambda_{qs2} + \omega\lambda_{ds2} \tag{2.19}$$

$$v_{ds2} = r_s i_{ds2} + p\lambda_{ds2} - \omega\lambda_{qs2} \tag{2.20}$$

$$v_{qr}' = r_r' i_{qr}' + p\lambda_{qr}' + (\omega - \omega_r)\lambda_{dr}' \tag{2.21}$$

$$v_{dr}' = r_r' i_{dr}' + p\lambda_{dr}' - (\omega - \omega_r)\lambda_{qr}' \tag{2.22}$$
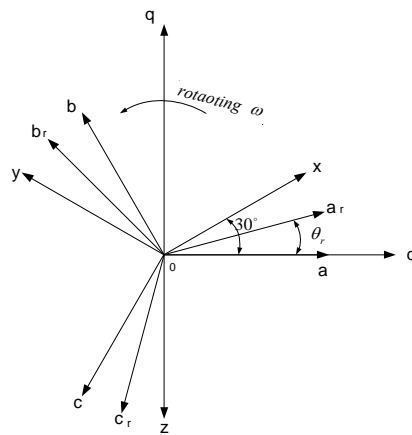
Fig. 2.9. Six-phase induction machine vector plot in the dq rotating frame.

The flux linkage equations are

$$\lambda_{qs1} = L_{ls} i_{qs1} + L_{lm}(i_{qs1} + i_{qs2}) + L_m(i_{qs1} + i_{qs2} + i'_{qr}) \qquad (2.23)$$

$$\lambda_{ds1} = L_{ls} i_{ds1} + L_{lm}(i_{ds1} + i_{ds2}) + L_m(i_{ds1} + i_{ds2} + i'_{dr}) \qquad (2.24)$$

$$\lambda_{qs2} = L_{ls} i_{qs2} + L_{lm}(i_{qs1} + i_{qs2}) + L_m(i_{qs1} + i_{qs2} + i'_{qr}) \qquad (2.25)$$

$$\lambda_{ds2} = L_{ls} i_{ds2} + L_{lm}(i_{ds1} + i_{ds2}) + L_m(i_{ds1} + i_{ds2} + i'_{dr}) \qquad (2.26)$$

$$\lambda'_{qr} = L'_{lr} i'_{qr} + L_m(i_{qs1} + i_{qs2} + i'_{qr}) \qquad (2.27)$$

$$\lambda'_{dr} = L'_{lr} i'_{dr} + L_m(i_{ds1} + i_{ds2} + i'_{dr}) \qquad (2.28)$$

The voltage and flux linkage equations suggest the equivalent circuits of Fig. 2.10. The electromagnetic torque can be expressed in the dq0 reference frame as,

$$T_e = \frac{3}{2}(\frac{P}{2})(\frac{L_m}{L'_r})[\lambda'_{dr}(i_{qs1} + i_{qs2}) - \lambda'_{qr}(i_{ds1} + i_{ds2})] \qquad (2.29)$$
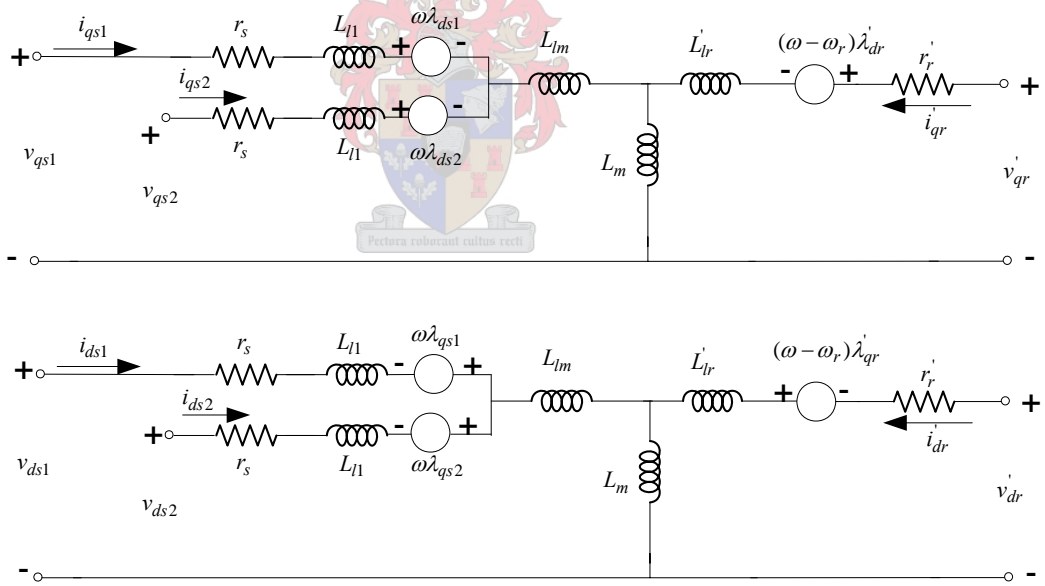
Fig. 2.10. Arbitrary reference frame equivalent circuits for six-phase induction motor.

2.2.4   *Six-phase induction machine control*

As discussed in the previous section, the rotor flux oriented control (RFOC) is usually employed in three-phase induction motors due to the fact that the slip and flux linkage relationship is decoupled, and is relatively simple as compared to the stator and airgap flux

oriented control strategies. The RFOC strategy is also extended to the six-phase drive system [22 – 26]. With the rotor flux oriented control in the synchronously rotating reference frame the important equations [27 – 28] for the six-phase machine control are

$$i'_{qr} = -(\frac{L_m}{L_r})(i_{qs1} + i_{qs2})$$
(2.30)

$$i'_{dr} = \frac{\lambda_r - L_m(i_{ds1} + i_{ds2})}{L_r}$$
(2.31)

$$\lambda_r = \frac{L_m}{(1 + T_r p)}(i_{ds1} + i_{ds2})$$
(2.32)

$$\omega_{sl} = (\frac{L_m}{T_r})(\frac{i_{qs1} + i_{qs2}}{\lambda_r})$$
(2.33)

$$\theta = \int (\omega_r + \omega_{sl})dt$$
(2.34)

$$T_e = \frac{3}{2}(\frac{P}{2})(\frac{L_m}{L'_r})[\lambda_r(i_{qs1} + i_{qs2})]$$
(2.35)

where $T_r = \frac{L'_r}{r'_r}$ is the rotor time constant.

Eqn (2.35) resembles the torque equation of a separately excited dc machine.

The block diagram of a six-phase induction machine controller with RFOC is shown in Fig. 2.11. The input signals to the RFOC controller are the speed and flux reference signals. The error signals, which are from the comparison of the input and feedback signals, are processed by proportional integral (PI) controllers. The outputs of the two PI controllers are the torque and flux stator current commands, i^*_{qs} and i^*_{ds}, respectively. The command currents are further processed through two independent pairs of PI controllers. This is followed by a coordinate transformation to convert the variables from the synchronous rotating frame to the stationary frame, i.e. to obtain two sets of voltage vectors ($v^*_{s\alpha_1}$, $v^*_{s\beta_1}$ and $v^*_{s\alpha_2}$, $v^*_{s\beta_2}$) in the stationary frame. These voltage vectors are used to generate two sets of three-phase reference voltage vectors (v^*_a, v^*_b, v^*_c) and (v^*_x, v^*_y, v^*_z) phase shifted by 30° electrical. The inverter switch trigger signals are produced by a pulse width modulation (PWM) generator [7], which utilizes the principle of three-phase voltage vectors compared to triangular carrier signals.

The two sets of three-phase measured currents are transformed to direct- and quadrature-current vectors in the synchronous rotating reference frame, which are used as feedback signals to estimate the rotor flux vector.
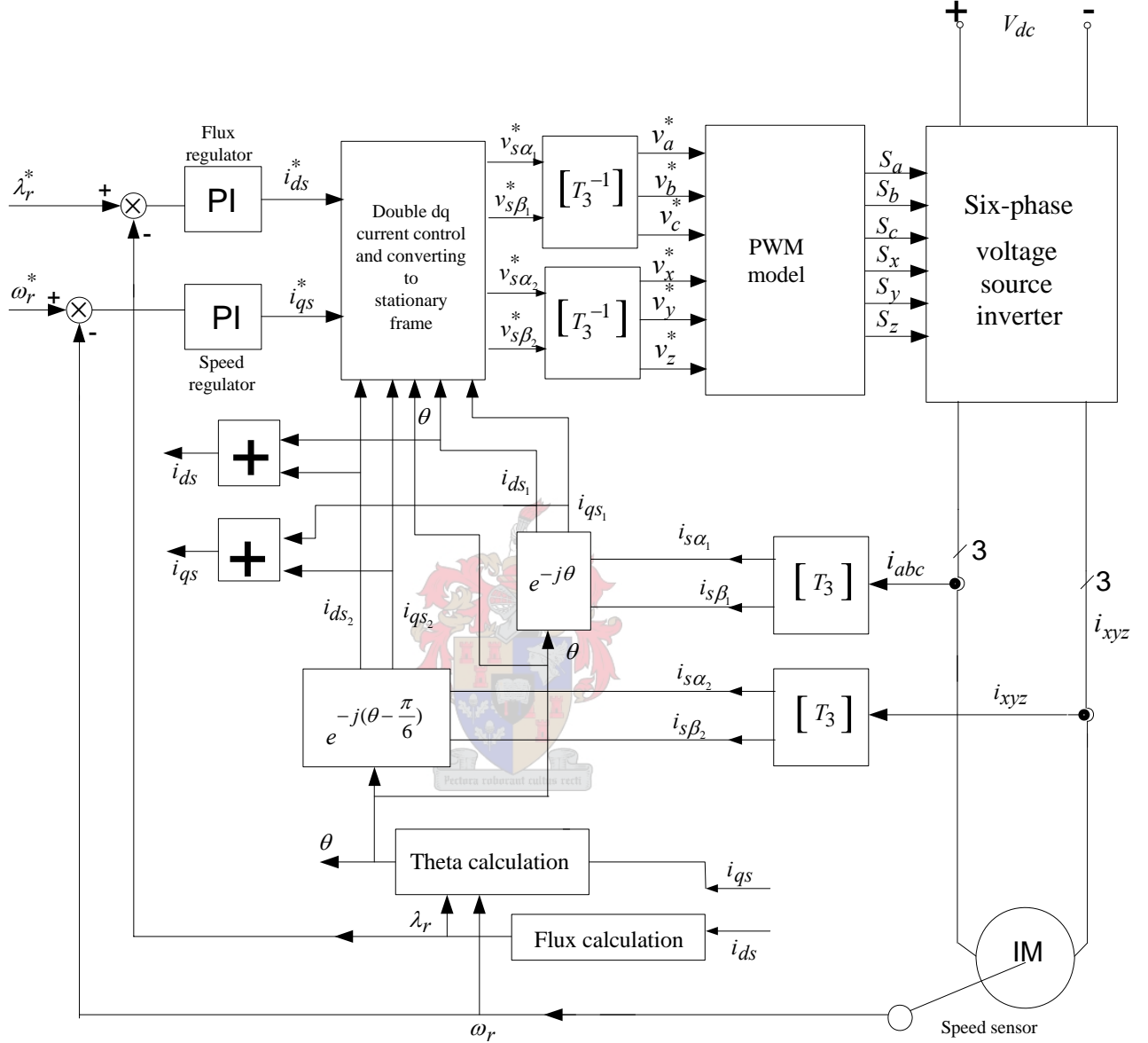
Fig. 2.11. Block diagram of six-induction machine control with RFOC.

The block diagram of the double-pair PI controllers and the reference frame transformation is shown in Fig. 2.12. Furthermore, the matrixes T_3 and T_3^{-1} in Fig. 2.11 are given by

$$T_3 = \frac{2}{3}\begin{bmatrix} 1 & -1/2 & -1/2 \\ 0 & \sqrt{3}/2 & -\sqrt{3}/2 \end{bmatrix} \quad ; \quad T_3^{-1} = \frac{3}{2}\begin{bmatrix} 1 & 0 \\ -1/2 & \sqrt{3}/2 \\ -\sqrt{13}/2 & -1/2 \end{bmatrix}.$$
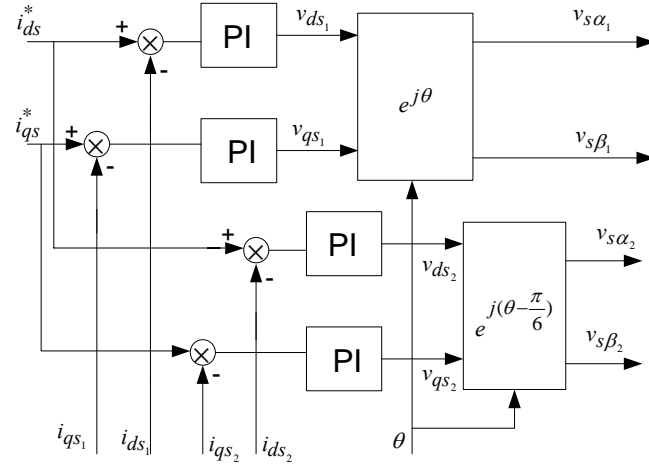
Fig. 2.12. Block diagram of PI controllers and reference frame transformation.

The transformation matrixes in Figs. 2.11 and 2.12 from stationary to rotating reference frame are given by

$$e^{-j\theta} = \begin{bmatrix} \cos\theta & \sin\theta \\ -\sin\theta & \cos\theta \end{bmatrix}; \qquad e^{-j(\theta-\frac{\pi}{6})} = \begin{bmatrix} \cos(\theta-\frac{\pi}{6}) & \sin(\theta-\frac{\pi}{6}) \\ -\sin(\theta-\frac{\pi}{6}) & \cos(\theta-\frac{\pi}{6}) \end{bmatrix}.$$

The inverse transformation is given by

$$e^{j\theta} = \begin{bmatrix} \cos\theta & -\sin\theta \\ \sin\theta & \cos\theta \end{bmatrix}; \qquad e^{j(\theta-\frac{\pi}{6})} = \begin{bmatrix} \cos(\theta-\frac{\pi}{6}) & -\sin(\theta-\frac{\pi}{6}) \\ \sin(\theta-\frac{\pi}{6}) & \cos(\theta-\frac{\pi}{6}) \end{bmatrix}.$$

2.3   **Conclusions**

In this chapter the mechanism of the torque production in electrical motors is described. Furthermore, various forms of expressions for the torque of the induction motor are presented. The six-phase induction machine model and its control system are also described. The important conclusions drawn from this chapter are the following:

- Induction motor control can be modelled in such a way as to emulate brush dc motor control, allowing for separate control of the field and torque current components by selecting a flux oriented control scheme.

- Among the three flux oriented control strategies, only the rotor flux oriented control is decoupled and relatively simple to implement. This is the reason that the rotor flux oriented control is widely used in three-phase or six-phase induction motor control.

- Air gap flux oriented control has the advantage that the air gap flux can be measured directly and that the air gap flux is relative to the saturation level in the motor. If the issues of complicated control and the coupling of the slip and flux can be solved, the air gap flux oriented control is a good control strategy. This will be elaborated further in the next chapter.

- It is shown that the rotor flux oriented control can be extended to the six-phase induction motor control. However, the extra transformations show that the control system is more complicated than with a three-phase induction motor.

- As discussed, the flux-oriented control causes the performance of the induction machine to resemble that of a dc motor. However, this requires a higher level of control complexity, especially in the case of a six-phase induction motor. In Chapter 3 a novel current control strategy used to solve this complex control problem will be discussed.
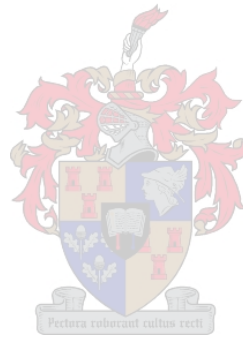
3 NOVEL CURRENT CONTROL AND ANALYSIS OF SIX-PHASE INDUCTION MOTOR

In this chapter special phase current waveforms are proposed in order to realize the direct control of the field and torque currents of the six-phase induction dc motor (IDCM). With these special phase current waveforms the distribution of the field in the air gap of the motor is analysed. The torque equation is derived by the use of the IDCM model and the static torque is calculated under balanced MMF condition. Lastly the air gap MMF harmonics of the IDCM are analysed and the per phase self- and mutual inductances are described. This chapter presents for the first time the operational principle of the IDCM.

3.1   Background knowledge

A dc machine consists of a stationary field structure utilizing a stationary dc excited winding or permanent magnets, and a rotating armature winding supplied through a commutator and brushes. This basic structure is schematically illustrated in Fig. 3.1 [7]. The construction of a dc machine guarantees that the field flux φ_f produced by the field current I_f is perpendicular to the armature flux φ_a produced by the armature current I_a. These can be represented by space vectors as shown in Fig. 3.1; note that the space vectors are stationary and orthogonal. Neglecting the armature reaction and field saturation, the developed torque is given by

$$T_e = K_t' I_a I_f. \tag{3.1}$$

Obviously, the electromagnetic torque is proportional to the product of armature current and the field current as shown in eqn (3.1). The armature and field circuits are decoupled, which means that field current and armature current can be adjusted independently without interference. In a typical application, adjustable speed operation is obtained by fixed field current and adjustable armature current to control the electromagnetic torque.
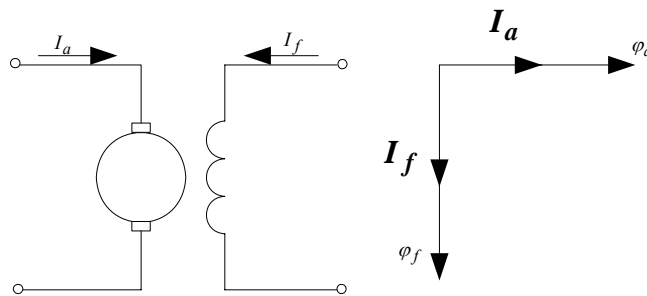
Fig. 3.1. Separately excited dc machine and space vector representation.

The thought of emulating dc machine control has been extended to the three-phase induction machine. The induction machine control is considered in the synchronously rotating reference frame (dq), where the sinusoidal variables appear as dc quantities in the steady state. This means that the three-phase induction machine can be controlled like the separately excited dc machine. This kind of induction machine control strategy, namely vector control, has been successfully applied in industry as discussed in Chapter 2.

Because of the demand for high reliability and high torque performance, scholars have extensively studied HPO induction machines. HPO induction machines have specifically been used in propulsion systems, e.g. ship propulsion [43] and electric vehicles (EVs) [44 – 46].

As described in the previous chapter, the control of the six-phase induction machine is very complex. This is one of the main reasons for the limited usage of HPO induction machines. Another distinguished achievement in HPO machine control is that of a five- or six-phase induction machine with combined fundamental and third harmonic currents to improve the electromagnetic torque density of the machine, as was proposed in [31, 32]. For the conventional induction machine only the sinusoidal flux distribution exists in the airgap [47 – 48], in other words the flux density is maximum only in a small area. As a result of the unsaturated state of the most part of the core, the power density and torque density are comparatively lower. By the injection of a third harmonic current with proper amplitude in the phase current, a rectangular distributed flux is produced, as shown in Fig. 3.2. This will bring about improved iron utilization, higher power density and increased output torque. However, the control strategy will also be complex.
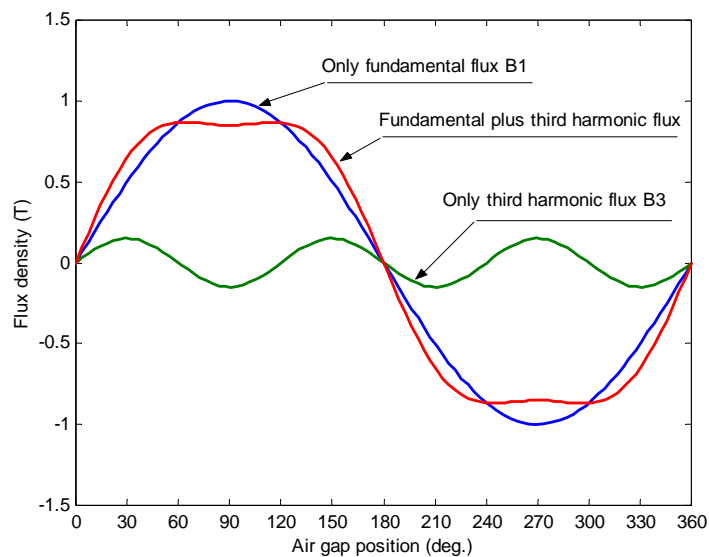
Fig. 3.2. Comparison of two different flux density distribution waveforms.

3.2   Six-phase current waveform configuration

Based on the previous section, the author proposes a six-phase current configuration as shown in Fig. 3.3 [49, 50]. The current waveforms produce a rectangular flux density in the air gap. The field and torque current components, I_F and I_T, can be controlled separately like in a dc machine. The control system is simple to implement, because unlike in vector control, there are not any transformations.

The phase current waveforms are assumed to be supplied by six full-bridge converters, one converter per phase. With these current waveforms two separate rotating stator MMFs are generated, namely a *field* rotating MMF and a *torque* rotating MMF.

Consider phase *a* as an example. Fig. 3.4 shows the composition of the waveform, whereby time *0 - t₃* and time *t₃ - t₆* show field and torque components respectively. The other phase current waveforms follow the same pattern of phase *a*, but with a certain phase displacement. The function of the field current component is to produce a magnetic field inside the motor. Normally, the average amplitude of the flux density distribution in the air gap is fixed, so that the amplitude of the field current component is fixed. At rated field current this will ensure that the average flux density in the iron is at the knee of the *BH* magnetization curve.
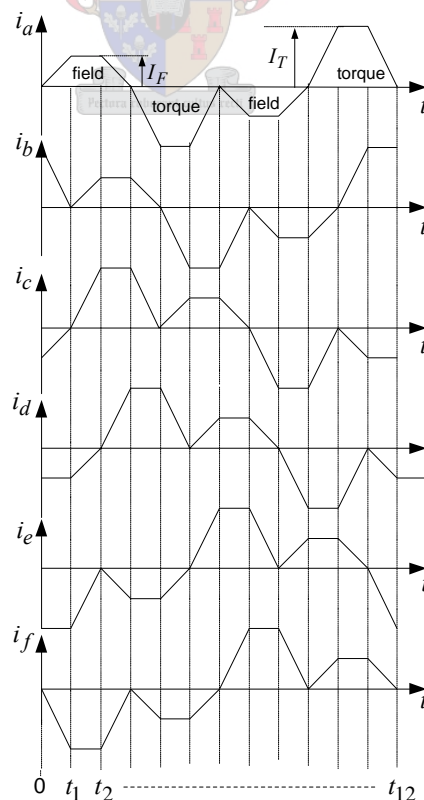
Fig. 3.3. Six-phase current waveform configuration.
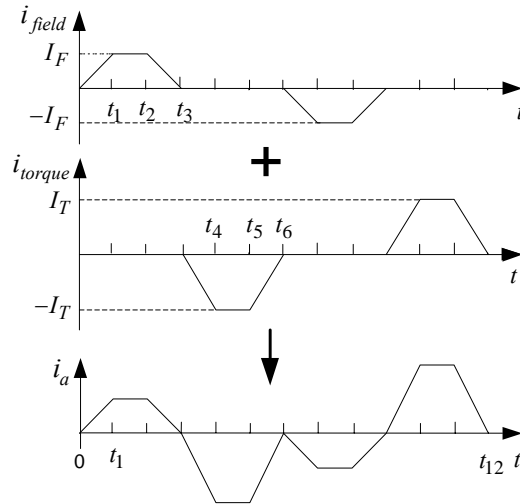
Fig. 3.4. Composition of phase *a* current.

When the six-phase induction machine is supplied with the phase current waveforms of Fig. 3.3, a rotating magnetic field is produced in the air gap. This rotating magnetic field induces an electromotive force (EMF) in the rotor conductors that cut the magnetic field. The induced EMF results in rotor conductor current because of the closed rotor circuit. The electromagnetic torque is produced by the interaction of the induced current and the rotating field. The induced rotor current, however, also generates a magnetic field in the air gap and distorts the main stator magnetic field. This causes the electromagnetic torque to become smaller. The role of the stator torque current component is to cancel the induced rotor magnetic field to restore the main stator field. The amplitude of the torque current component, therefore, should vary with the amplitude of the rotor induced current. At any instant, three neighboring phases form a field winding that produces a resultant field MMF, while the other three neighboring phases form a torque winding that produces a resultant torque MMF. Hence, it is clear that the resultant field MMF and the resultant torque MMF are always electrically perpendicular to each other. For the viewpoint of control, the configuration of the current waveforms makes the six-phase motor operate like a dc motor allowing the field and torque currents to be controlled separately.

3.3   Field intensity analysis

A six-phase induction machine has been built based on a commercial 2.2 kW three-phase, 4-pole induction machine with 36 slots and 28 slots in the stator and rotor, respectively. Now the six-phase induction machine possesses two poles with three slots per pole per phase in the stator and 14 phases on the rotor. The detailed design specifications of the six-phase machine are given in the Appendix A.

Fig. 3.5 shows the direction of current in the respective phases of the six-phase induction machine as well as the direction of the MMFs inside the machine at the time of $t = t_1/2$, as explained in Fig. 3.3. The direction of the current is given by the conventional method of dots and crosses. It is clear that there are three MMFs that exist inside the six-phase machine. The MMF amplitudes across two air gaps with the assumption of concentrated windings are defined as follows:

F_f is the field MMF due to the three-phase field currents, i_a, i_c and i_d. F_t is the torque MMF due to the three-phase torque currents, i_b, i_e and i_f. F_r is the rotor MMF due to the rotor phase induced currents $i_{r7}, i_{r8} \cdots, i_{r13}$.

As previously explained, at any instant three neighboring stator phases are used as field windings to produce the resultant field MMF, F_f. In Fig. 3.6 the waveforms of the three phase currents used to generate the field MMF are redrawn for time $t = 0 - t_1$. The instantaneous values of the three phase currents can be expressed as,
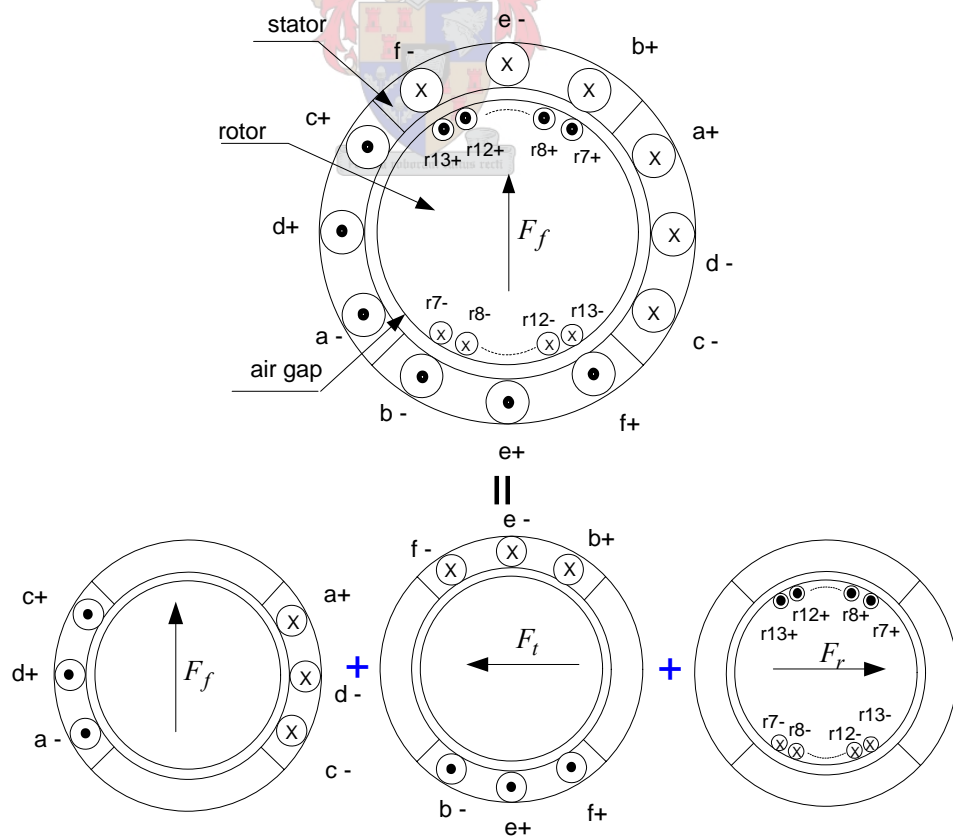
Fig. 3.5. MMF configuration inside the machine at $t = t_1/2$.

25

$$i_a = \frac{I_F}{t_1} t,$$ (3.2)

$$i_c = \frac{I_F}{t_1} t - I_F,$$ (3.3)

$$i_d = -I_F.$$ (3.4)

From this the resultant *amplitude* of the field MMF, F_f, for time interval $0 - t_1$ can be calculated as,

$$\begin{aligned}
F_f &= N_a i_a - N_c i_c - N_d i_d \\
&= N_s i_a - N_s i_c - N_s i_d \\
&= N_s (i_a - i_c) - N_s(-I_F) \\
&= 2 N_s I_F
\end{aligned}$$ (3.5)

From the above field analysis, the air gap field intensity [51] can be obtained as shown in Fig. 3.7 corresponding to the three field phase currents respectively. For simplification, the permeability of iron is assumed to be infinite, hence, the field intensities in the stator iron and rotor iron are zero. Applying Ampere's law, the amplitude of the air gap field intensity can be calculated as

$$H_i = \frac{N_i \, i_i}{2 \, l_g},$$ (3.6)

where $i = a, c, d$. For illustration, Fig. 3.8 shows the field intensity waveforms versus circumference position, θ, when $t = 0$, $t_1/2$ and t_1, where the reference position is selected in Fig. 3.7. The resultant field intensity, $H_{tf}(\theta)$ (the subscript "*tf*" means total field intensity), is the sum of $H_a(\theta)$, $H_c(\theta)$ and $H_d(\theta)$, and is shown in Fig. 3.8.
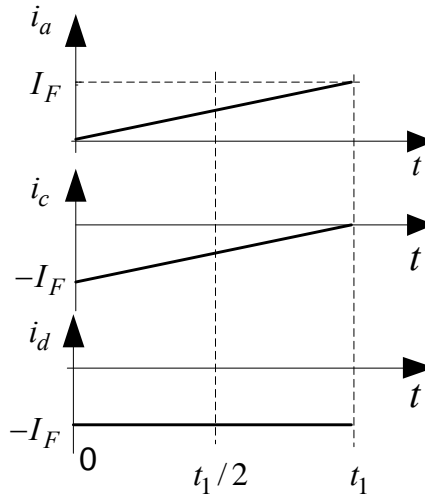
Fig. 3.6. Stator field current waveforms.
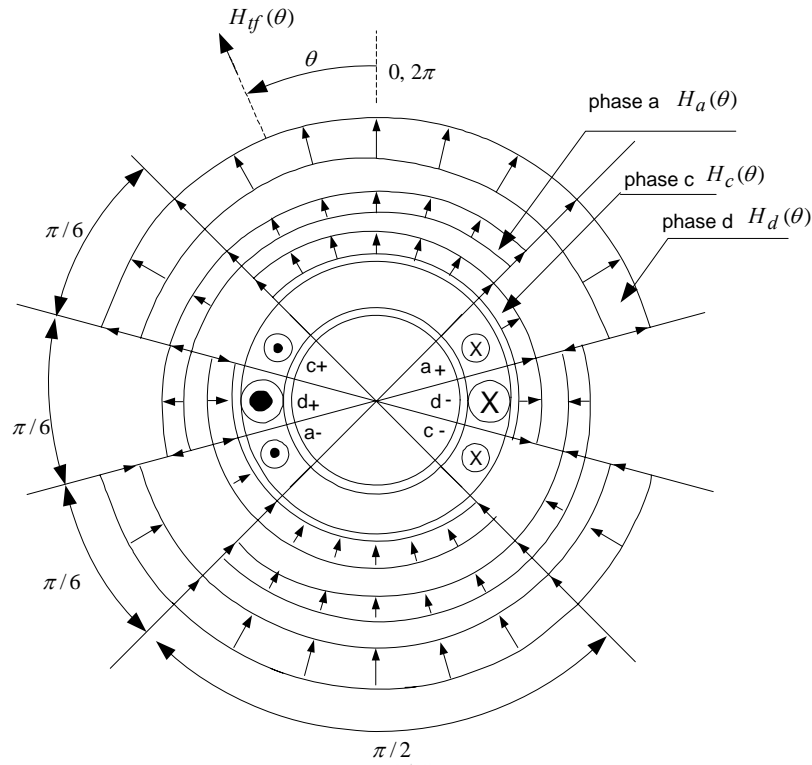
Fig. 3.7. Illustration of field intensity distribution in the air gap at $t = t_1/2$.

From Fig. 3.8 it is found that:

(i)   The resultant field intensity due to the field MMF in the air gap is approximately trapezoidal, similar to the air gap field intensity in a dc machine.

(ii)   The amplitude of the resultant field intensity is constant due to the constant amplitude of the resultant MMF as given by eqn (3.5).

(iii)   The plateau angle of the resultant field intensity waveform is always $\pi/2$ minimum. This field intensity waveform will result in induced voltage and current waveforms in the rotor phases that are identical but out of phase; this is shown in Fig. 3.9. Note that the rotor phase current waveform is assumed in the analysis as quasi-square (to simplify the analysis), but this has to be investigated in further studies (practical measurement of the actual current waveform is shown in Chapter 6).

Based on the above field intensity analysis and the rotor current waveforms, the six-phase induction machine, due to the special stator phase current waveforms, is referred to as an induction dc machine (IDCM).

27
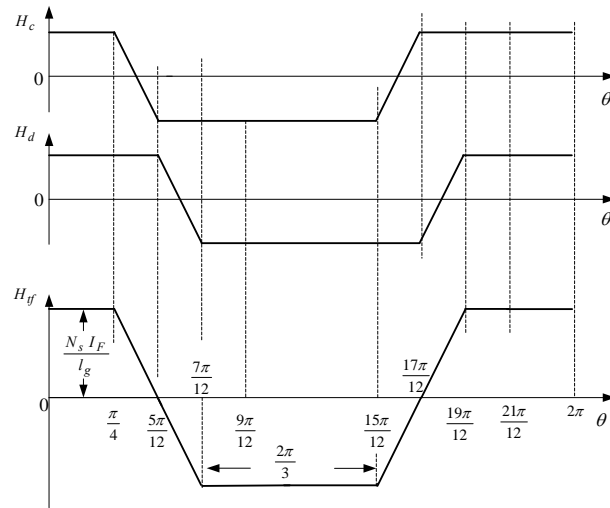
(a) $t = 0$
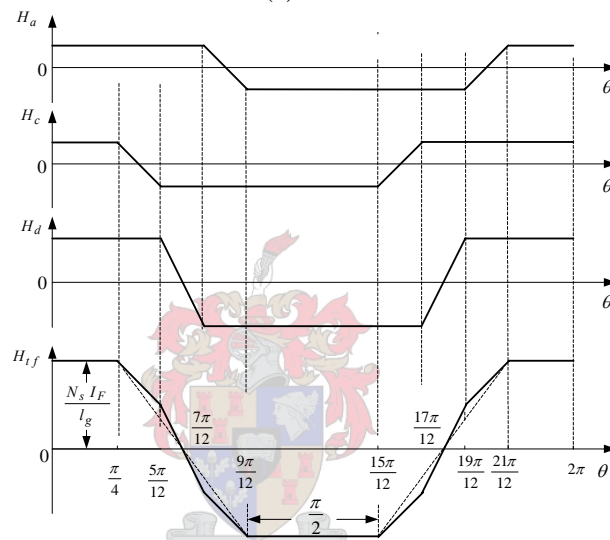
(b) $t = t_1/2$
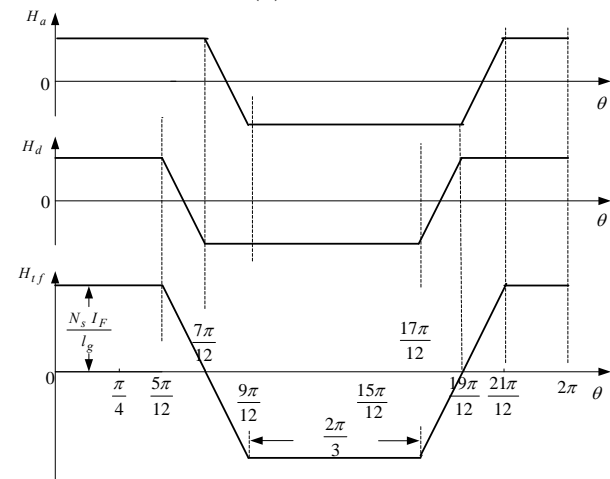
(c) $t = t_1$

Fig. 3.8. Field intensity distributions in the air gap at different times.
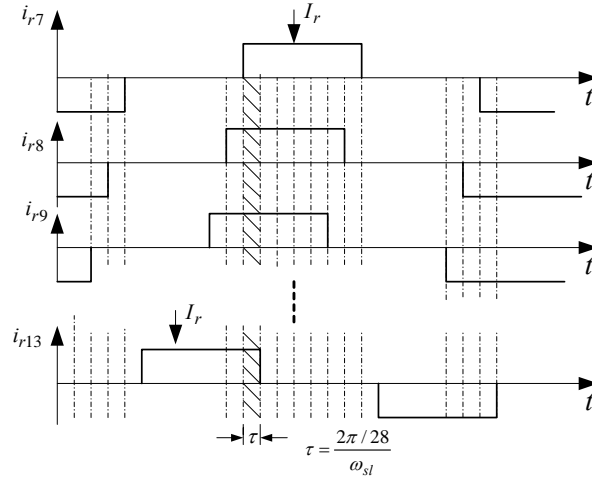
Fig. 3.9. Rotor phase current waveforms (seven rotor phases always active).

With seven (of the fourteen) rotor phases active for this machine, the amplitude of the rotor MMF, F_r, can be expressed as,

$$F_r = \sum_{i=7}^{13} N_{ri}\, i_{ri} = 7\, N_r\, I_r\, .$$ (3.7)

For the stator torque currents during time $t = 0 - t_1$, as shown in Fig. 3.3, the amplitude of the torque MMF, F_t, can be expressed as,

$$F_t = N_b\, i_b - N_e\, i_e - N_f\, i_f = 2\, N_s\, I_T\, .$$ (3.8)

For comparison, Fig. 3.10 shows the field intensity distributions in the air gap with field current, torque current and rotor current flowing at $t = t_1 / 2$.

From this it can be concluded that:

(i)   The phase displacement between H_{tf} and H_{tt} is $\pi / 2$. This verifies that the special current waveform configuration produces perpendicular field and torque magnetic fields.

(ii)   The rotor current field intensity, H_{tr}, is opposite to the torque current field intensity, H_{tt}, which means that it is possible that these field intensities in the air gap can cancel each other.

29
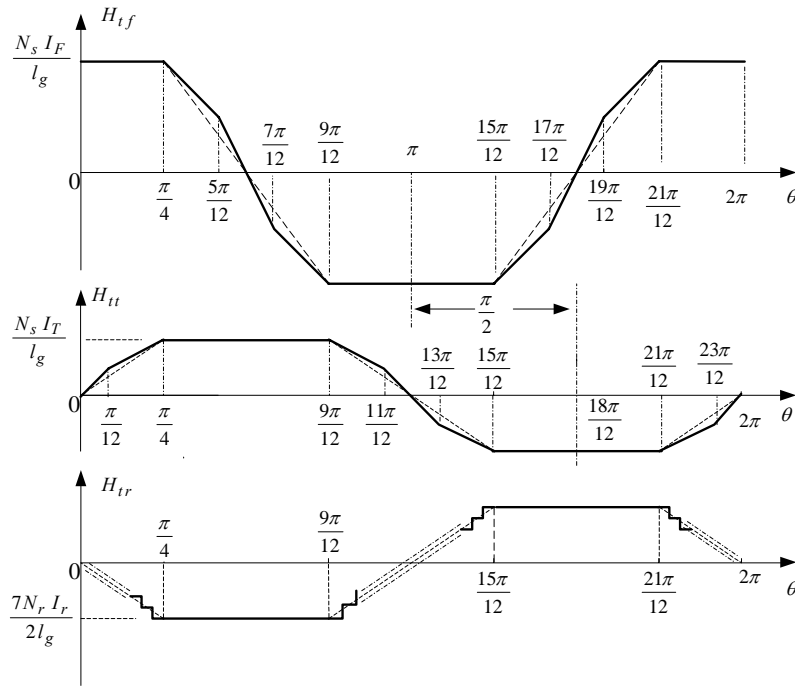
Fig. 3.10. Three field intensity distributions in the air gap at time $t = t_1/2$.

3.4   Torque formula derivation

In the steady state, the MMF distribution inside the motor is assumed to be as shown in Fig. 3.11. Fig. 3.12 shows the phasor composition diagram of Fig. 3.11.
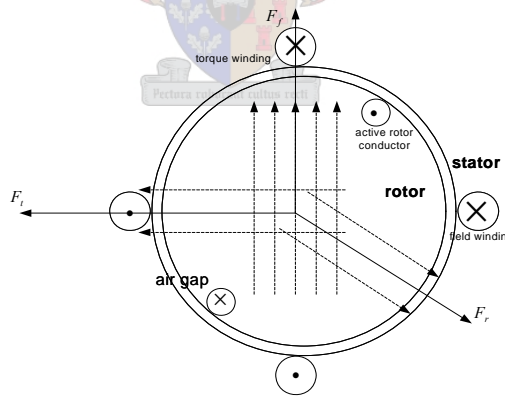
Fig. 3.11. MMF distribution diagram.
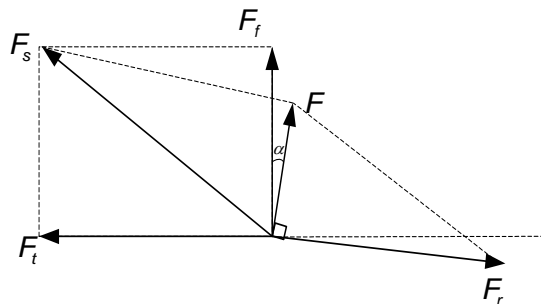
Fig. 3.12. MMF phasor composition diagram.

From Fig. 3.12 it follows that:

$$F^2 = F_s^2 - F_r^2$$
$$= F_f^2 + F_t^2 - F_r^2$$

(3.9)

By ignoring the stator and rotor core reluctances, the air flux density can be expressed as,

$$B = \mu_0 \frac{F}{2l_g}$$
$$= \mu_0 \frac{\sqrt{(2N_s I_F)^2 + (2N_s I_T)^2 - (7N_r I_r)^2}}{2\,l_g} .$$

(3.10)

With a constant flux density, B, the EMF voltage is induced in the rotor phase windings. The amplitude of this induced voltage can be calculated, as for brush dc motors, as

$$E = 2\,N_r\,B\,l\;\omega_{sl}\;r\,.$$

(3.11)

The induced rotor phase current is given by

$$I_r = \frac{E}{r_{eq}} = 2\,N_r \frac{B\,l\;\omega_{sl}\;r}{r_{eq}} ,$$

(3.12)

where

$$r_{eq} = \rho \frac{l'}{S} N_r ,$$

(3.13)

where N_r is the number of turns in series per phase of the rotor and for a cage rotor $N_r = 1$. Therefore, eqns (3.11) – (3.13) are valid for both wound and cage rotors. Note that in the analysis the effect of the rotor inductance is ignored. Substituting eqns (3.10) and (3.13) into eqn (3.12), it follows that

$$I_r = 2\,\mu_0 \frac{l}{l'} \frac{S}{\rho} \frac{r}{2l_g} \omega_{sl} \sqrt{(2N_s I_F)^2 + (2N_s I_T)^2 - (7N_r I_r)^2}$$
$$= k'_c\,\omega_{sl} \sqrt{(2N_s I_F)^2 + (2N_s I_T)^2 - (7N_r I_r)^2}$$

(3.14)

where, $k'_c = \mu_0 \dfrac{l}{l'} \dfrac{S}{\rho} \dfrac{r}{l_g} .$

From eqn (3.14) it follows that:

$$I_r = \sqrt{\frac{(2N_s I_F)^2 + (2N_s I_T)^2}{(\dfrac{1}{k'_c\,\omega_{sl}})^2 + (7N_r)^2}} .$$

(3.15)

Therefore, the amplitude of the rotor MMF is

$$F_r = 7N_r \sqrt{\frac{(2N_s I_F)^2 + (2N_s I_T)^2}{(\dfrac{1}{k'_c\,\omega_{sl}})^2 + (7N_r)^2}} .$$

(3.16)

Also, the flux density equation can be obtained as

$$B = \mu_0 \frac{\sqrt{(2N_s\,I_F)^2 + (2N_s\,I_T)^2 - (7N_r\sqrt{\dfrac{(2N_s\,I_F)^2 + (2N_s\,I_T)^2}{(\dfrac{1}{k'_c\,\omega_{sl}})^2 + (7N_r)^2}})^2}}{2\,l_g} \tag{3.17}$$

For the specific motor with seven rotor phases active and using the Lorentz force, the electromagnetic torque law is given by

$$T_e = 7(2\cdot N_r)\cdot(B\cdot I_r\cdot l)\cdot r$$

$$= 7(2N_r)\mu_0 \frac{\sqrt{(2N_s\,I_F)^2 + (2N_s\,I_T)^2 - (7N_r\sqrt{\dfrac{(2N_s\,I_F)^2 + (2N_s\,I_T)^2}{(\dfrac{1}{k'_c\,\omega_{sl}})^2 + (7N_r)^2}})^2}}{2\,l_g} I_r\,l\,\,r$$

$$= 7(N_r\,\mu_0\,l\,r)\frac{\sqrt{(2N_s\,I_F)^2 + (2N_s\,I_T)^2 - (7N_r\sqrt{\dfrac{(2N_s\,I_F)^2 + (2N_s\,I_T)^2}{(\dfrac{1}{k'_c\,\omega_{sl}})^2 + (7N_r)^2}})^2}}{l_g}\sqrt{\dfrac{(2N_s\,I_F)^2 + (2N_s\,I_T)^2}{(\dfrac{1}{k'_c\,\omega_{sl}})^2 + (7N_r)^2}}$$

$$\tag{3.18}$$

Equation (3.18) is the general equation for the electromagnetic torque of the six-phase IDCM. It has been derived by the use of the motor's parameters and angular slip frequency. In the next section attention is given to the static torque calculation under the balanced MMF condition.
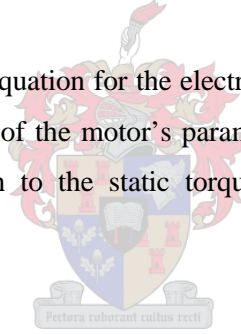
3.5   Static torque calculation

For correct operation F_t must be controlled in such a way that it is equal in amplitude but opposite in direction to F_r [referring to eqns (3.7) and (3.8) and Figs. 3.11 and 3.12], which means that

$$2N_s\,I_T = 7N_r\,I_r\,. \tag{3.19}$$

From eqn (3.19) thus

$$I_T = \frac{7\,N_r\,I_r}{2\,N_s}\quad. \tag{3.20}$$

From eqn (3.12) and (3.20), the important relationship between I_T and ω_{sl} is obtained namely,

$$k = \frac{\omega_{sl}}{I_T} = \frac{N_s\,r_{eq}}{7\,(N_r)^2\,B\,l\,r}\,. \tag{3.21}$$

Form eqn (3.21) it is clear that the control gain k is dependent on two variables namely r_{eq}, which is temperature sensitive, and B, which is dependent on the field current I_F. The field current can be controlled to keep B at the desired value, but r_{eq} can easily vary by 40% due to temperature changes. This will cause that a wrong k-value is used in the control system, which will disturb the MMF balance and torque output of the motor. The effect of the variation of k on the torque output is further investigated in Chapter 6. Using the design data of the six-phase induction machine and with $B = 0.47$ T, k of eqn (3.21) is calculated as $k = 7.08$ (rad/s)/A.

The principle of the operation of the IDCM is that F_f generates a nearly square flux density in the air gap; at a certain slip speed, the rotor F_t is cancelled by F_r so that the field flux F_f is not distorted; torque is generated by Lorentz forces on the rotor conductors. The stator flux field occupies half of the air gap periphery, which means that 7 phases among the rotor cut the field lines and are thus active as shown Fig. 3.5. A simplified rotor equivalent circuit is shown in Fig. 3.13. To investigate the air gap flux density with the supply of the special stator phase current waveforms a wound rotor with connectors, as shown in Fig. 3.13, was designed and built. The role of the connectors for every rotor phase is to close or open the rotor phase windings. Therefore, the induced rotor voltage used to evaluate the air gap flux density can be measured by opening these connectors. The electromagnetic torque can be evaluated by closing these connectors. Further experimental investigation will be described in Chapter 6.

By using eqn (3.19) for the balanced MMF condition, eqn (3.18) of the electromagnetic torque becomes

$$
\begin{aligned}
T_e &= 7(2N_r)(BI_r l)\, r \\
&= 2\,(7N_r\,I_r)\,Bl\,r \\
&= (4N_s\,l\,r)\,B\,I_T
\end{aligned}
\qquad (3.22)
$$

Using the six-phase IDCM parameters as given in Appendix A, the calculation of torque versus torque current [eqn (3.22)] and the induced rotor phase voltage versus slip speed [eqn (3.11)] is done as shown in Fig. 3.14. Note that in the calculation, $B = 0.47$ T is used and the slip speed is

$$
\omega_{sl} = \omega_e - \omega_r \,,
\qquad (3.23)
$$

where ω_e is the synchronous speed, which is 3000 rpm at 50 Hz for a 2-pole induction machine and ω_r is the rotor speed.
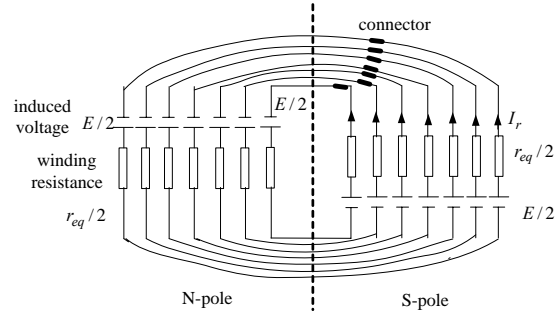
Fig. 3.13. Rotor equivalent circuit of 2-pole motor with seven rotor phases active.
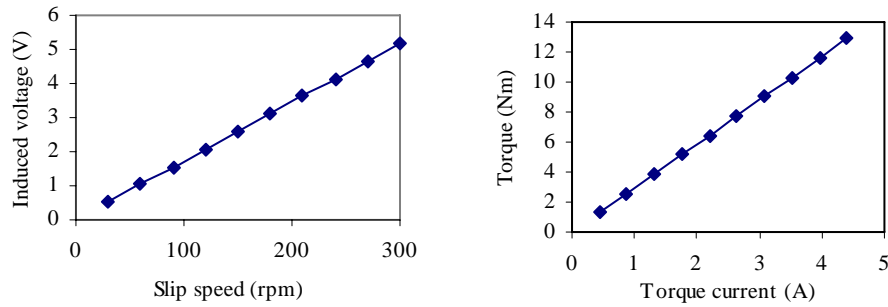
Fig. 3.14. Calculation of induced rotor voltage and torque.

3.6   Theoretical field current calculation

In section 3.4 the reluctances of the stator and rotor cores are ignored in the analysis of the air gap flux density. However, when calculating air gap flux density versus field current, the stator and rotor core reluctances need to be taken into account due to the effect of saturation. In other words, it is important to know the air gap flux density versus field current by considering the stator and rotor core's reluctance MMF drops. Due to symmetry only half of the magnetic circuit of the machine needs to be analyzed. For the specific machine with the stator and rotor core dimensions as given in Appendix A, the approximate magnetic circuit (AMC) [50, 52 - 53] is selected and divided into nine regions as shown in Fig. 3.15. In the analysis three phases are active with the currents as shown in Fig. 3.6 at time $t = t_1/2$.

The effect of cross magnetisation is ignored in this calculation method. The calculated MMF drop in every region and the field currents corresponding to the flux density are given in Table 3.1. For a detail explanation of the calculation procedure refer to Appendix C. From Table 3.1 it can be seen that for a field current amplitude of 4.14 A the air gap flux density equals 0.5 T. At this field current the MMF drops in regions 1, 6 and 9 are much larger than in the other regions. To avoid heavy saturation in the stator and rotor cores a rated field current of 3.5 A is chosen for the machine as shown in Fig. 3.16; this rated field current value is used in the analysis in the rest of the thesis.
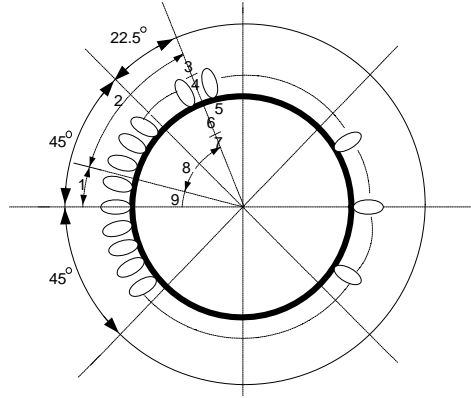
Fig. 3.15. Average route of magnetic field and region division.

Table 3.1 Calculated results of MMF drops in specific regions.

MMF (At) / B(T)	F_{air}	F_4	F_3	F_2	F_1	F_6	F_7	F_8	F_9	F_{tot}	I_F
0.05	46.5	0.35	0.24	2.4	0.76	0.68	0.16	0.9	0.28	49.87	0.22
0.1	93	0.5	0.29	3.34	1.05	0.9	0.24	1.15	0.4	100.87	0.45
0.2	186	0.67	0.39	4.74	1.63	1.28	0.33	1.6	0.5	196.87	0.88
0.3	279	0.83	0.46	6.54	3.1	2.58	0.39	2.38	1.1	296.38	1.32
0.4	372	1.02	0.54	11.34	17.2	8.67	0.46	3.75	3.6	418.58	1.86
0.5	465	1.275	0.61	33.36	216.65	153	0.54	8.09	51.8	930.33	4.14
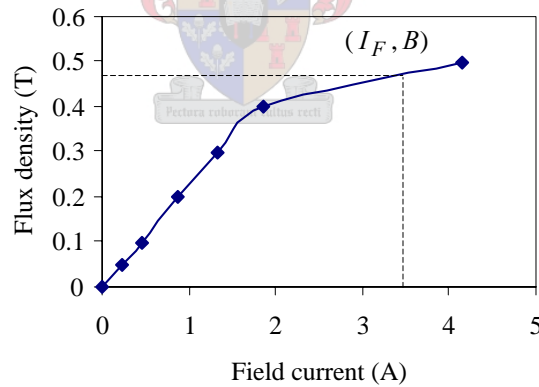
Fig. 3.16. Flux density versus field current.

3.7   Field MMF harmonic analysis with time and space distribution

Due to the fact that the *field* MMF across the core and air gap plays an important role in the air gap field intensity (or flux density) and the developed torque of the machine, this section investigates the *field* MMF harmonic content of the six-phase IDCM. The harmonic analysis refers to the time and space distributions of respectively the stator field currents and the winding function [54 - 57]. To complete this task, the winding functions and Fourier series of

the phase currents are necessary, as described in the next section. From this a resultant MMF expression can be obtained to analyze the MMF harmonics in space and time.

3.7.1   *Spatial harmonics of six-phase concentrated winding induction machine*

A cross section of a two-pole, six-phase induction machine with stator phase windings is shown in Fig. 3.17. Concentrated windings are assumed to simplify the analysis. The axis of phase *a* is used as the reference point for the circumference angle θ to define the winding function $N(\theta)$ as shown in Fig. 3.18, where N_s is the number of turns per pole per phase. The winding function waveforms of phases *b, c, d, e*, and *f* can be obtained by shifting the waveform by $\pi/6$, $4\pi/6$, $5\pi/6$, $8\pi/6$ and $9\pi/6$ respectively out of phase with phase *a*.

The Fourier series of the six-phase stator winding functions are given as follows:

$$N_a(\theta) = \sum_{n=1}^{\infty} (\frac{2N_s}{n\pi}) \sin(n\theta) \tag{3.24}$$

$$N_b(\theta) = \sum_{n=1}^{\infty} (\frac{2N_s}{n\pi}) \sin(n(\theta - \frac{\pi}{6})) \tag{3.25}$$

$$N_c(\theta) = \sum_{n=1}^{\infty} (\frac{2N_s}{n\pi}) \sin(n(\theta - \frac{4\pi}{6})) \tag{3.26}$$

$$N_d(\theta) = \sum_{n=1}^{\infty} (\frac{2N_s}{n\pi}) \sin(n(\theta - \frac{5\pi}{6})) \tag{3.27}$$

$$N_e(\theta) = \sum_{n=1}^{\infty} (\frac{2N_s}{n\pi}) \sin(n(\theta - \frac{8\pi}{6})) \tag{3.28}$$

$$N_f(\theta) = \sum_{n=1}^{\infty} (\frac{2N_s}{n\pi}) \sin(n(\theta - \frac{9\pi}{6}))   \quad , \tag{3.29}$$

where $n = 1, 3, 5, \cdots, \infty$. Since the winding function is symmetric, even harmonics do not exist. Eqns (3.24) - (3.29) will be used in the next section to calculate the inductances.
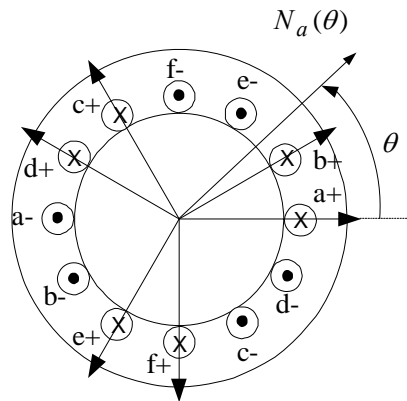
Fig. 3.17. Cross-section of a six-phase machine with concentrated stator winding.
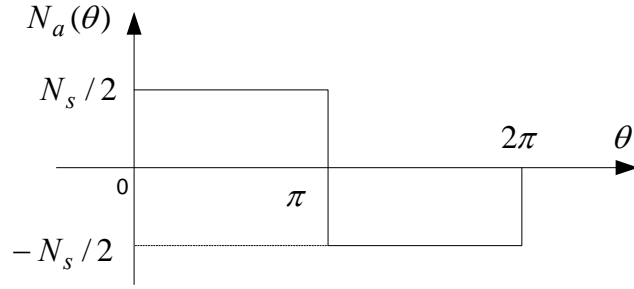
Fig. 3.18. Winding function of phase *a* of six-phase IDCM machine.

3.7.2   Time harmonic analysis of six-phase currents

Under ideal conditions the magnetic effects of the stator torque current component and the rotor induced current are cancelled by each other; this aspect will be dealt with clearly in Chapter 4. It is, thus, reasonable to consider only the stator field current component in the phase currents in the time harmonic analysis. Further for simplicity, the six-phase field currents are approximated to be square (rectangular) waveforms as shown in Fig. 3.19.

Let's take phase *a* as an example as shown in Fig. 3.20; the other phase currents follow the same pattern but with a certain phase displacement. The coefficients of the Fourier series of the waveform can be determined mathematically as,

$$A_n = \frac{1}{\pi}[\int_{\frac{\pi}{12}}^{\frac{5\pi}{12}} (I_F \sin(n(\omega t))d(\omega t) + \int_{\frac{13\pi}{12}}^{\frac{17\pi}{12}} (-I_F \sin(n(\omega t)))d(\omega t)]$$

(3.30)

$$= \frac{4I_F}{n\pi} \sin n\frac{\pi}{6} \sin n\frac{\pi}{4}$$

$$B_n = 0 \quad ,$$

(3.31)

where *n* is the harmonic order of the stator winding function and $n = 1, 3, 5, \cdots, \infty$. Hence the Fourier series of the six-phase currents are given as in eqns (3.32) - (3.37).

$$i_{af} = \sum_{m=1}^{\infty} ((\frac{4I_F}{m\pi}) \sin(m\frac{\pi}{6}) \sin(m\frac{\pi}{4})) \sin(m(\omega t))$$

(3.32)

$$i_{bf} = \sum_{m=1}^{\infty} ((\frac{4I_F}{m\pi}) \sin(m\frac{\pi}{6}) \sin(m\frac{\pi}{4})) \sin(m(\omega t - \frac{\pi}{6}))$$

(3.33)

37

$$i_{cf} = \sum_{m=1}^{\infty} ((\frac{4I_F}{m\pi})\sin(m\frac{\pi}{6})\sin(m\frac{\pi}{4}))\sin(m(\omega t - \frac{4\pi}{6})) \tag{3.34}$$

$$i_{df} = \sum_{m=1}^{\infty} ((\frac{4I_F}{m\pi})\sin(m\frac{\pi}{6})\sin(m\frac{\pi}{4}))\sin(m(\omega t - \frac{5\pi}{6})) \tag{3.35}$$

$$i_{ef} = \sum_{m=1}^{\infty} ((\frac{4I_F}{m\pi})\sin(m\frac{\pi}{6})\sin(m\frac{\pi}{4}))\sin(m(\omega t - \frac{8\pi}{6})) \tag{3.36}$$

$$i_{ff} = \sum_{m=1}^{\infty} ((\frac{4I_F}{m\pi})\sin(m\frac{\pi}{6})\sin(m\frac{\pi}{4}))\sin(m(\omega t - \frac{9\pi}{6})) \tag{3.37}$$

where m is the harmonic order of the stator field currents and $m = 1, 3, 5, \cdots, \infty$. Because the current waveforms are symmetric, the even harmonics do not exist.
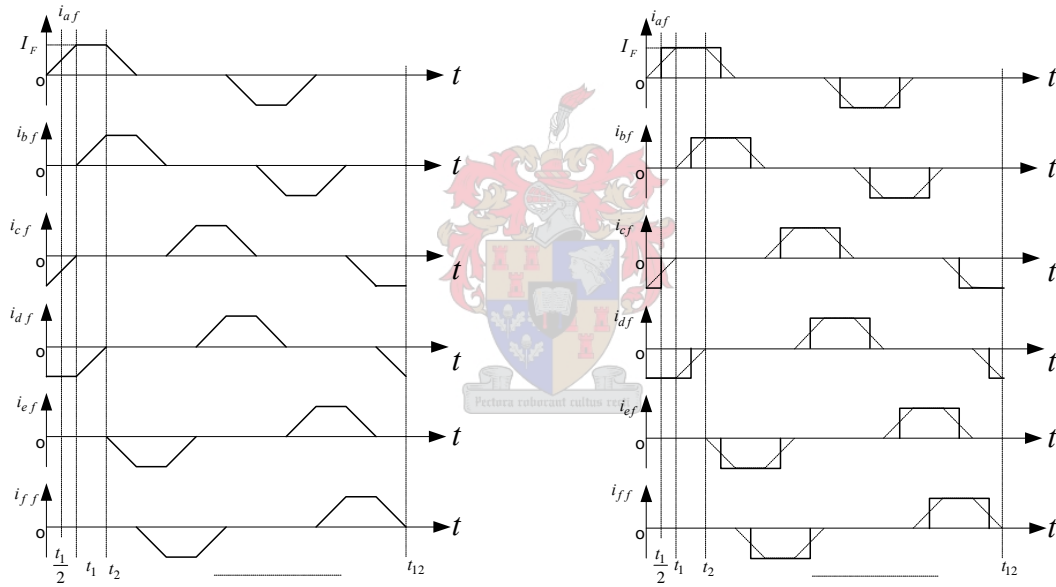
(a) Field current waveforms   (b) Approximated field current waveforms

Fig. 3.19. Six-phase field current waveforms.
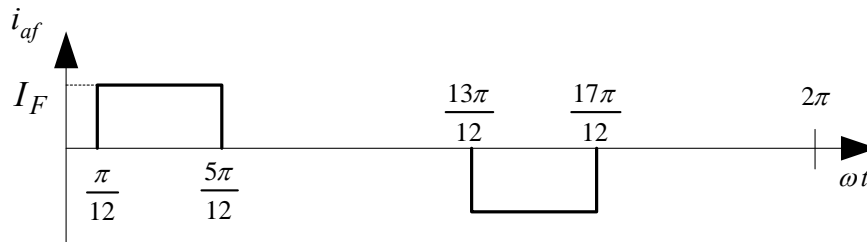
Fig. 3.20. Phase *a* current waveform.

3.7.3   *MMF harmonics analysis with only field current*

The resultant air gap MMF produced by the six phases $a - f$ is obtained by

$$F = F_a + F_b + F_c + F_d + F_e + F_f = \sum_{i=a}^{f} N_i(\theta) i_{if} \quad , \tag{3.38}$$

where, $i = a$, b, c, d, e, f. Eqn (3.38) can be expanded by substituting the winding function eqns (3.24) - (3.29) and field current eqns (3.32) - (3.37) as follows:

$$F = \sum_{n=1}^{\infty} \sum_{m=1}^{\infty} \left(\frac{1}{nm}\right)\left(\frac{4}{\pi}\right)^2 \left(\frac{N_s I_F}{2}\right) \sin(m\frac{\pi}{6})\sin(m\frac{\pi}{4})[\ \sin(n\theta)\ \sin m(\omega t) + \sin n(\theta - \frac{\pi}{6})\ \sin m(\omega t - \frac{\pi}{6})$$

$$+ \sin n(\theta - \frac{4\pi}{6})\ \sin m(\omega t - \frac{4\pi}{6}) + \sin n(\theta - \frac{5\pi}{6})\sin m(\omega t - \frac{5\pi}{6})$$

$$+ \sin n(\theta - \frac{8\pi}{6})\ \sin m(\omega t - \frac{8\pi}{6}) + \sin n(\theta - \frac{9\pi}{6})\sin m(\omega t - \frac{9\pi}{6})\ ]$$

$$= \sum_{n=1}^{\infty} \sum_{m=1}^{\infty} \left(\frac{1}{nm}\right)\left(\frac{4}{\pi}\right)^2 \left(\frac{N_s I_F}{2}\right) \sin(m\frac{\pi}{6})\sin(m\frac{\pi}{4})[3\cos(n\theta - m(\omega t))$$

$$+ \cos(n\theta + m(\omega t) - (m+n)\frac{9\pi}{6})\ (\cos(n+m)\frac{9\pi}{6} + \cos(n+m)\frac{7\pi}{6} + \cos(m+n)\frac{\pi}{6})]$$

$$\tag{3.39}$$

The two major terms in the square brackets in the above expression represent a pair of air-gap fields. The first term $cos(n\theta - m(\omega t))$ is the rotating forward field MMF and the other term $cos(n\theta + m(\omega t) - (m+n)9\pi/6)$ is the rotating backward field MMF.

The relation between the field space harmonics and current time harmonics for the concentrated six-phase winding is given numerically in Table 3.2. The following conclusions can be drawn:

(i)   The same order space and time harmonics produce the forward rotating MMFs.

(ii)   All harmonics with a number of $6k$ ($k = 1$, 3, 5…) are removed in the six-phase induction machine.

(iii)   The higher order space and time harmonics have little effect on the MMF and torque performance of the six-phase IDCM.

Table 3.2. Per unit MMF versus space and time harmonics for concentrated

six-phase windings

Space⟍Time	1	3	5	7	9	11	13	15	17
1	**0.8605**	0.2869	0	0.1229	0.0956	0	0.0662	0.0574	0
3	0.574	**0**	0.1147	0.082	0	0.052	0.044	0	0.034
5	0	0.0574	**0.0344**	0	0.0191	0.0156	0	0.0115	0.0101
7	0.1129	0.0409	0	**0.01756**	0.0137	0	0.0095	0.0082	0.0072
9	0.191	0	0.038	0.027	**0**	0.0174	0.0147	0	0.0112
11	0	0.026	0.0156	0	0.0087	**0.0071**	0	0.0052	0.0044
13	0.066	0.022	0	0.0095	0.0074	00.0051	**0.0044**	0.0039	0
15	0.125	0	0.023	0.16	0	0.010	0.009	**0**	0.007
17	0	0.017	0.010	0	0.006	0.0005	0	0.003	0.0026

Multiply all entries by $N_s\,I_F$ to get the true MMF

3.8   Calculation of stator inductances

In the dynamic analysis the stator inductance plays an important role, hence, it is necessary to analyse the stator inductance by using the winding function. Taking into account the dominant harmonics only (i.e. the fundamental and third harmonics as is clear from Fig. 3.18), the winding functions of the six-phase stator windings as given by eqns (3.24) - (3.29) can be simplified as,

$$N_{as}(\theta) = N_{s1}\sin\theta + N_{s3}\sin 3\theta \tag{3.40}$$

$$N_{bs}(\theta) = N_{s1}\sin(\theta - \frac{\pi}{6}) + N_{s3}\sin 3(\theta - \frac{\pi}{6}) \tag{3.41}$$

$$N_{cs}(\theta) = N_{s1}\sin(\theta - \frac{4\pi}{6}) + N_{s3}\sin 3(\theta - \frac{4\pi}{6}) \tag{3.42}$$

$$N_{ds}(\theta) = N_{s1}\sin(\theta - \frac{5\pi}{6}) + N_{s3}\sin 3(\theta - \frac{5\pi}{6}) \tag{3.43}$$

$$N_{es}(\theta) = N_{s1}\sin(\theta - \frac{8\pi}{6}) + N_{s3}\sin 3(\theta - \frac{8\pi}{6}) \tag{3.44}$$

$$N_{fs}(\theta) = N_{s1}\sin(\theta - \frac{9\pi}{6}) + N_{s3}\sin 3(\theta - \frac{9\pi}{6}) \;, \tag{3.45}$$

where N_{s1} and N_{s3} are equivalent stator turns per phase per pole for the fundamental and the third harmonics, respectively.

In the following analysis the air gap is assumed to be uniform. The permeability of the stator and rotor irons is assumed to be infinite and saturation and iron losses, as well as end winding

and slotting effects, are neglected. Therefore the self- or mutual inductances [58] between any two stator windings can be expressed in terms of their winding functions as

$$L_{ij} = \frac{\mu_0 \, r l}{l_g} \int_0^{2\pi} N_i(\theta) \, N_j(\theta) \, d\theta \, .$$

(3. 46)

The self-inductances of the stator are readily calculated by the integral as follows:

$$
\begin{aligned}
L_a &= \frac{\mu_0 \, r l}{l_g} \int_0^{2\pi} (N_{as}(\theta))^2 \, d\theta \\
&= \frac{\mu_0 \, r l}{l_g} \int_0^{2\pi} ((N_{s1}\sin\theta)^2 + (N_{s3}\sin 3\theta)^2 + 2 N_{s1} \, N_{s3} \sin\theta \sin 3\theta) \, d\theta \\
&= \frac{\mu_0 \, r l}{l_g} \left[\frac{N_{s1}^2}{2} \left[\theta - \frac{1}{2}\sin 2\theta \right]_0^{2\pi} + \frac{N_{s3}^2}{2} \left[\theta - \frac{1}{6}\sin 6\theta \right]_0^{2\pi} \right] \\
&= \frac{\mu_0 \, r l \, \pi}{l_g} (N_{s1}^2 + N_{s3}^2) \\
&= L_{ms1} + L_{ms3}
\end{aligned}
$$

(3.47)

$$L_b = L_c = L_d = L_e = L_f = L_a = L_{ms1} + L_{ms3}$$

(3.48)

The mutual inductances between the stator phases are defined by the integral as

$$
\begin{aligned}
L_{ab} &= \frac{\mu_0 \, r l}{l_g} \int_0^{2\pi} (N_{as}(\theta) \, N_{bs}(\theta)) \, d\theta \\
&= \frac{\mu_0 \, r l}{l_g} \int_0^{2\pi} (N_{s1}\sin\theta + N_{s3}\sin 3\theta)(N_{s1}\sin(\theta - \frac{\pi}{6}) + N_{s3}\sin 3(\theta - \frac{\pi}{6})) \, d\theta \\
&= \frac{\mu_0 \, r l \, \pi}{l_g} (N_{s1}^2) \cos\frac{\pi}{6} \\
&= L_{ms1} \cos\frac{\pi}{6}
\end{aligned}
$$

(3.49)

$$L_{bc} = L_{cd} = L_{de} = L_{ef} = L_{ab} = L_{ms1} \cos\frac{\pi}{6}$$

(3.50)

$$
\begin{aligned}
L_{ac} &= \frac{\mu_0 \, r l}{l_g} \int_0^{2\pi} (N_{as}(\theta) \, N_{cs}(\theta)) \, d\theta \\
&= \frac{\mu_0 \, r l}{l_g} \int_0^{2\pi} (N_{s1}\sin\theta + N_{s3}\sin 3\theta)(N_{s1}\sin(\theta - \frac{4\pi}{6}) + N_{s3}\sin 3(\theta - \frac{4\pi}{6})) \, d\theta \\
&= \frac{\mu_0 \, r l \, \pi}{l_g} [(N_{s1}^2)\cos\frac{4\pi}{6} + N_{s3}^2] \\
&= L_{ms1} \cos\frac{4\pi}{6} + L_{ms3}
\end{aligned}
$$

(3.51)

$$L_{bd} = L_{ce} = L_{df} = L_{ac} = L_{ms1} \cos\frac{4\pi}{6} + L_{ms3}$$

(3.52)

$$L_{ad} = \frac{\mu_0\, r\, l}{l_g} \int\limits_0^{2\pi} (N_{as}(\theta)\, N_{ds}(\theta))\, d\theta$$

$$= \frac{\mu_0\, r\, l}{l_g} \int\limits_0^{2\pi} (N_{s1}\sin\theta + N_{s3}\sin 3\theta)(N_{s1}\sin(\theta - \frac{5\pi}{6}) + N_{s3}\sin 3(\theta - \frac{5\pi}{6}))\, d\theta$$

$$= \frac{\mu_0\, r\, l\, \pi}{l_g}(N_{s1}^2)\cos\frac{5\pi}{6}$$

$$= L_{ms1}\cos\frac{5\pi}{6}$$

(3.53)

$$L_{be} = L_{cf} = L_{ad} = L_{ms1}\cos\frac{5\pi}{6}$$

(3.54)

$$L_{ae} = \frac{\mu_0\, r\, l}{l_g} \int\limits_0^{2\pi} (N_{as}(\theta)\, N_{es}(\theta))\, d\theta$$

$$= \frac{\mu_0\, r\, l}{l_g} \int\limits_0^{2\pi} (N_{s1}\sin\theta + N_{s3}\sin 3\theta)(N_{s1}\sin(\theta - \frac{8\pi}{6}) + N_{s3}\sin 3(\theta - \frac{8\pi}{6}))\, d\theta$$

$$= \frac{\mu_0\, r\, l\, \pi}{l_g}[(N_{s1}^2)\cos\frac{8\pi}{6} + N_{s3}^2]$$

$$= L_{ms1}\cos\frac{8\pi}{6} + L_{ms3}$$

(3.55)

$$L_{bf} = L_{ae} = L_{ms1}\cos\frac{8\pi}{6} + L_{ms3}$$

(3.56)

$$L_{af} = \frac{\mu_0\, r\, l}{l_g} \int\limits_0^{2\pi} (N_{as}(\theta)\, N_{fs}(\theta))\, d\theta$$

$$= \frac{\mu_0\, r\, l}{l_g} \int\limits_0^{2\pi} (N_{s1}\sin\theta + N_{s3}\sin 3\theta)(N_{s1}\sin(\theta - \frac{9\pi}{6}) + N_{s3}\sin 3(\theta - \frac{9\pi}{6}))\, d\theta$$

$$= \frac{\mu_0\, r\, l\, \pi}{l_g}(N_{s1}^2)\cos\frac{9\pi}{6}$$

$$= L_{ms1}\cos\frac{9\pi}{6}$$

(3.57)

The armature reaction effect of the rotor induced current is cancelled by the stator torque current component (Fig. 3.5); it is thus reasonable to ignore the mutual inductance from the rotor side. Thus, the stator magnetizing inductances of the six-phase induction machine are given by

$$L_S = \begin{bmatrix} L_a & L_{ab} & L_{ac} & L_{ad} & L_{ae} & L_{af} \\ L_{ba} & L_b & L_{bc} & L_{bd} & L_{be} & L_{bf} \\ L_{ca} & L_{cb} & L_c & L_{cd} & L_{ce} & L_{cf} \\ L_{da} & L_{db} & L_{dc} & L_d & L_{de} & L_{df} \\ L_{ea} & L_{eb} & L_{ec} & L_{ed} & L_e & L_{ef} \\ L_{fa} & L_{fb} & L_{fc} & L_{fd} & L_{fe} & L_{fs} \end{bmatrix}$$

$$= L_{ms1} \begin{bmatrix} 1 & \cos\frac{\pi}{6} & \cos\frac{4\pi}{6} & \cos\frac{5\pi}{6} & \cos\frac{8\pi}{6} & \cos\frac{9\pi}{6} \\ \cos\frac{\pi}{6} & 1 & \cos\frac{\pi}{6} & \cos\frac{4\pi}{6} & \cos\frac{5\pi}{6} & \cos\frac{8\pi}{6} \\ \cos\frac{4\pi}{6} & \cos\frac{\pi}{6} & 1 & \cos\frac{\pi}{6} & \cos\frac{4\pi}{6} & \cos\frac{5\pi}{6} \\ \cos\frac{5\pi}{6} & \cos\frac{4\pi}{6} & \cos\frac{\pi}{6} & 1 & \cos\frac{\pi}{6} & \cos\frac{4\pi}{6} \\ \cos\frac{8\pi}{6} & \cos\frac{5\pi}{6} & \cos\frac{4\pi}{6} & \cos\frac{\pi}{6} & 1 & \cos\frac{\pi}{6} \\ \cos\frac{9\pi}{6} & \cos\frac{8\pi}{6} & \cos\frac{5\pi}{6} & \cos\frac{4\pi}{6} & \cos\frac{\pi}{6} & 1 \end{bmatrix} + L_{ms3} \begin{bmatrix} 1 & 0 & 1 & 0 & 1 & 0 \\ 0 & 1 & 0 & 1 & 0 & 1 \\ 1 & 0 & 1 & 0 & 1 & 0 \\ 0 & 1 & 0 & 1 & 0 & 1 \\ 1 & 0 & 1 & 0 & 1 & 0 \\ 0 & 1 & 0 & 1 & 0 & 1 \end{bmatrix} \tag{3.58}$$

With the parameters of the six-phase, 2-pole induction machine under consideration equal to: N_s =249 turns; l = 128 mm; l_g = 0.5 mm and r = 49 mm, the theoretical calculated inductances of phase a based on eqns (3.47), (3.49), (3.51), (3.53), (3.55), (3.57) are as given in Table 3.3. These results will be compared to the finite element analysis results in Chapter 4.

Table 3.3. Phase a inductances.

Self-inductance (H)	Mutual-inductance (H)				
L_a	L_{ab}	L_{ac}	L_{ad}	L_{ae}	L_{af}
1.37	1.068	- 0.479	- 1.068	- 0.479	0

3.9   Summary

In this chapter a special phase current waveform for a six-phase IDCM was proposed and analyzed. This current waveform was derived considering the dc motor control principle with separately excited field and armature currents, as well as the advantage of a rectangular flux density waveform in the air gap of the induction motor. The field intensity in the air gap was discussed for an IDCM model as defined in this chapter. The electromagnetic torque production principle was also described and a torque equation was derived. With the torque equation, the torque was calculated by using the specific six-phase IDCM parameters. The field current amplitude was analyzed by considering the effect of stator and rotor iron core saturation. The field MMF harmonics were analyzed by using an approximate method. The important conclusion is that all the harmonics are forward field MMFs. Lastly the stator phase

inductances of the IDCM were presented. Some of the calculated results of this chapter (e.g. developed torque, field current amplitude etc.) will be compared with the results from finite element analysis and measurements in the next chapters.
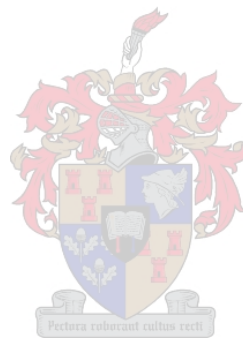
4   FINITE ELEMENT ANALYSIS

Chapter 3 presented the theoretical analysis of the induction dc motor (IDCM). This chapter describes the numerical analysis of the six-phase IDCM using a finite element (FE) package [33] and presents a mathematical model for the machine using natural variables. In the FE analysis the air gap flux density and electromagnetic torque of the IDCM are investigated, as well as the balanced flux linkage condition and induced rotor voltage. The parameters of the per phase equivalent circuit are also determined through FE analysis.

4.1   FE modelling of six-phase IDCM

The FE software used is not of the commercial variety. It makes use of triangular elements of the first order. Only one pole (stator and rotor) of the machine is meshed with one air gap macro-element [59, 60] comprising nodals on both sides of the air gap. A time-saving scheme has been devised [33, 61] that makes the use of one air gap element very attractive as a means to model rotor movement. The Newton-Phapson method is used for the solution of the set of non-linear equations.

Due to the symmetry of the proposed machine, only one pole of the machine cross section needs to be represented. Fig. 4.1 shows the winding layout with its corresponding slots. The figure also shows the portion of the machine used in the FE analysis. Using this one portion reduces the number of elements and nodes and decreases the FE computational time. The vector potentials in the entire machine can be obtained from the solved one pole part by using the symmetry applied. Fig. 4.2 shows the one pole part of the machine used in the FE analysis and the boundary conditions. Dirichlet boundary conditions with zero vector potential are set to the outer stator and inner rotor shaft. By doing this, the solution is confined inside the machine frame. Anticyclic boundary conditions are set to the symmetry cut lines [62].

For the FE analysis, the mesh generation is completed as shown in Fig. 4.3. Only one stator slot of the machine is outlined in terms of xy-coordinates and meshed and mirrored to the number of slots over a pole pitch. The phase windings are then allocated to the slots. Also, one half of a pole of the rotor is outlined and meshed and mirrored to the other half pole. The stator and rotor meshes are then joined. The FE analysis in this chapter is based on the model of Fig. 4.3. Fig. 4.4 shows a typical plot of flux lines.

slot	1	2	3	4	5	6	7	8	9	10	11	12	13	14	15	16	17	18	19	20	21	22	23	24	25	26	27	28	29	30	31	32	33	34	35	36

phase coils: a+, a+, a+, b+, b+, b+, e-, e-, e-, f-, f-, f-, c+, c+, c+, d+, d+, d+, a-, a-, a-, b-, b-, b-, e+, e+, e+, f+, f+, f+, c-, c-, c-, d-, d-, d-

FE representation
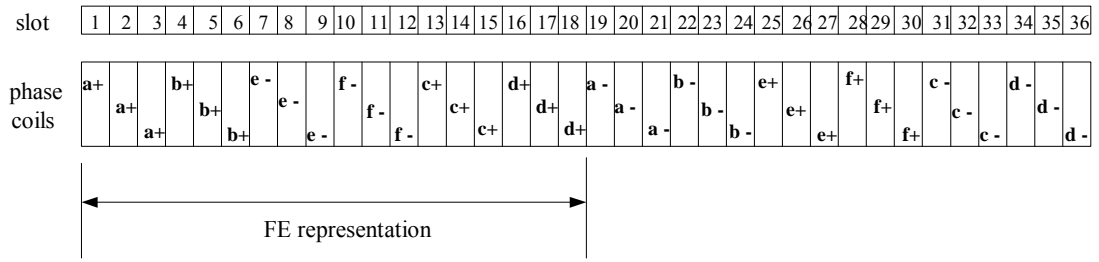
Fig. 4.1. Stator winding diagram and portion (18 slots) analysed.
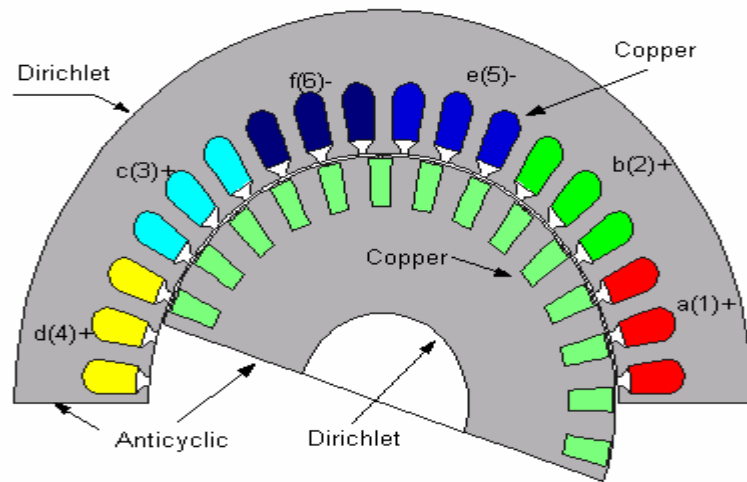
Fig. 4.2. Six-phase IDCM geometry and boundary condition.
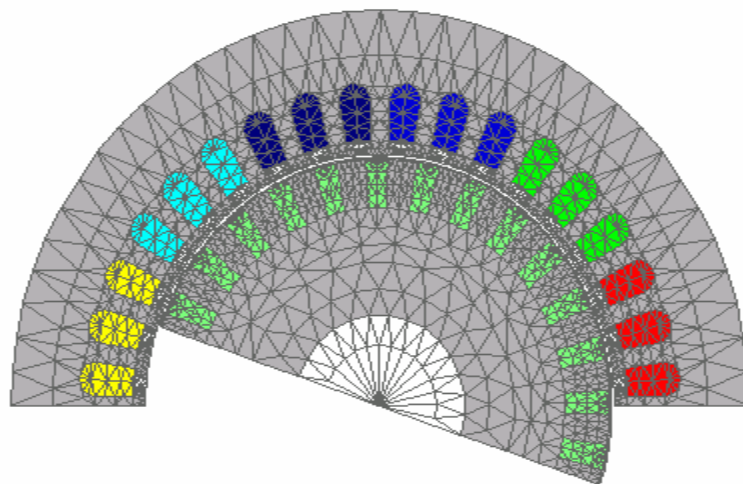
Fig. 4.3. Mesh used in the FE analysis.

46
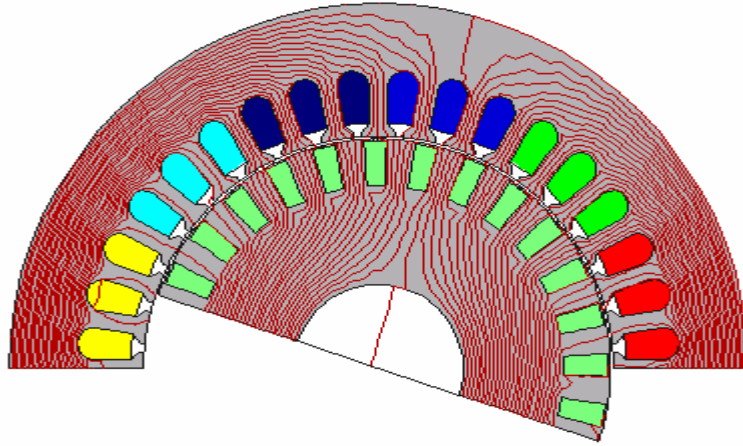
Fig. 4.4. Flux lines for magneto-static situation with only field current.

4.2   Analysis of the air gap flux density

Due to the importance of the flux density distribution in the air gap relevant to the electromagnetic torque performance, the air gap flux density characteristic is evaluated in terms of the following aspects:

- Flux density amplitude versus field current;
- Flux density waveform at different field current positions;
- Flux density waveform under balanced condition of torque versus rotor current.

4.2.1   Flux density amplitude versus field current

The six-phase stator currents with only field current components are shown in Fig. 4.5. The flux density versus field current characteristic is investigated at time $t = t_l/2$, which means that the six-phase current setup is: $i_a = -i_c =-i_d/2 = I_F /2$ and $i_b = i_e = i_f = 0$. The effect of skew is taken into account in this 2-D FE solution by using a set of unskewed machines of which the rotors are displaced by an angle that is a fraction of the total skew. The rotor of Fig. 4.2 is skewed by one stator slot pitch. The different values of the amplitude of the flux density in the air gap can be obtained by changing I_F. The result of the air gap flux density calculation at $I_F =$ 3.5 A is shown in Fig. 4.6; the flux line plot inside the motor for the given stator current setup has already been shown in Fig. 4.4.

The flux density waveform obtained from FE analysis is filtered by a low pass filter in Matlab software. The low pass filter program used in Matlab is

```
load bgap.txt
x1=bgap(:,2);
t1=bgap(:,1);
```

47

```
[B,A]=butter(2,2/80, 'low');
y1=filter(B,A, x1);
csvwrite('bgapf.txt', y1)
```

In this manner, a plot to demonstrate B versus I_F can be obtained as shown in Fig. 4.7.
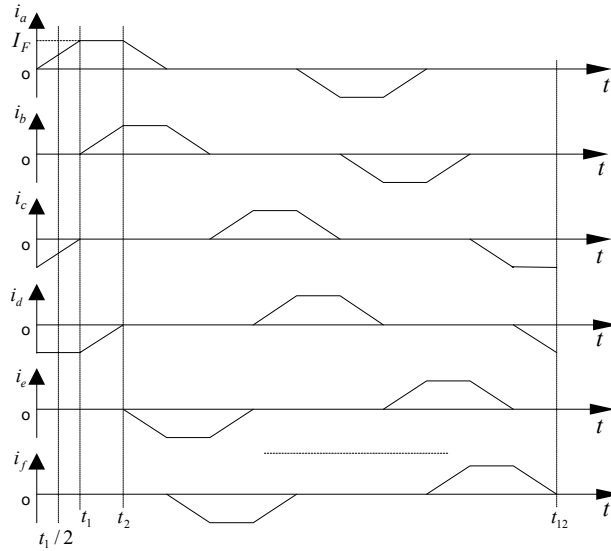
Fig. 4.5. Six-phase stator current waveforms with only field components.

Position (deg.)
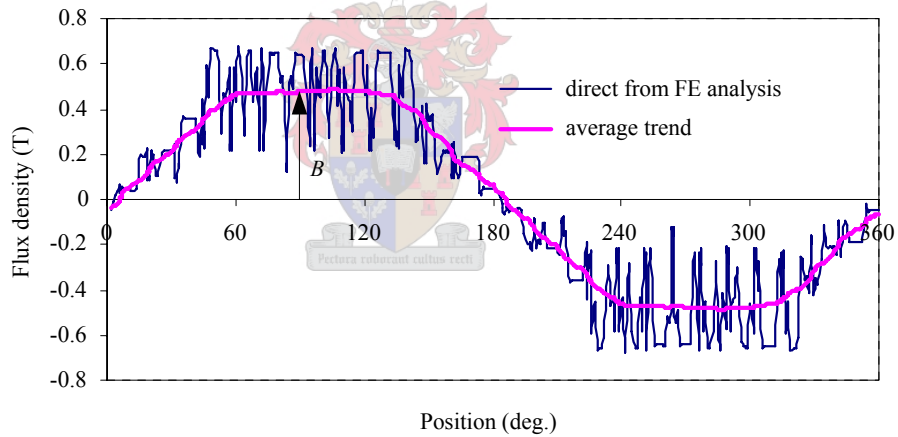
Fig. 4.6. Flux density distribution in the air gap.

Field current amplitude (A)
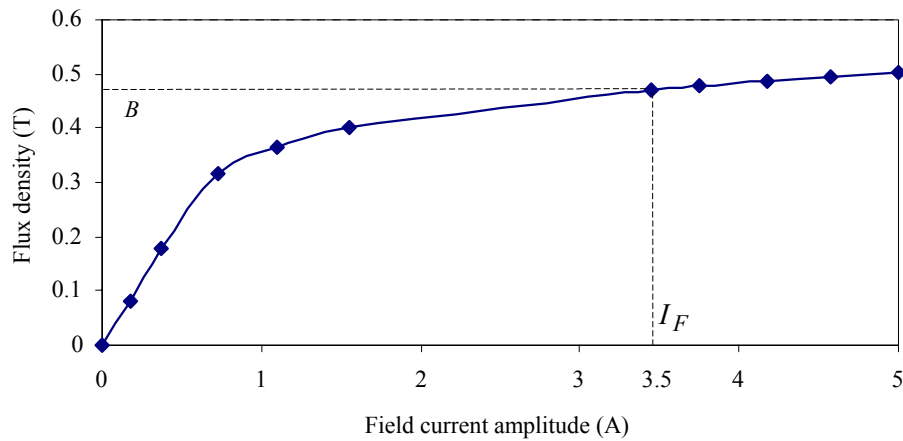
Fig. 4.7. Flux density versus field current amplitude.

It can be seen from Fig. 4.6 that the average radial component of the air gap flux density shows a quasi-square waveform with a flat-topped amplitude of value *B*. Also clear from Fig. 4.7, is the relatively high field current of I_F = 4.5A necessary to obtain a flux density of 0.5 T in the air gap. This will cause heavy saturation in the small stator and rotor iron yokes of the machine; note that the machine has been changed from a standard 4-pole machine to a 2-pole machine. Hence, I_F = 3.5 A is selected in the FE analysis (also in the theoretical analysis in Chapter 3) to decrease the level of saturation.

4.2.2   Flux density waveform at different stator field current positions

For clarity, the current waveform for the time region 0 - t_1 in Fig. 4.5 is enlarged as shown in Fig. 4.8. The current amplitude, I_F, is kept constant at 3.5A. The amplitude and the plateau width of the flux density waveform are investigated by inputting the active three-phase current values, i_{af}, i_{cf} and i_{df} at times 0 - t_1. In Fig. 4.9 the average radial component of the air gap flux density is shown at different times and different phase current values of the currents in Fig. 4.8. At time $t = 0$ the field phase currents are $i_c = i_d = -I_F$, while at time $t = t_1/2$ the phase currents are $i_a = -i_c = I_F/2$ and $i_d = -I_F$ with I_F = 3.5A. It is clear that the flux density waveform moves (rotates) synchronously with change in phase current, but the flat-topped amplitude *B* slightly varies with angular position between 0.43 - 0.46 T.
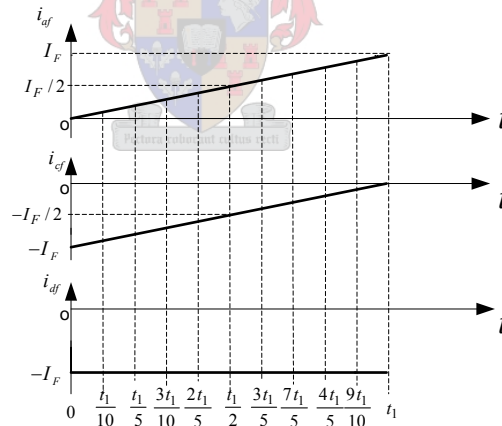
Fig. 4.8. Enlarged plot of three-phase currents in the time region 0 - t_1.
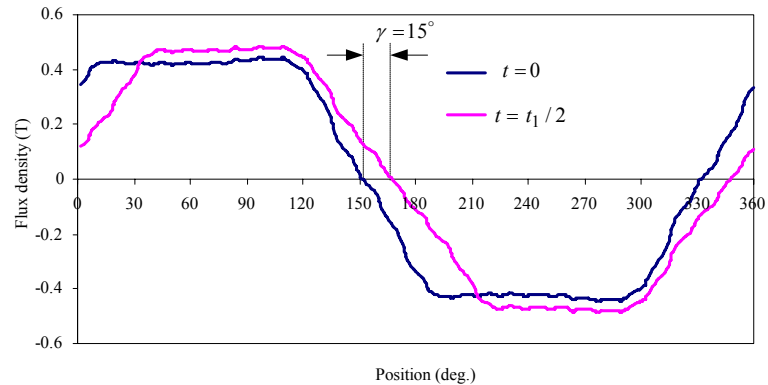
Fig. 4.9. Average air gap flux density at different times and phase currents

49

Fig. 4.10 shows the amplitude and plateau angle values of *B* versus the angular position of the flux density waveform. It can be seen from Fig. 4.10 that there is a ripple in *B* of frequency $12f_1$, where f_1 is the fundamental frequency of the phase current. This will induce a high frequency voltage in the rotor phase windings, which will be dealt with in section 4.6. It is also shown in Fig. 4.10 (b) that the plateau angle varies between 90 and 104 degrees.
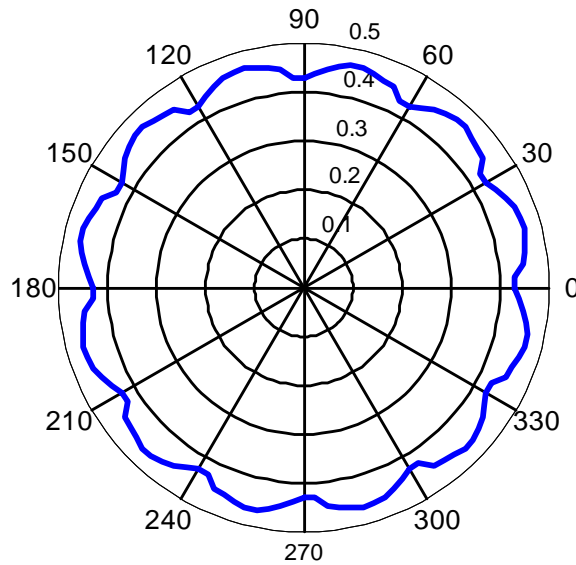
(a) Amplitude.
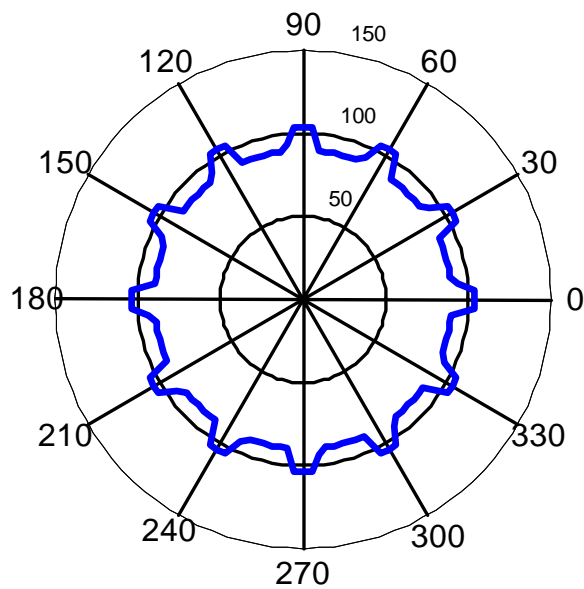
(b) Plateau angle.

Fig. 4.10. Values of amplitude and plateau angle of flux density in the air gap versus angular position.

4.2.3   Flux density distribution with stator torque and rotor currents

What will happen to the flux density distribution in the air gap when the stator torque current and balanced rotor current are supplied? Fig. 4.11 shows the flux lines and flux density distribution at rated load condition, that is I_F = 3.5 A, I_T = 2.2 A and I_r = 5.6 A [the latter two values are from the theoretical analysis in Appendix B, calculated at rated slip].

When comparing the flux line plot of Fig. 4.11(a) (rated load condition) with the plot of Fig. 4.4 (no-load condition with only field current), as well as the air gap flux density distribution of Fig. 4.6 (only field current) with that of Fig. 4.11(b) (rated load condition), a distortion can be seen in the flux plot and air gap flux density distribution. This distortion can be due to the fact that the stator torque current and rotor current MMFs are not equal, as the values of the torque and rotor currents used in the FE analysis are calculated theoretically. Another critical factor is the leakage flux in the air gap of the machine, which can also cause the distortion of the air gap flux density distribution. The balanced flux linkage issue will be investigated in detail in section 4.3.

(a) Flux line distribution.

(b)   Flux density distribution.
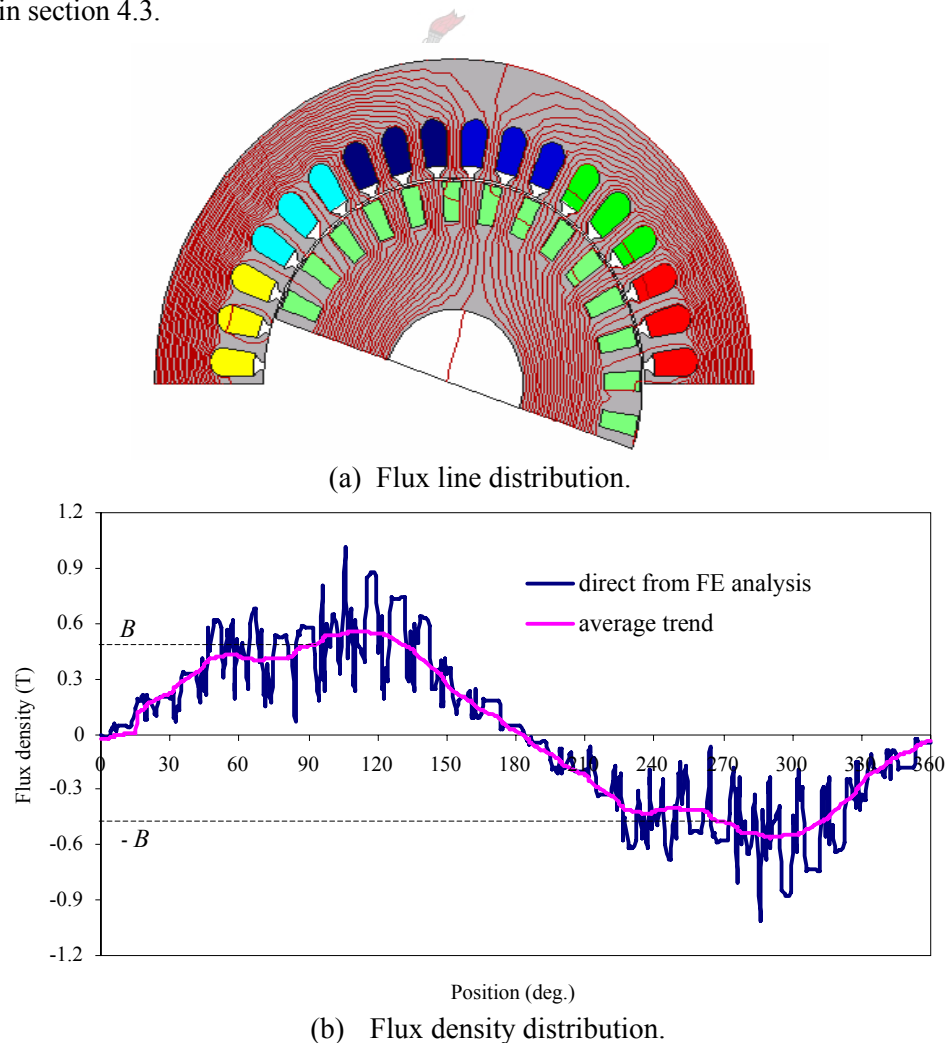
Fig. 4.11. Flux line and flux density distribution at rated load condition.

4.3   Balanced flux linkage investigation

It is important to confirm the calculation of the control gain *k* according to eqn (3.21) or more specifically the I_r/I_T current ratio according to eqn (3.20) in section 3.5. This can be done by looking at the resultant flux linkages of the active rotor phase windings and the torque producing stator phase windings; for MMF balance the quadrature flux in the machine should be zero, hence the resultant flux linkage of these two sets of windings should be zero. The per phase flux linkage λ_j of the stator or rotor winding is calculated for the skewed rotor by eqn (4.1) as

$$\lambda_j = \frac{1}{k_s} \sum_{n=1}^{k_s} \lambda_{jn}(\alpha_n) \ , \tag{4.1}$$

where $\lambda_{jn}(\alpha_n)$ is the total flux linkage of phase winding *j* with unskewed rotor *n* at position α_n, and k_s is the number of unskewed rotors. In this analysis k_s is taken as 5.

4.3.1   Specific rotor and stator torque current phases

In the FE calculation of the flux linkages it is assumed that the induced rotor phase current takes up the ideal form shown in Fig. 3.9. This implies that dc current is always flowing in seven of the fourteen rotor phases of the machine in Fig. 4.2. The position of the seven active rotor phase windings must be opposite the position of the torque phase windings of the stator. In the FE analysis, rotor phase windings 11 – 17 and stator torque phase windings 2, 5 and 6, which correspond to phases *b, e* and *f,* are made active as shown in Fig. 4.12.

The current set-up of the stator torque phase windings is $i_5 = 2i_6 = -2i_2 = 2.2A$, while the specific rotor phase currents $i_{11} = i_{12} = \cdots = i_{17} = I_r$ are varied. With this current set-up the flux linkages are investigated for these specific stator and rotor phase windings.
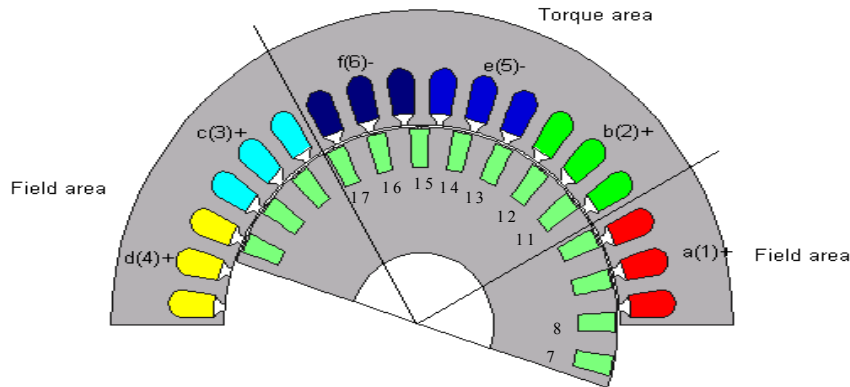
Fig. 4.12. Illustration of the filed and torque phases distribution.

4.3.2   Resultant flux linkage calculation

A. Stator phase flux linkage:

As can be seen in Fig. 4.13 (a), all the stator torque phase flux linkages are projected to λ_5 because phase winding 5 lies in the middle among the three torque phases, which are phase windings 2, 5 and 6. The formula to calculate the stator resultant phase flux linkage is

$$\lambda_{st} = -\lambda_2 \cos\beta + \lambda_5 + \lambda_6 \cos\beta, \tag{4.2}$$

where β is the angle of displacement of the stator phase windings as shown Fig. 4.13 (a).

B. Rotor phase flux linkage

As can be seen in Fig. 4.13 (b), all the active rotor phase flux linkages are projected to λ_{14} because phase winding 14 lies in the middle among the seven active rotor phase windings, which are phase windings 11 – 17. The formula to calculate the resultant rotor flux linkage is

$$\begin{aligned}\lambda_{rt} = \lambda_{11}\cos(3\alpha) + \lambda_{12}\cos(2\alpha) + \lambda_{13}\cos\alpha + \lambda_{14} + \lambda_{15}\cos\alpha \\ + \lambda_{16}\cos(2\alpha) + \lambda_{17}\cos(3\alpha)\end{aligned}, \tag{4.3}$$

where α is the angle of displacement of the rotor phase windings as shown in Fig. 4.13 (b).

The flux linkages of eqns (4.2) and (4.3) are calculated through FE analysis for the skewed rotor using eqn (4.1). In this calculation the stator torque current, I_T, was kept constant at $I_T = 2.2$ A and the rotor current I_r was varied. The calculated results of the flux linkages λ_{st} and λ_{rt} versus rotor current are shown in Fig. 4.14.

As mentioned before the theoretical calculated values of I_T and I_r under rated load conditions are $I_T = 2.2$ A and $I_r = 5.6$A; this corresponds to balanced MMF condition, which means that the stator and rotor sides should experience minimum flux linkage. Hence, the theoretical calculated balanced rotor current value can be verified by referring to Fig. 4.14(b); it can be seen that with $I_T = 2.2$ A the flux linkages of both sides become a minimum at a rotor current of $I_r = 5.8$ A. In other words, an air gap zero flux linkage condition is obtained at this rotor current. This gives a FE calculated current ratio for MMF balance equal to $I_r/I_T = 5.8/2.2 = 2.63$, which compares well with the theoretical calculated value of 2.54 according to eqn (3.20); the difference is less than 4%. This confirms, thus, the theoretical calculation of the gain k according to eqn (3.21).
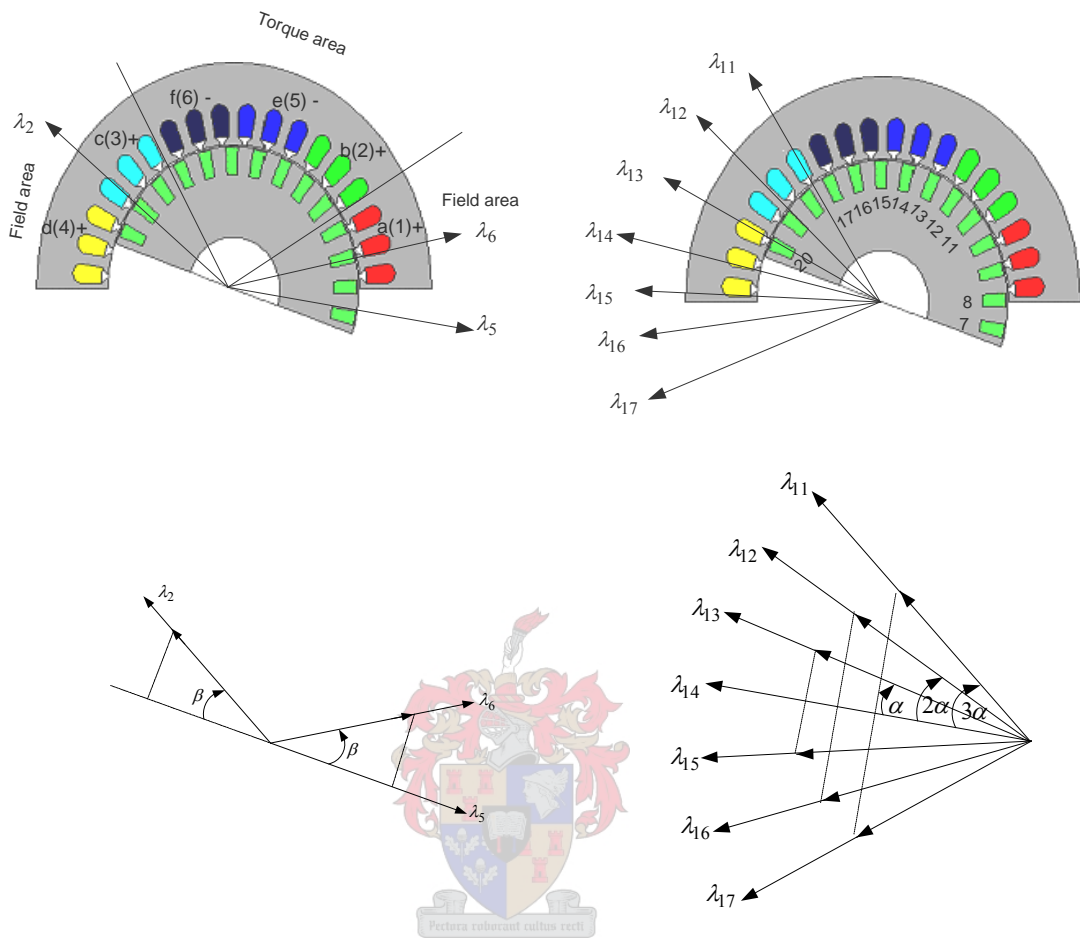
(a) Stator torque phase flux linkage vectors.   (b) Rotor torque phase flux linkage vectors.

Fig. 4.13. Plot of flux linkage vectors.
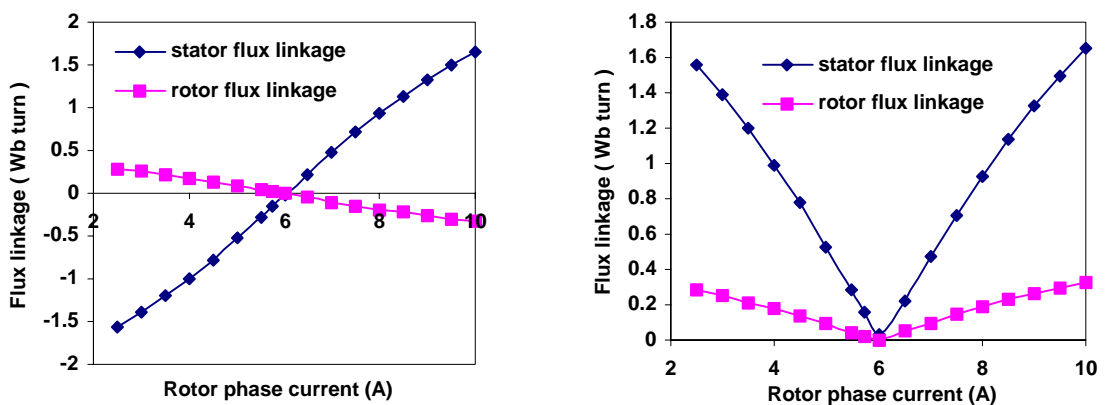
(a) Flux linkage from FE analysis.   (b) Absolute flux linkage.

Fig. 4.14. Resultant flux linkages versus rotor current.

4.4   Static electromagnetic torque evaluation

The static electromagnetic torque of the six-phase IDCM under consideration is also calculated directly from the FE solution. As in eqn (4.1) for flux linkages, the electromagnetic torque of the skewed machine is calculated by using k_s unskewed machines as

$$T_e = \frac{1}{k_s} \sum_{n=1}^{k_s} T_n \,, \tag{4.4}$$

where T_n is the torque of the n-th unskewed machine determined by the Maxwell stress tensor method. Through time-stepping FE analysis the electromagnetic torque of this machine is calculated at balance conditions, which means $2N_s\, I_T = 7\, N_r\, I_r$. The theoretical calculated values of I_T and I_r at balanced MMF condition are given in Appendix B. Using these current values, the FE electromagnetic torque versus torque current is calculated according to eqn (4.4). The results are shown in Fig. 4.15. It is clear that the torque versus torque current has a nearly linear relationship, and the ratio of T_e/ I_T is around 2.91 Nm/A (12.81/4.4). These results will be verified by practical measurement in Chapter 6.
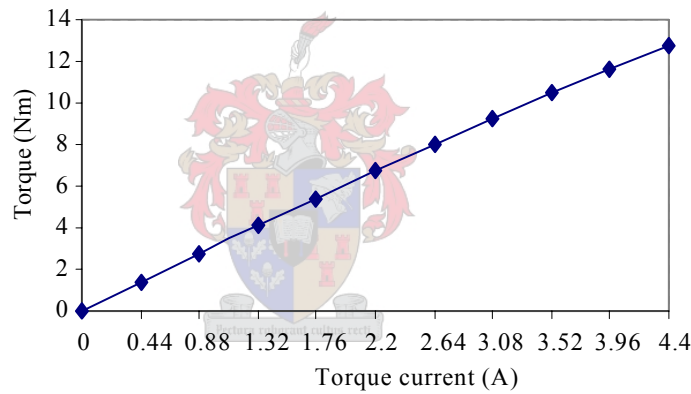
Fig. 4.15. FE calculated torque versus torque current.

4.5   Electromagnetic torque ripple evaluation

When investigating the electromagnetic torque ripple at the rated load condition, a very important known fact namely that the rotor field speed is the same as the rotating stator field speed must be kept in mind. In time-stepping FE analysis the electromagnetic torque ripple can be evaluated by keeping the seven specific rotor phase currents constant and setting the rotor speed equal to the stator field speed; this is at rated load and balanced MMF conditions, i.e. I_F = 3.5 A, I_T = 2.2 A and I_r = 5.6 A at a rated slip speed of 150 rpm. The result is shown in Fig. 4.16, with the torque ripple found to be less than 7.6% (0.5/6.5). The $12f_1$ ripple frequency in the torque is also evident; this is consistent with the ripple frequency in B in section 4.2.2. Further analysis of Fig. 4.16 shows that the torque ripple is caused by the stator phase current commutation.
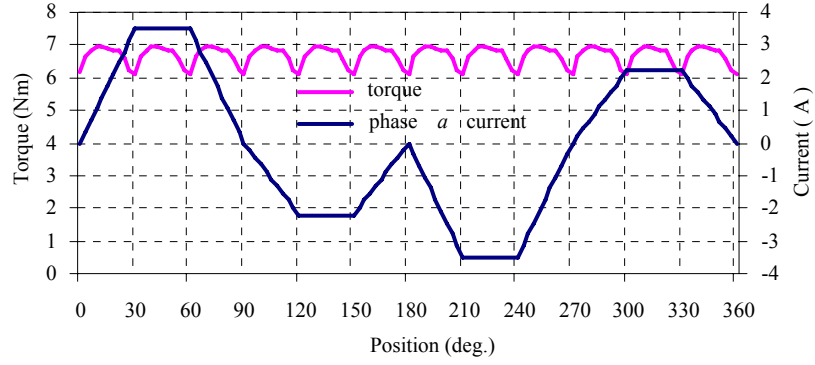
Fig. 4.16. Torque ripple at rated load condition.

4.6   Rotor induced voltage

To investigate the waveform of the induced voltage in a rotor phase winding of the six-phase IDCM the open-circuit voltage of the *j*-th rotor phase winding,

$$e_j = \frac{d\lambda_j}{dt},$$

(4.5)

is solved by time-stepping FE analysis. In eqn (4.5) λ_j is the flux linkage of rotor phase winding *j* calculated according to eqn (4.1) for the skewed machine. Three methods are used to determine the induced voltage in the rotor phase winding.

Method 1:

In this method the rotor is kept at standstill and the stator field is rotated by supplying the six-phase stator currents according to Fig. 4.5 with $I_F = 3.5$ A and $I_T = 0$ A. The flux linkages of rotor phase windings 7 and 14 obtained from FE calculation are shown in Fig. 4.17. To solve the induced voltage of (4.5) the forward difference approximation is used as

$$e_j = \frac{d\lambda_j}{dt} \approx \frac{\lambda_j(t_0 + \Delta t) - \lambda_j(t_0)}{\Delta t}$$

(4.6)
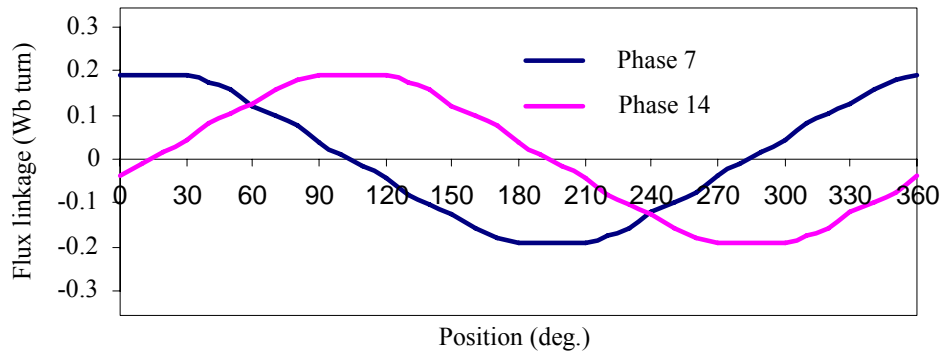
Fig. 4.17. Flux linkages of rotor phases 7 and 14.

Fig. 4.18 shows the FE calculated induced voltages of phases 7 and 14 at a stator field rotating speed of 150 rpm (rated slip speed). The quasi-square shape of the induced voltage waveforms is clear from this figure. Also the expected $12f_l$ high frequency component of the induced voltage is clear, as explained in the section 4.2.2.   The induced voltage waveform will be verified in Chapter 6 by practical measurements.

Method 2:

In this method the rotor is also kept at standstill. Due to the fact that the rotor phase windings are open circuit the mutual effect on the induced rotor voltage from the rotor side can be ignored. Therefore only the mutually induced rotor voltages from the stator side need to be considered. Hence, the rotor-induced voltage eqn (4.5) can be expanded by using the partial derivative as,

$$
\begin{aligned}
e_j &= \frac{\partial \lambda_j}{\partial i_a}\frac{di_a}{dt} + \frac{\partial \lambda_j}{\partial i_b}\frac{di_b}{dt} + \cdots + \frac{\partial \lambda_j}{\partial i_f}\frac{di_f}{dt} + \frac{\partial \lambda_j}{\partial \theta}\frac{d\theta}{dt} \\
&= L_{ja}\frac{di_a}{dt} + L_{jb}\frac{di_b}{dt} + \cdots + L_{jf}\frac{di_f}{dt} + \frac{\partial \lambda_j}{\partial \theta}\frac{d\theta}{dt}
\end{aligned}
\tag{4.7}
$$

As the rotor is at standstill, $\dfrac{\partial \lambda_j}{\partial \theta}\dfrac{d\theta}{dt} = 0$, and the mutual inductances can be calculated by,

$$
L_{jm} = \frac{\partial \lambda_j}{\partial i_m} \approx \frac{\lambda_j(i_m + \Delta i) - \lambda_j(i_m)}{\Delta i} \;,
\tag{4.8}
$$

where m = 1, 2, $\cdots$, 6. The rotor-induced voltage calculated from this method is shown in Fig. 4.19. For purpose of comparison, the induced voltage obtained from the first method, called the general derivative method, is also shown in Fig. 4.19. It is found that the two methods show good agreement in the voltage waveforms.
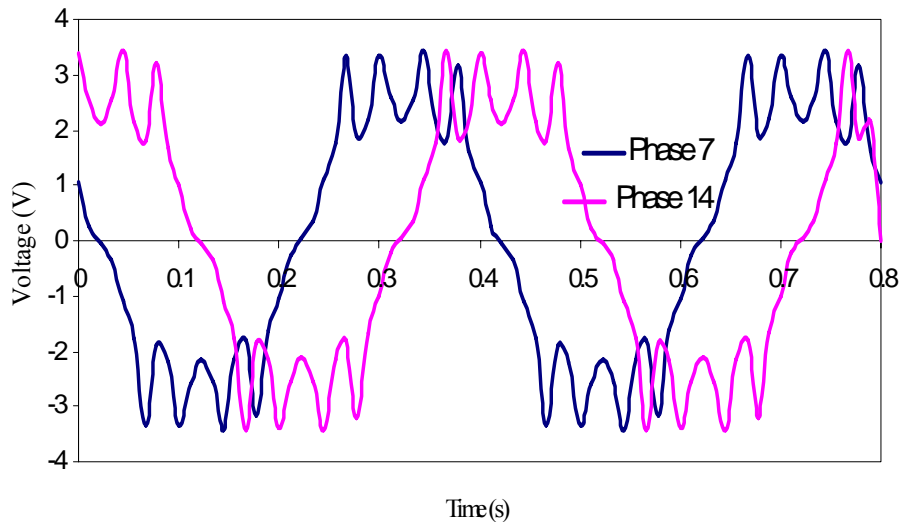
Fig. 4.18. FE calculated induced rotor voltages of phases 7 and 14 using method 1.
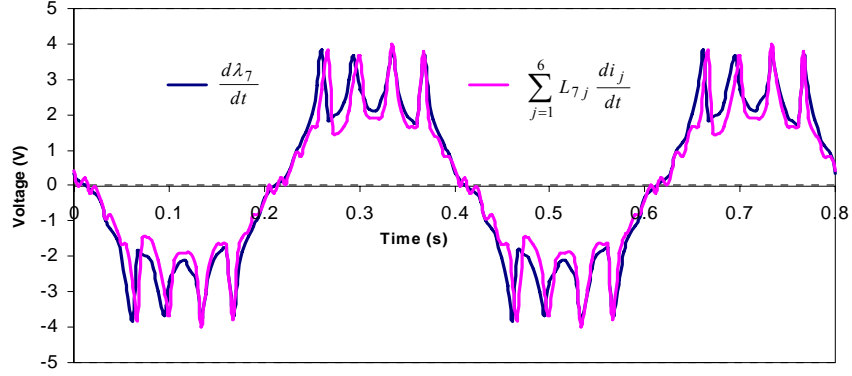
Fig. 4.19. Comparing methods 1 and 2 of the FE calculated induced rotor voltage of phase 7.

Method 3:

In this method the stator field is kept stationary and the rotor is rotated at a speed of 150 rpm. The stator phases are supplied with phase currents $i_a = -i_c = I_F/2$, $i_d = -I_F$; $i_b = i_e = i_f = 0$, which are the phase current values from Fig. 4.5 at time $t = t_1/2$. Due to the constant stator phase currents, eqn (4.5) is solved by

$$
\begin{aligned}
e_j &= \frac{\partial \lambda_j}{\partial i_a} \frac{di_a}{dt} + \frac{\partial \lambda_j}{\partial i_b} \frac{di_b}{dt} + \cdots + \frac{\partial \lambda_j}{\partial i_f} \frac{di_f}{dt} + \frac{\partial \lambda_j}{\partial \theta} \frac{d\theta}{dt} \\
&= \frac{\partial \lambda_j}{\partial \theta} \frac{d\theta}{dt} \approx \frac{\lambda_j(\theta + \Delta\theta) - \lambda_j(\theta)}{\Delta\theta} \omega_r
\end{aligned}
, \tag{4.9}
$$

again using the forward difference approximation. The results of the time-stepping FE calculated flux linkages and induced rotor voltages at a rotor speed of 150 rpm are shown in Fig. 4.20. Again the quasi-square shape waveform is evident, and, in this case, very similar to the induced stator phase voltage of brushless dc motors (BDCMs). With the stator field stationary there is, as expected, no high ripple induced voltage. The small ripple voltage visible in the waveform is due to slotting effects, which is, in this case, very much reduced by the skewed rotor.
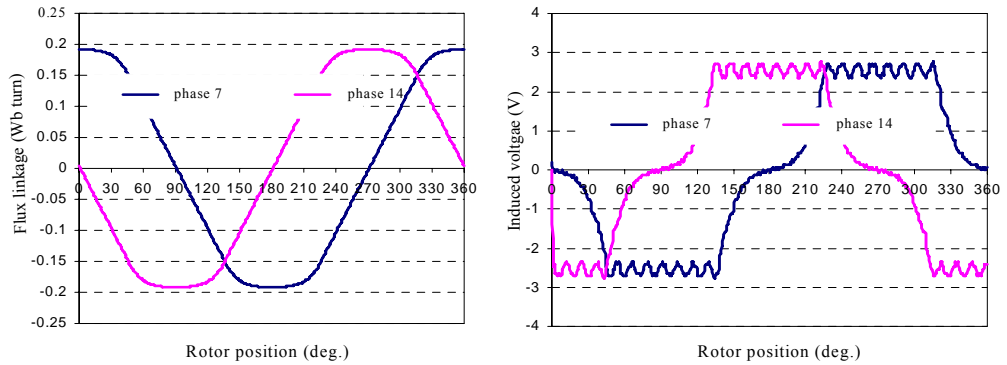
(a) Rotor phase flux linkages.   (b) Induced rotor voltage.

Fig. 4.20. FE calculated rotor induced voltage using method 3.

It is found among the three calculation methods that the average of the flat-topped rotor induced voltages are almost the same (around 2.5 V at rated load condition). There exist, however, differences among the induced voltage waveforms due to the different operating conditions. The induced rotor voltage according to the conditions of methods 1 and 3 will be verified in Chapter 6 by practical measurement.

4.7   Stator phase circuit modelling

In this section a stator per phase equivalent circuit of the six-phase IDCM is developed by considering the six-phase special stator current waveforms.

4.7.1   Effect of rotor currents on stator phase flux linkage

The effect of the active rotor phase currents on the stator phase flux linkage is investigated in order to prove that the stator per phase circuit modelling can be simplified and yet remain accurate. Fig. 4.21 shows current and flux linkage waveforms versus time with/without active rotor phase currents; this is at a synchronous speed of 950 rpm. In the first investigation the six-phase windings of the stator are supplied with only stator field current, i.e. $I_F = 3.5$ A and $I_T = 0$ A as shown in Fig. 4.5. In the second investigation, besides the field current, the stator torque current as well as the specific rotor phase currents are supplied to the machine at the rated load and balanced MMF condition, i.e. with $I_F = 3.5$ A, $I_T = 2.2$A and $I_r = 5.6$ A at rated slip speed of 150 rpm. The stator current and phase flux linkage waveforms for these two cases of investigation are shown in Fig. 4.21 (a) and (b) respectively. For the purpose of comparison, Fig. 4.21 (c) shows the stator phase flux linkage waveforms for both cases. It is clear that the phase flux linkage is hardly distorted by the addition of the stator torque and rotor phase currents at the balanced MMF condition.

From this it can be concluded that in the per phase circuit modelling it is reasonable to (i) ignore the effect of the rotor current under balanced MMF conditions and (ii) when mutual stator voltages need to be considered, the stator torque current can be ignored as the magnetic effect of the stator torque current is cancelled by the rotor phase currents at the balanced MMF condition. This way of modelling is an approximation, however it is accurate enough for simulation and control system design purposes. An in-depth study of the accurate per phase circuit modelling of the IDCM is beyond the scope of this thesis and must be further investigated.
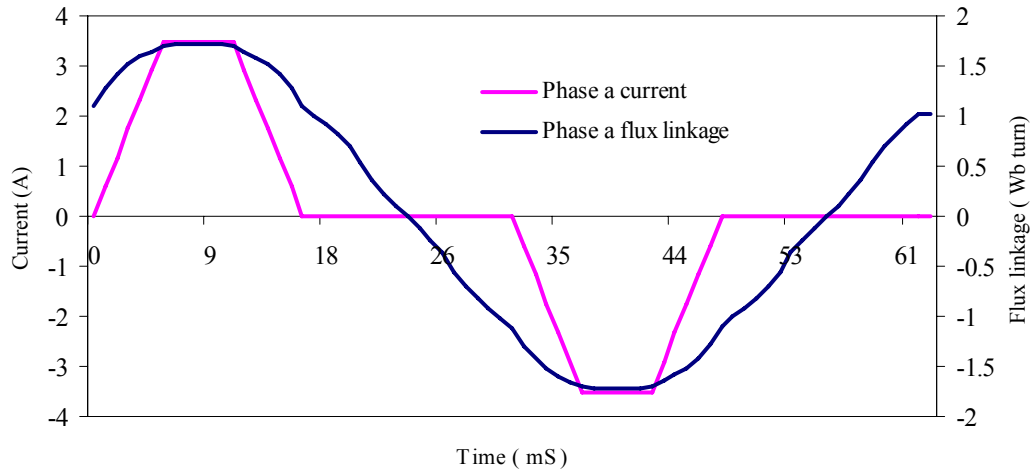
(a) FE calculated stator phase flux linkage with only stator field current.
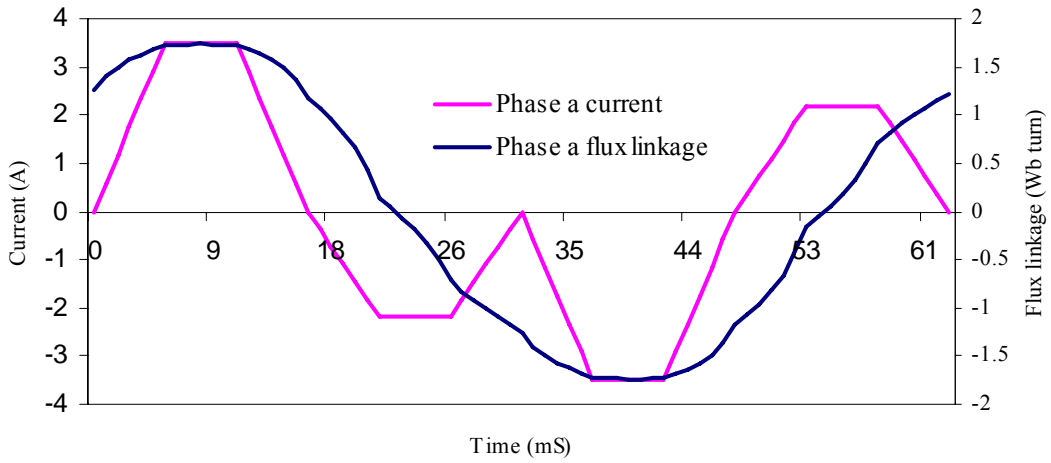
(b) FE calculated stator phase flux linkage with field, torque and rotor currents.
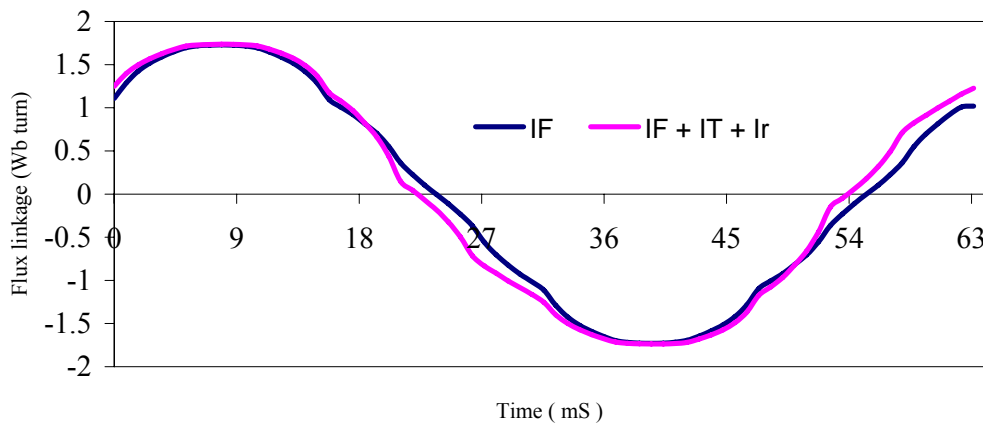
(c) Comparison of two case stator phase flux linkages.

Fig. 4.21. Stator phase flux linkage versus time under different current conditions.

4.7.2   Development of per phase equivalent circuit

The general stator voltage in the natural reference frame can be expressed as in eqn (4.10),

$$v_j = r_s i_j + \frac{d\lambda_j}{dt} \quad , \qquad (4.10)$$

where v_j , i_j and λ_j are the stator phase voltage, current and flux linkage of the jth phase respectively. The stator phase flux linkage of the six-phase IDCM is a non-linear function of the stator and rotor currents. By ignoring the stator torque current and the rotor phase currents as explained in section 4.7.1, the stator flux linkage can be expressed as

$$\lambda_s = F(\, i_s) \qquad (4.11)$$

where λ_s and i_s are column vectors

$$\lambda_s = \begin{bmatrix} \lambda_a \\ \lambda_b \\ \vdots \\ \lambda_f \end{bmatrix} \quad ; \qquad i_s = \begin{bmatrix} i_a \\ i_b \\ \vdots \\ i_f \end{bmatrix}_{I_T = 0} \qquad (4.12)$$

By using the partial derivative method the stator flux linkage, λ_s, can be expressed as,

$$\frac{d\lambda_s}{dt} = \begin{bmatrix} \frac{d\lambda_a}{dt} \\ \frac{d\lambda_b}{dt} \\ \vdots \\ \frac{d\lambda_f}{dt} \end{bmatrix} = \begin{bmatrix} \frac{\partial\lambda_a}{\partial i_a} & 0 & \cdots & 0 \\ 0 & \frac{\partial\lambda_b}{\partial i_b} & \cdots & 0 \\ \vdots & \vdots & \ddots & \vdots \\ 0 & 0 & \cdots & \frac{\partial\lambda_f}{\partial i_f} \end{bmatrix} + \begin{bmatrix} 0 & \frac{\partial\lambda_a}{\partial i_b} & \cdots & \frac{\partial\lambda_a}{\partial i_f} \\ \frac{\partial\lambda_b}{\partial i_a} & 0 & \cdots & \frac{\partial\lambda_b}{\partial i_f} \\ \vdots & \vdots & \ddots & \vdots \\ \frac{\partial\lambda_f}{\partial i_a} & \frac{\partial\lambda_f}{\partial i_b} & \cdots & 0 \end{bmatrix} \cdot \begin{bmatrix} \frac{di_a}{dt} \\ \frac{di_b}{dt} \\ \vdots \\ \frac{di_f}{dt} \end{bmatrix} + \begin{bmatrix} \frac{\partial\lambda_a}{\partial\theta} \\ \frac{\partial\lambda_b}{\partial\theta} \\ \vdots \\ \frac{\partial\lambda_m}{\partial\theta} \end{bmatrix} \cdot \frac{d\theta}{dt}$$

$$= [L]\cdot[\frac{di_s}{dt}] \; + \; [L_m]\cdot[\frac{di_s}{dt}] \; + \; [k_r]\cdot\omega_r \qquad (4.13)$$

$$= [v_L] \; + \; [e_m] \; + \; [e_r] \quad ,$$

where

$$[L] = \begin{bmatrix} \frac{\partial\lambda_a}{\partial i_a} & 0 & \cdots & 0 \\ 0 & \frac{\partial\lambda_b}{\partial i_b} & \cdots & 0 \\ \vdots & \vdots & \ddots & \vdots \\ 0 & 0 & \cdots & \frac{\partial\lambda_f}{\partial i_f} \end{bmatrix} = \begin{bmatrix} L_a & 0 & \cdots & 0 \\ 0 & L_b & \cdots & 0 \\ \vdots & \vdots & \ddots & \vdots \\ 0 & 0 & \cdots & L_f \end{bmatrix} \quad \text{is the self inductance matrix,}$$

$$[L_m] = \begin{bmatrix} 0 & \dfrac{\partial \lambda_a}{\partial i_b} & \cdots & \dfrac{\partial \lambda_a}{\partial i_f} \\ \dfrac{\partial \lambda_b}{\partial i_a} & 0 & \cdots & \dfrac{\partial \lambda_b}{\partial i_f} \\ \vdots & \vdots & \ddots & \vdots \\ \dfrac{\partial \lambda_f}{\partial i_a} & \dfrac{\partial \lambda_f}{\partial i_b} & \cdots & 0 \end{bmatrix} = \begin{bmatrix} 0 & L_{ab} & \cdots & L_{af} \\ L_{ba} & 0 & \cdots & L_{bf} \\ \vdots & \vdots & \ddots & \vdots \\ L_{fa} & \cdots & L_{fe} & 0 \end{bmatrix} \quad \text{is the mutual inductance matrix,}$$

and

$$[k_r] = \begin{bmatrix} \dfrac{\partial \lambda_a}{\partial \theta} \\ \dfrac{\partial \lambda_b}{\partial \theta} \\ \vdots \\ \dfrac{\partial \lambda_f}{\partial \theta} \end{bmatrix} = \begin{bmatrix} k_{ra} \\ k_{rb} \\ . \\ . \\ . \\ k_{rf} \end{bmatrix} \quad \text{is the slotted air gap EMF matrix.}$$

For example, for phase *a* the voltage equation can be written as,

$$
\begin{aligned}
v_a &= r_s\, i_a + L_a \frac{di_a}{dt} + (L_{ab}\frac{di_b}{dt} + L_{ac}\frac{di_c}{dt} + L_{ad}\frac{di_d}{dt} + L_{ae}\frac{di_e}{dt} + L_{af}\frac{di_f}{dt}) + k_{ra}\,\omega_r \\
&= r_s\, i_a + L_a \frac{di_a}{dt} + (v_{mab} + v_{mac} + v_{mad} + v_{mae} + v_{maf}) + k_{ra}\,\omega_r \\
&= r_s\, i_a + v_{La} + e_{ma} + e_{ra}\,.
\end{aligned}
\tag{4.14}
$$

The equivalent circuit of phase *a* is shown in Fig. 4.22. It is shown that the per phase voltage consists of a resistance voltage, self- and mutual inductance voltages and a rotor movement induced voltage due to the slotted air gap.
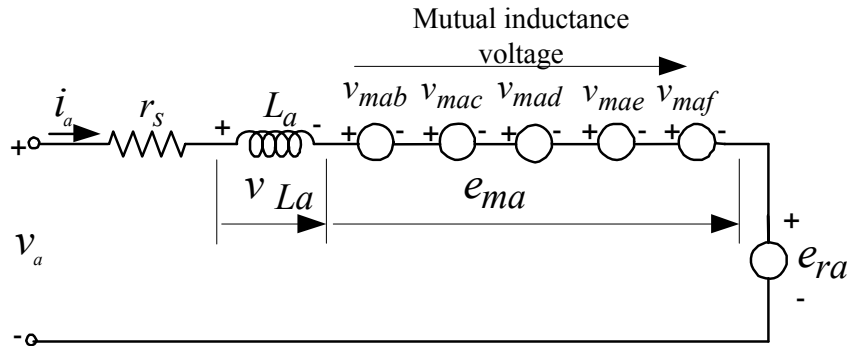
Fig. 4.22. Equivalent circuit of phase *a*.

4.8   Parameter determination

In this section the circuit parameters of eqn (4.14), namely the phase resistance, self-inductance, mutual inductance and slotted air gap constant, are determined through FE

analysis [the per phase resistance is calculated using an analytical formula in the FE program]. The per phase model parameters are verified later in this chapter by investigating the per phase induced voltage.

4.8.1   Inductance calculation

As shown in eqn (4.14), there are two types of inductances in the equation, namely self-inductance and mutual inductance. In the following sub-sections the calculation of these two types of inductances are described.

Self-inductance L_a :

According to the definition of self-inductance the forward difference approximation is used to determine the inductance as

$$L_j = \frac{\partial \lambda_j}{\partial i_j} \approx \frac{\lambda_j(i_j + \Delta i) - \lambda_j(i_j)}{\Delta i} \ , \tag{4.15}$$

where j refers to the jth stator phase. By adding a small change in current, Δi, to the phase current, i_j, while keeping the other phase currents constant, two different flux linkage data, $\lambda(i_j)$ and $\lambda(i_j + \Delta i)$, can be obtained from the FE analysis for the skewed machine. By using eqn (4.15), Fig. 4.23 shows the instantaneous self-inductance of phase *a* versus synchronous position. For the purpose of comparison, the current waveform of phase *a* is also shown in Fig. 4.23. It is clear that during field mode the instantaneous phase inductance is lower than during torque mode; this is due to saturation and the partial differentiation of the flux linkage versus current curves. This result is consistent with the instantaneous inductances of dc motors. Note that linearised inductance calculations give different results; then the field inductance is normally larger than the torque (armature) inductance. Finally, the instantaneous self-inductances of the other phases follow the same trend as that of phase *a*.

In the modeling for the purpose of simulation the average value of the instantaneous inductances during field and torque modes is taken. This is shown in Fig. 4.24. Mathematically, thus, the self inductance of the phase winding during field and during torque mode is calculated as

$$\bar{L}_f = \frac{1}{n_f} \sum_{i=1}^{n_f} L_{fi} \tag{4.16}$$

$$\overline{L}_t = \frac{1}{n_t}\sum_{i=1}^{n_t} L_{ti} \quad , \tag{4.17}$$

where n_f and n_t are the number of inductance-values for respectively the field and torque modes, and L_{fi} and L_{ti} are the ith instantaneous inductances of the field and torque modes.
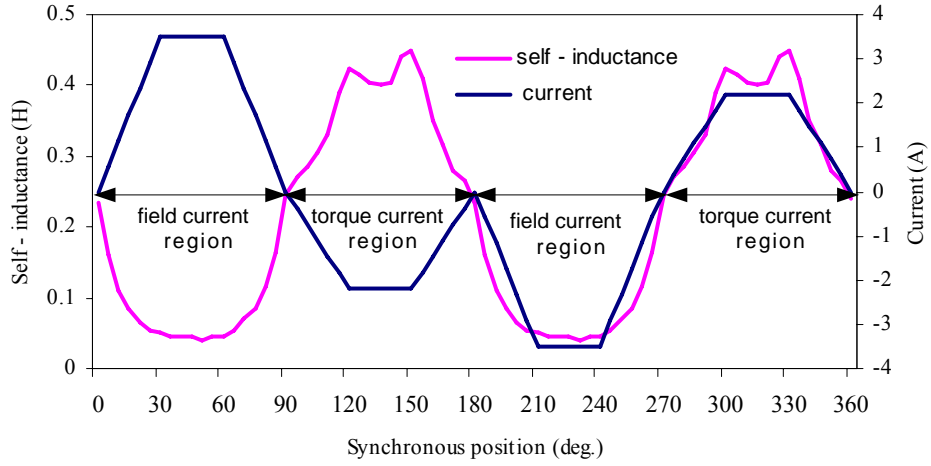
Fig. 4.23. FE calculated instantaneous self-inductance versus synchronous position.
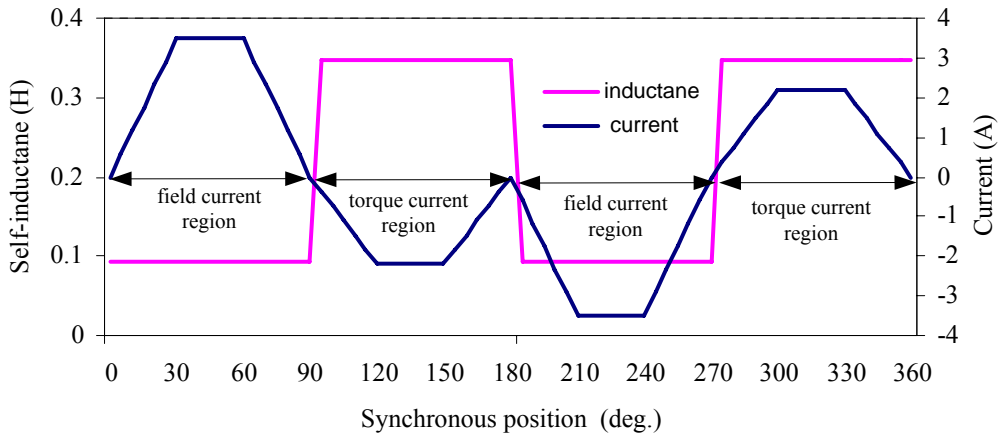
Fig. 4.24. Average self-inductance versus synchronous position.

Mutual inductance and mutual voltage:

The method to determine mutual inductances is the same as the method used for self-inductance; hence the mutual inductance is calculated by

$$L_{ji} = \frac{\partial \lambda_j}{\partial i_i} \approx \frac{\lambda_j(i_i + \Delta i) - \lambda_j(i_i)}{\Delta i} , \tag{4.18}$$

where i and j refer to the stator phases with $i \neq j$. Note that this calculation is executed by setting the torque current component of the i-phase equal to zero, as explained earlier.

Fig. 4.25 shows the results of the mutual inductances between phase a and the other five stator phases namely L_{ab}, L_{ac}, L_{ad}, L_{ae} and L_{af}. It can be seen that L_{ab} and L_{ad} have bigger absolute values when compared to the other mutual inductances; this is due to the fact that phases b and d are neighbourhood phases to phase a. In many respects the results of Fig. 4.25 are in agreement with the theoretical results of Table 3.3 [e.g. both calculations show that L_{af} (and its average) is zero and that L_{ac} and L_{ae} are the same]. One difference is that the values of the FE calculated mutual inductances are smaller than the theoretical calculated values of Table 3.3. The main reason for this deviation is that in the theoretical calculation the iron saturation has been neglected.
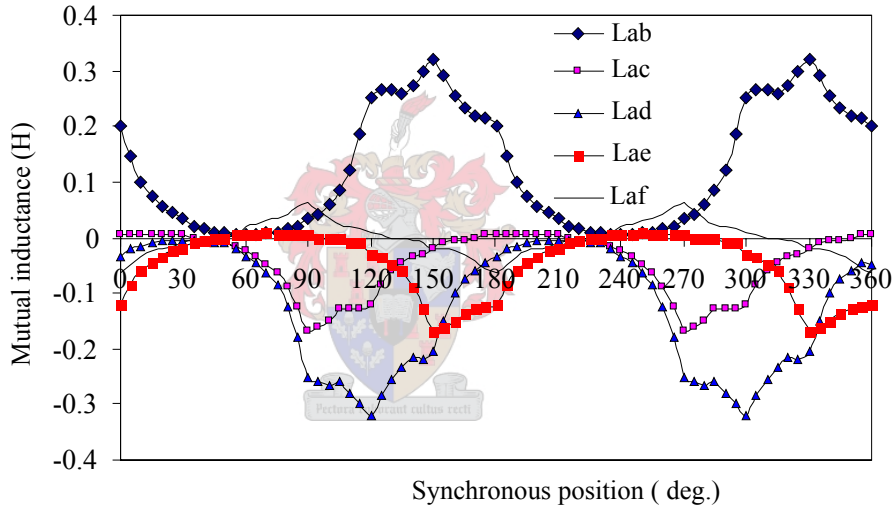
Fig. 4.25. FE calculated mutual inductances of phase a versus synchronous position.

The mutual voltage for a stator phase is determined by

$$e_{mj} = (\sum_{i=a}^{f} L_{mji} \frac{di_i}{d\theta}) \frac{d\theta}{dt} \quad [i \neq j],$$

$$= k_{ej} \omega_e$$

(4.19)

where

$$k_{ej} = (\sum_{i=a}^{f} L_{mji} \frac{di_i}{d\theta}) \quad [i \neq j];$$

(4.20)

k_{ej} is defined as the mutual voltage constant. The FE calculated mutual voltage e_{ma} of phase a is shown in Fig. 4.26 for the IDCM under consideration. In Fig. 4.26(a) it can be seen that the mutual voltage is practically zero during field mode, but high during torque mode. Fig. 4.26(b) shows the mutual voltage of the IDCM with stator torque current [and balanced rotor current]

added. Fig. 4.26(c) compares the results of Figs. 4.26(a) and (b). It shows that there is not much difference in the mutual voltage with or without torque current. This result confirms the validity of the earlier approximation made, that in the per phase modeling of the IDCM the torque current [and rotor current] can be ignored due to the flux linkage cancellation.
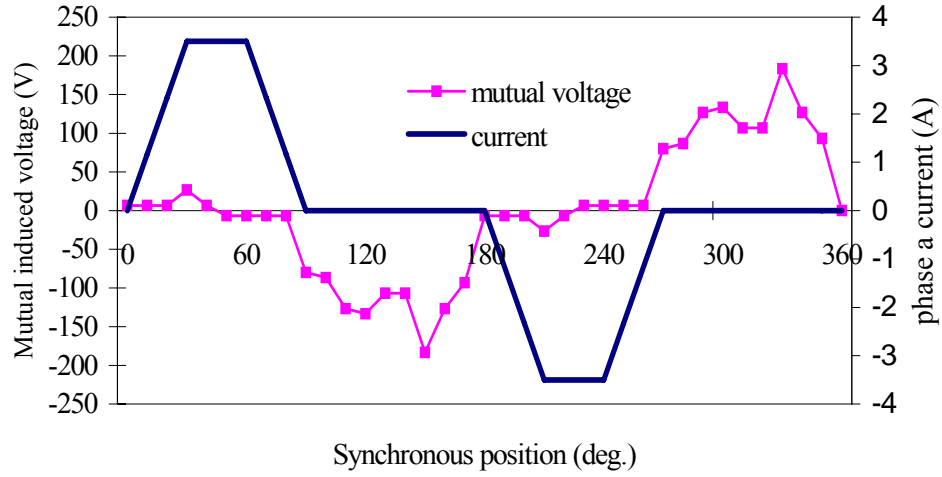
(a) Without stator torque current.
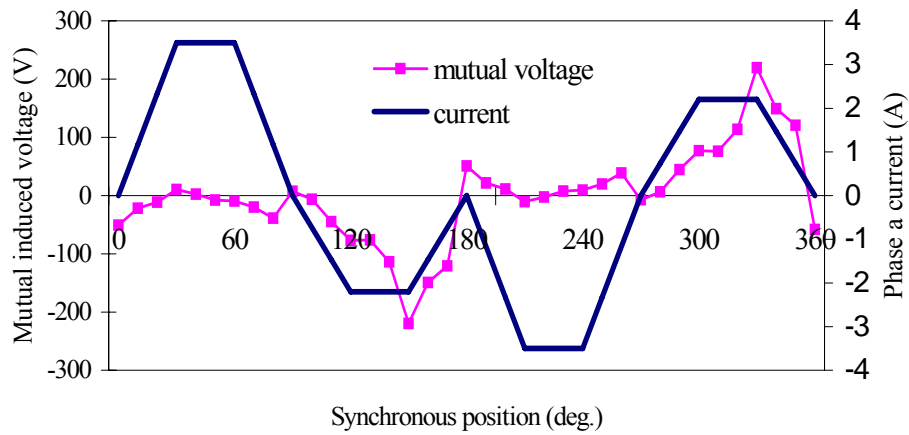
(b) With stator torque current.
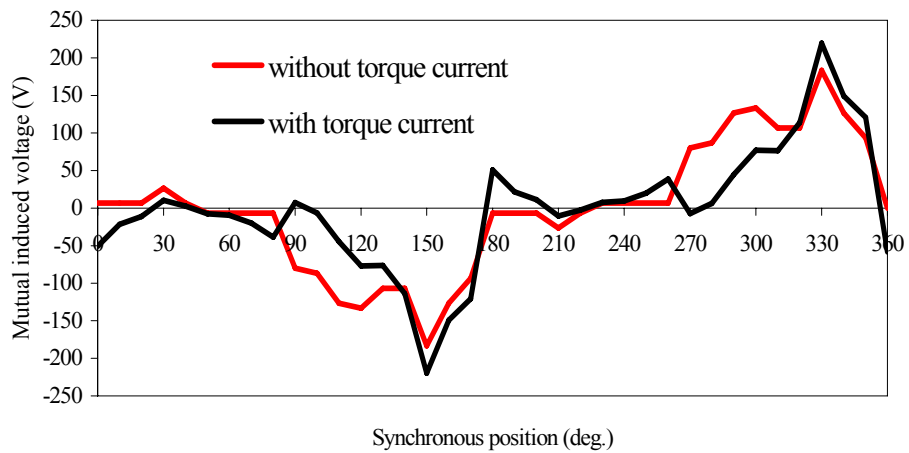
(c) Comparison of the mutual voltages.

Fig. 4.26. FE calculated mutual voltage e_{ma} of phase *a* at synchronous speed = 950 rpm.

In Fig. 4.27 the mutual voltage constant k_{ea} [eqn (4.20)] of the IDCM is shown. The average of k_{ea} during field and torque mode is also shown in Fig. 4.27(b); the average is used for the purpose of modelling and simulation. It can be seen that the average constant k_{ea} is again practically zero during field mode, but is much higher during torque mode [around 1.17 V/(rad/s)].

The results of Figs. 4.26 and 4.27 imply that with stator torque current flowing, netto (active) power flow takes place in a phase over a cycle; this is part of the developed power of the IDCM. The mutual voltage and the stator torque current are, thus, equivalent to, respectively, the back EMF and armature current of a dc motor.
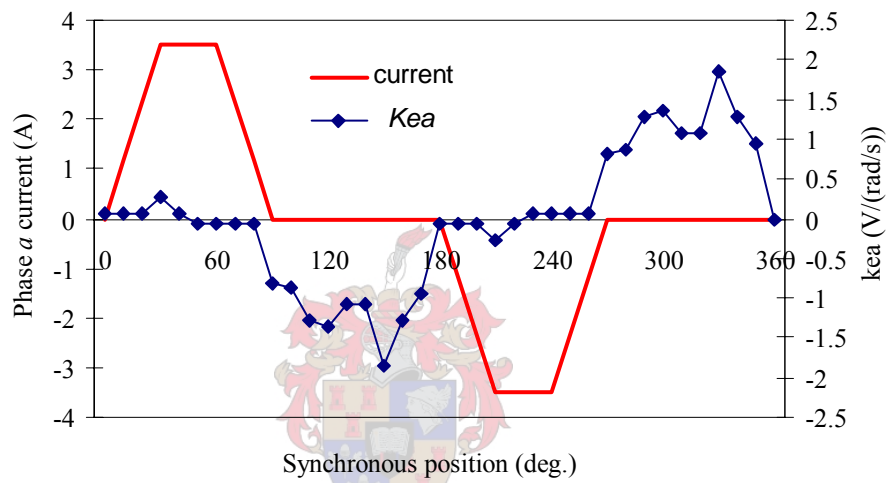
(a) Mutual voltage constant k_{ea} of phase *a* versus synchronous position.
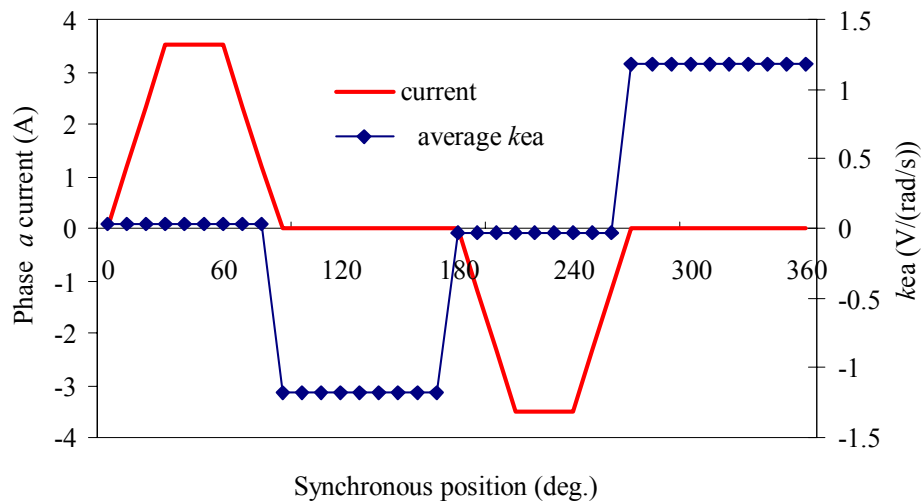
(b) Average mutual voltage constant of phase a versus synchronous position.

Fig. 4.27. FE calculated mutual voltage constant of phase *a* versus synchronous position.

4.8.2   Slotted air gap voltage constant.

The slotted air gap voltage constant k_{rj} [given in eqn (4.14)] is also investigated by using the forward difference approximation as

$$k_{rj} = \frac{\partial \lambda_j}{\partial \theta} \approx \frac{\lambda_j(\theta + \Delta\theta) - \lambda_j(\theta)}{\Delta\theta} \quad . \tag{4.21}$$

Fig. 4.28 shows k_{ra} (of phase *a*) versus rotor position of the skewed-rotor IDCM. Although it can be seen that the induced voltage e_{ra} is very small in this case [with $\omega_r = 83.7$rad/s (1000rpm) the maximum induced voltage will be $e_{ra(max)} = 0.14 \times 83.7 = 11.7$ V], this voltage might be substantially large for an unskewed rotor. However, it is clear that the average of the instantaneous power $e_{ra} i_a$ is zero, i.e. no netto (active) power is developed due to the slotted air gap which is correct. For the purpose of modelling and simulation the effect of the high frequency slotted air gap voltage is ignored, i.e. it is assumed that $e_{ra} = 0$.
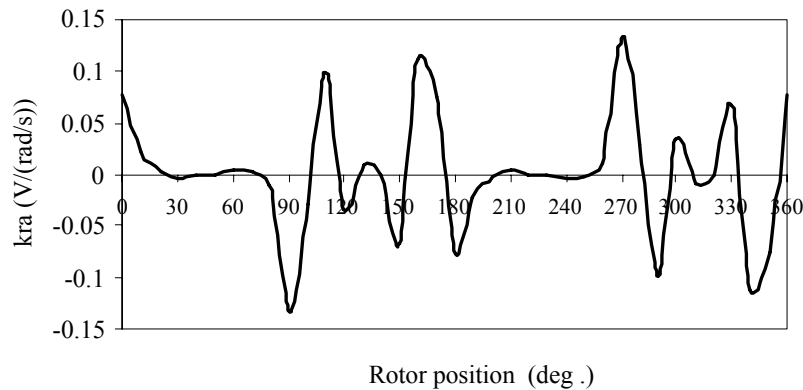
Fig. 4.28. FE calculated slotted air gap voltage constant versus rotor position.

Phase resistance:

The resistances of the stator and rotor phases are obtained using a standard analytical formula in the FE program; the phase resistances are calculated at a temperature of 75 °C. The values for the IDCM under consideration are: $r_s = 10.9$ Ω and $r_r = 0.64$ Ω; note the relatively high stator phase resistance.

By now all the parameters of phase *a* are determined; the parameter-values of the other phases are the same as that of phase *a*. From the above analysis, the per phase equivalent voltage equation can be simplified to that of eqn (4.22); the corresponding equivalent circuit is shown in Fig. 4.29.

$$v_j = r_s\, i_j + v_{Lj} + e_{mj}$$

$$= r_s\, i_j + L_j \frac{di_j}{dt} + k_{ej}\, \omega_s$$

(4.22)
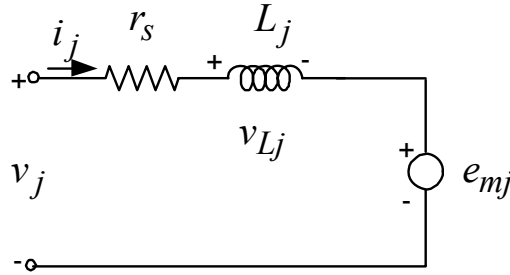
Fig. 4.29. Diagram of simplified per phase equivalent circuit.

4.9   Stator phase induced voltage investigation

The stator phase induced voltage is also investigated to further confirm the assumption that the resultant magnetic effect from the stator torque and rotor currents can be ignored under the balanced condition. The stator phase induced voltage is calculated by

$$e_j = \frac{d\lambda_j}{dt} \approx \frac{\lambda(\theta + \Delta\theta) - \lambda(\theta)}{\Delta\theta} \frac{d\theta}{dt}$$

$$= \frac{\lambda(\theta + \Delta\theta) - \lambda(\theta)}{\Delta\theta} \omega_s$$

.

(4.23)

The calculated results of the stator phase induced voltage with and without torque currents are shown in Fig. 30. It can be seen that there is little difference between the induced voltage waveforms; this thus confirms thus that the magnetic effects from the stator torque and active rotor currents can be ignored for the purpose of modelling and simulation.
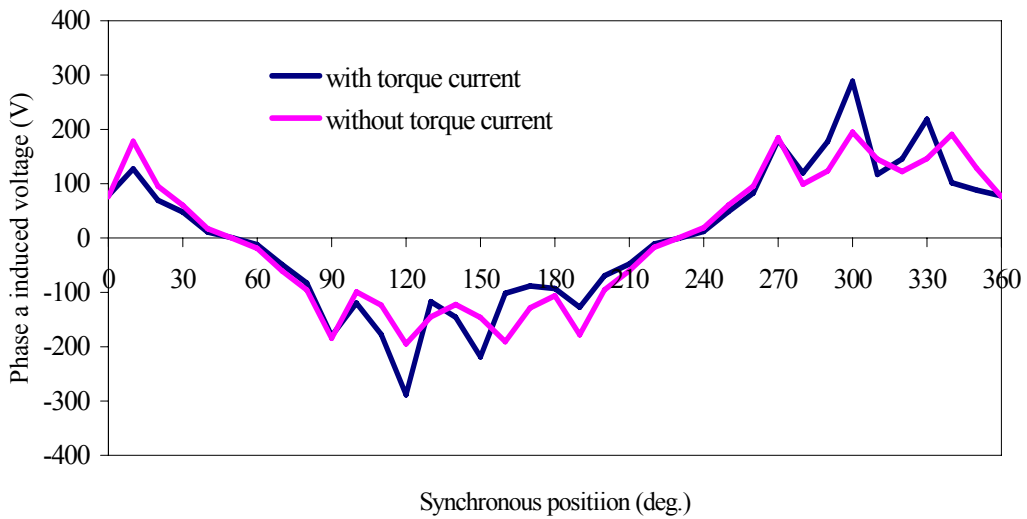
Fig. 4.30. FE calculated induced voltages of phase *a* at synchronous speed = 950 rpm with and without torque current.

4.10   Summary

In this chapter the per phase equivalent circuit and performance parameters of the six-phase
IDCM under consideration are calculated by using FE analysis. From the results obtained in
this chapter the following conclusions can be drawn:

- As a very important performance parameter relevant to the torque of the motor, the air
  gap flux density is investigated in terms of three aspects: (i) the flux density versus field
  current shows that with $B = 0.5$ T heavy saturation occurs in the core of the motor; this is
  due to the particular core dimensions of the 2-pole motor, (ii) the air gap flux density
  distribution is found to have a quasi-square waveform [like in a dc motor] and to rotate
  synchronously with the supply of the special current waveform; however, the negative
  side is that the flat-topped amplitude of the air gap flux density is not very constant, (iii)
  the air gap flux density is not affected much by supplying the stator torque and rotor
  currents under balanced conditions.

- The investigation into the torque of the IDCM shows that (i) the static torque versus stator
  torque current has a nearly linear relationship and (ii) that the torque ripple is due to the
  stator current commutation.

- The balanced condition of the flux linkages of the stator torque phase and active rotor
  phases is investigated by using the vector method. A very good agreement is obtained
  between FE and theoretical calculation methods.

- The analysed results of the mutual induced stator voltage imply that with stator torque
  current flowing, netto (active) power flow takes place in a phase over a cycle; this is part
  of the developed power of the IDCM. The mutual voltage and the stator torque current
  are, thus, equivalent to respectively the back EMF and armature current of a DC motor.

- The stator per phase induced voltage is evaluated by looking at the effect of the stator
  torque current of the motor. The results show that the effect is very little. This confirms
  that it is reasonable to ignore magnetic effects of the stator torque and active rotor
  currents for the purpose of modelling and simulation.

In summary, this chapter presents a detailed analysis of the six-phase IDCM. Some
conclusions will be further confirmed in Chapters 5 and 6.

5   MATLAB SIMULATION OF IDCM DRIVE SYSTEM

Chapters 3 and 4 focused on the analysis of the performance of the IDCM with the special stator phase current waveform.   What does the drive [motor plus inverter plus control] system's performance with this novel current control strategy look like? This chapter presents the simulation model and results of the six-phase IDCM drive system using Matlab/Simulink.

5.1   Development of simulation model for IDCM drive system

When a new control strategy of a converter or drive system is formulated, it is often convenient to study the system performance by simulation before building the prototype. The simulation not only validates the system's operation, but also permits optimization of the system's performance by iteration of its parameters. Simulink is basically a user-friendly, general digital simulation program of nonlinear dynamical systems, which works in the Matlab environment. A continuous or discrete time system can also be used. Although basically it is the Matlab (Math works) program, the user has a graphical interface where he or she builds the system with the help of sub-system blocks. In the beginning, the user must define the mathematical model of the system by differential and algebraic equations and express it in state variable or transfer function form. A library of templates or function blocks can be used in the simulation. Once the block diagram has been developed it can be simulated using any number of different solvers.
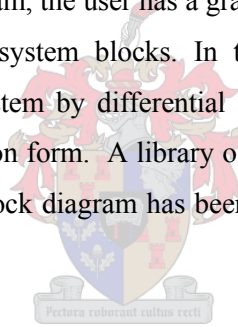
In the Matlab/Simulink workspace, the simulation model of the whole drive system is built as shown in Fig. 5.1. The simulation model consists of a PI speed controller, the synchronous position and speed calculation, the six-phase reference current waveform production, the hysteresis controller and inverter, the six-phase IDCM model and the mechanical system model.   This section introduces and explains the function of the different parts of the simulation model of Fig. 5.1.

5.1.1   PI Speed controller

The speed controller should guarantee that the rotor speed can follow a constant speed reference with zero steady state error. This is easily accomplished by choosing a PI controller. The function of the PI speed controller is to output a torque current command; its input, thus, is the speed error signal and its output is the amplitude of the stator torque current component. To design the PI speed controller, it is first necessary to consider the mechanical system of the six-phase IDCM drive. According to the motion equation [48] given by eqn(5.1),
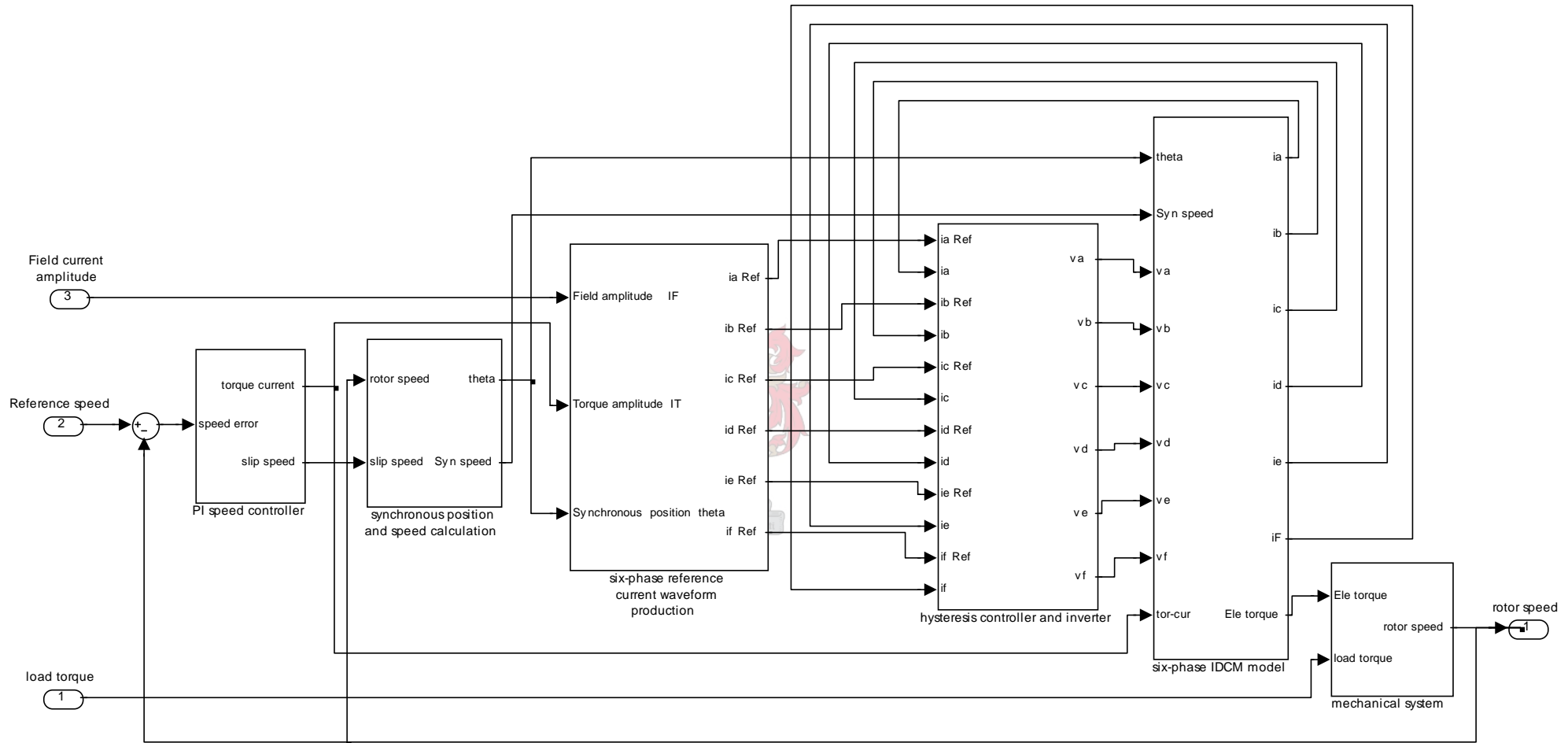
Fig. 5.1. Simulation block diagram in Matlab of six-phase IDCM drive system**.**

$$T_e = T_L + J \frac{d\omega_r}{dt} + \beta_{eq}\, \omega_r\,, \tag{5.1}$$

the Laplace transform and transfer function of eqn (5.1) are

$$T_e(s) = T_L(s) + J\ s\ \omega_r(s) + \beta_{eq}\, \omega_r(s) \tag{5.2}$$

$$G(s) = \frac{\omega_r(s)}{T_e - T_L} = \frac{1}{J\,s + \beta_{eq}}\ . \tag{5.3}$$

For the specific mechanical system of the machine test setup, as explained in Chapter 6, the values of J and β_{eq} are 0.7 Kg m^2 and 0.01 Nm / (rad/s) respectively as given in Appendix D.

According to the principle of the IDCM as discussed in Chapter 3 and 4, the produced electromagnetic torque can be expressed as

$$T_e = k_T\, I_T\,, \tag{5.4}$$

which means that there is a linear relationship between the stator torque current and the produced torque as shown in Fig. 4.15 from the FE analysis. The value of the torque coefficient, k_T, can be estimated as 2.91 from Fig. 4.15 (12.8 Nm/4.4 A). Using eqns (5.1) and (5.4), the simulation block diagram for the speed loop can be represented as shown in Fig.5.2.

In this thesis, the focus is on the current control strategy of the IDCM drive. The PI speed controller, thus, is designed for a relatively long settling time of about 1.5 s, as the settling time of the speed loop is not crucial for the current control investigation. By ignoring the torque current limit as shown in Fig. 5.2, the continuous plant transfer function is created in the Matlab command window as

$$G'(s) = \frac{k_T}{Js + \beta_{eq}} = \frac{2.91}{0.7s + 0.01}\ . \tag{5.5}$$

Then, by importing the plant into the Matlab's root tool, the speed controller is designed to give a settling time of $\tau_s = 1.6$ s to a step input command. The root locus plot and the step response of the system are shown in Fig. 5.3. From Fig. 5.3(a) the transfer function of the PI speed controller is obtained as

$$D(s) = \frac{1.0861(s+2)}{s} \approx 1 + \frac{2}{s}\ . \tag{5.6}$$
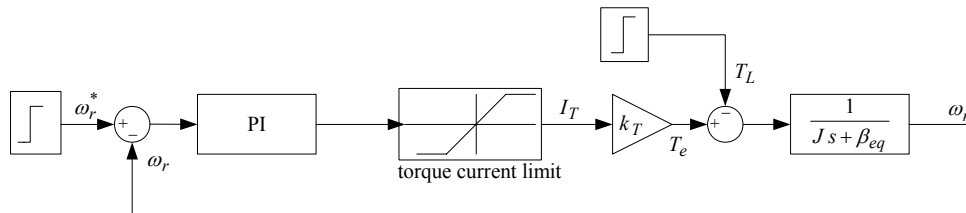
Fig. 5.2. Speed loop block diagram with PI controller.

The designed PI controller, therefore, has a proportional constant of $K_p = 1$ and a integral constant of $K_i = 2$. The speed response of the system with the designed PI controller is evaluated with the simulation block diagram in Matlab of Fig. 5.4. In this evaluation, a rotor speed command of $\omega_r^* = 500$ rpm (52.3 rad/s) is given; the simulated rotor speed, torque current and torque are tested with the results shown in Fig. 5.5. These results will be validated in Chapter 6.
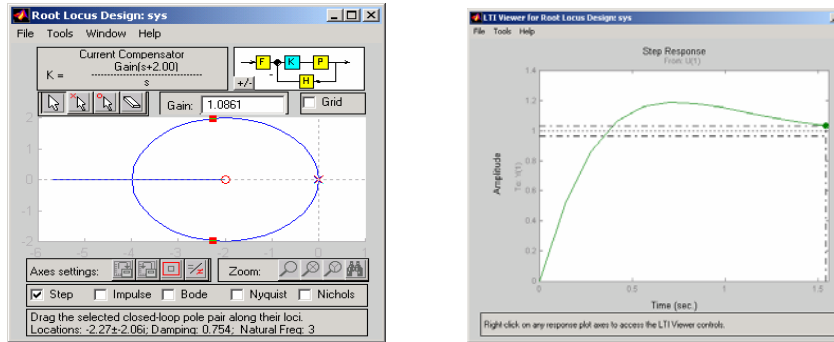
(a) Root locus.   (b) Step response.

Fig. 5.3. Speed response with specific PI controller.
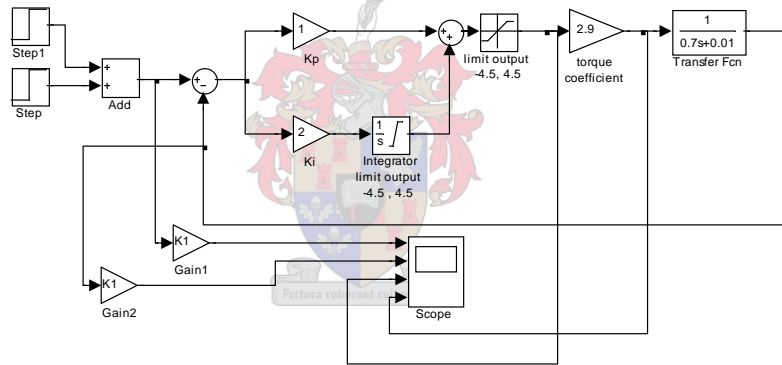
Fig. 5.4. Simulation block diagram in Matlab of the PI speed loop.
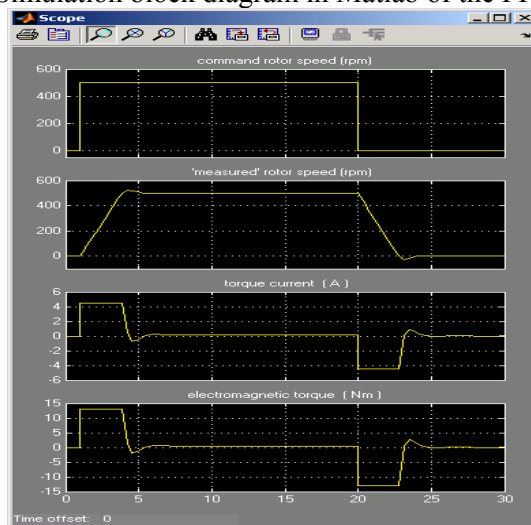
Fig. 5.5. Simulated results of the speed loop with the limits of the integrator and torque current [from top to bottom: command rotor speed; rotor speed response; torque current response and torque response respectively].

74

The complete block diagram of the PI speed controller block in Fig. 5.1 is shown in Fig. 5.6. This diagram includes the slip speed command using the slip speed constant, *k*, explained in section 3.5. The value of *k* for the IDCM drive is: *k* = 7.08 (rad/s)/A.
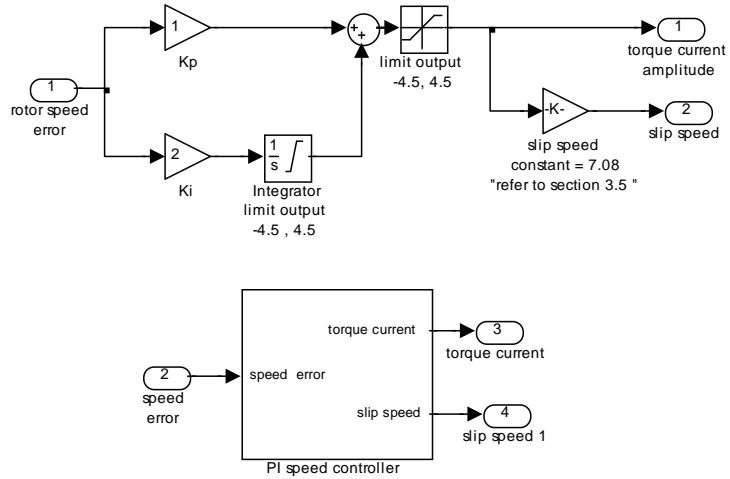
Fig. 5.6. Simulation block diagram of the PI speed controller.

5.1.2   *Synchronous position and speed calculation block*

The simulation block diagram for the synchronous position and speed is shown in Fig. 5.7. The synchronous position and speed is calculated by

$$\omega = \omega_r + \omega_{sl} \tag{5.7}$$

$$\theta = \int \omega \, dt \; . \tag{5.8}$$
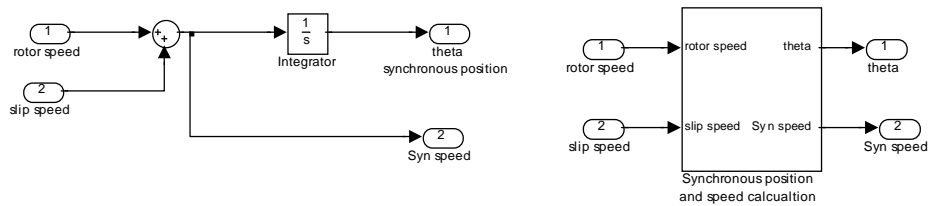
Fig. 5.7. Simulation block diagram for synchronous position and speed calculation.

5.1.3   *Six-phase current waveform generator block*

The simulation block diagram of the six-phase stator current waveform generator is shown in Fig. 5.8. The reference current waveforms are produced by the combination of the field and torque current look up tables. Note that in Fig. 5.8 the f(u) block is to convert the position signal to a saw-tooth waveform with a period of 2π.
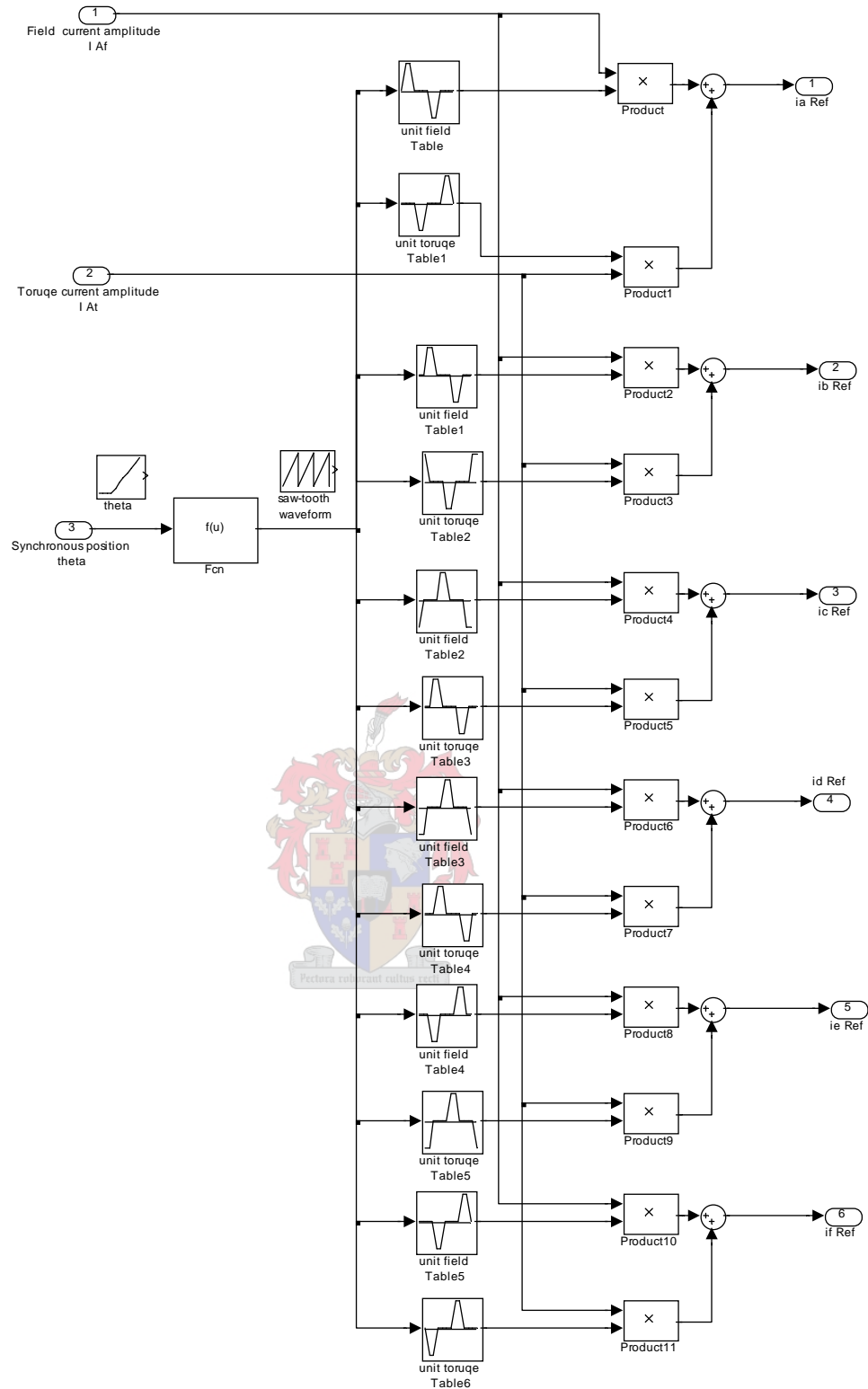
Fig. 5.8. Simulation block diagram of six-phase current waveform generator.

5.1.4   *Hysteresis controller and inverter*

The performance of the current loop is one of the most critical aspects of an ac drive in terms of its dynamic response and accuracy. Numerous current control techniques have been

developed which may generally be classified as linear PI, predictive and hysteresis current control.   Linear PI current control is simple to implement, but results in inherent tracking errors, both in amplitude and phase.   Moreover, it provides relatively poor transient response, whilst the controller tuning is sensitive to the drive system parameters.   In predictive current controllers, the current error is predicted at the beginning of each sampling period on the basis of the actual current and the motor parameters.   The required inverter voltage for the next modulation period is then calculated to minimize the predicted current error.   However, although good steady state and transient performance can be achieved, generally accurate knowledge of the system parameters is required.   The conventional hysteresis control results in an excellent transient response and is insensitive to load variation and relatively simple to implement.   Therefore, hysteresis current control is chosen in this study. Note, however, that hysteresis control has the disadvantage that the PWM switching frequency is not constant.

The hysteresis controller and inverter block diagram used in the simulation for phase *a* is shown in Fig. 5.9.   The hysteresis controller's switch input point is: -0.2 - +0.2, and the switch output point is: -300 - +300; this means that the bandwidth of the hysteresis controller is 0.2 A and the inverter DC bus voltage is 300 V.   Note that a full bridge with bipolar PWM switching is used to realize the per phase current control.
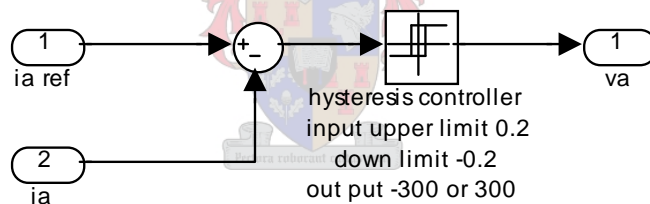
Fig. 5.9 Simulation block diagram of the hysteresis controller and inverter of phase *a*.

5.1.5   *Six-phase machine model*

The simulation block diagram of the six-phase machine, as shown in Fig. 5.10, consists of several sub-blocks, which are: sine function generator, six-phase machine current model and field and torque current adding models.   Their functions are described as follows:

- Sine function generator

The function of this block is to generate six sine waveforms which are out of phase with phase *a* with π/6, 4π/6, 5π/6, 8π/6, 9π/6 respectively.   These sine waveforms will be used in the six-phase machine circuit model to separate the phase current to field and torque current components.
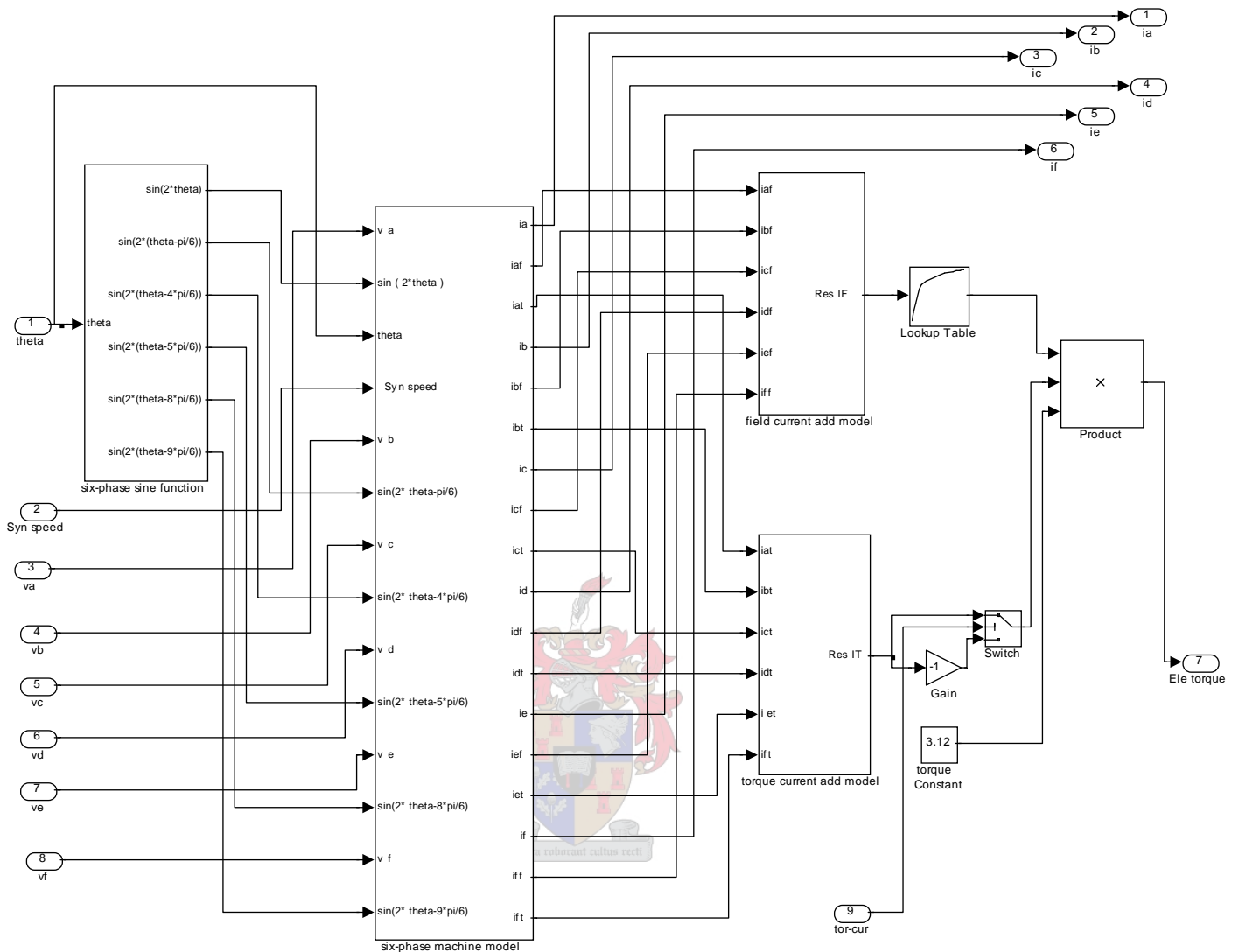
Fig. 5.10. Simulation block diagram of the six-phase IDCM model.

- Per phase modelling of the six-phase IDCM

The block diagram given in Fig. 5.11 represents the function given by eqn (4.22) in Chapter 4. It is assumed that the system is running under balanced MMF conditions. Under balanced MMF conditions the flux linkages of the active rotor phases and the stator torque phases cancel each other, as explained in Chapter 4. A simplified per phase equivalent circuit as shown in Fig. 4.29 can, thus, be used in the simulation. The average parameters explained and showed in section 4.8 are used in the stator per phase simulation block diagram.

The simulation block diagram of the mutual voltage, e_{ma}, is shown in Fig. 5.12. Note that the average mutual voltage constant is different during field and torque modes [Fig. 4.27]; this constant is defined by k_{eaf} and k_{eat} in Fig. 5.12 respectively for the field and torque modes. The signs of these constants are according to the phase current waveform as shown in Fig. 5.13.
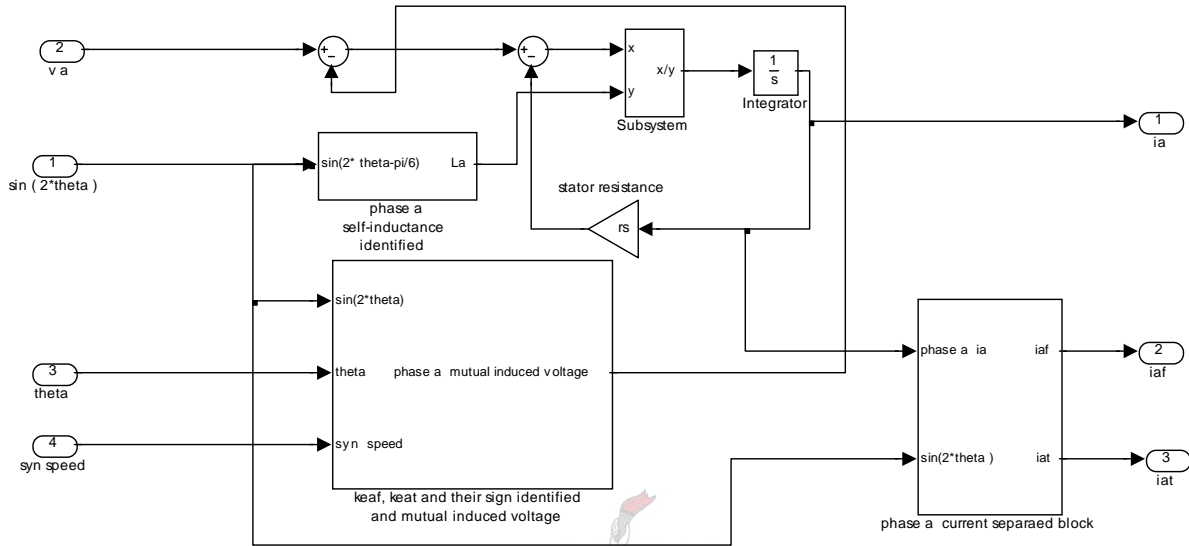
Fig. 5.11. Simulation block diagram in Matlab of the phase *a* equivalent circuit.
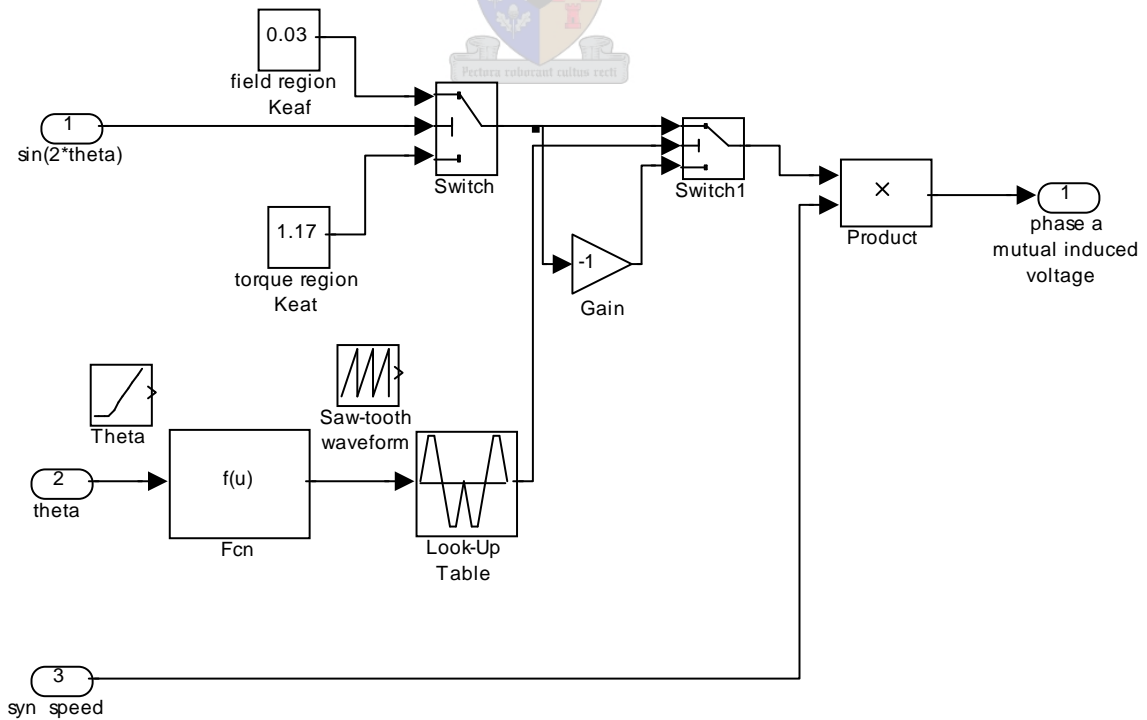
Fig. 5.12. Simulation block diagram in Matlab of the mutual voltage of phase *a*.
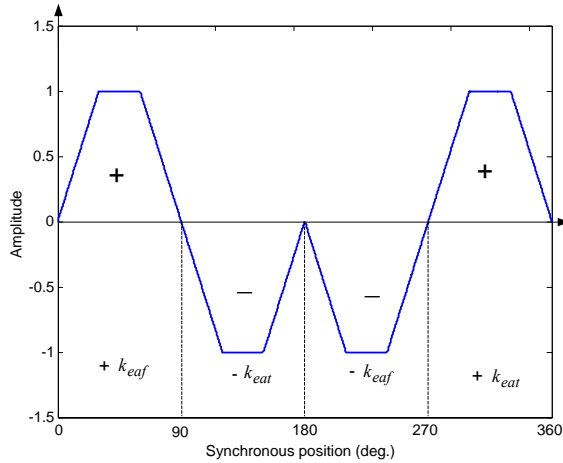
Fig. 5.13. Illustration of k_{eaf} and k_{eat} and their signs identified.

Note that the self-inductance L is also different during field and torque modes [Fig. 4.24]; this constant is defined as L_{af} and L_{at} in Fig. 5.14 for identifying the field inductance and torque inductance.

The phase current separation block diagram to generate separate field and torque machine currents is shown in Fig. 5.15. This simulation makes use of the sine and phase current waveforms shown in Fig. 5.16; note that the sine values are positive in the field region and negative in the torque region.
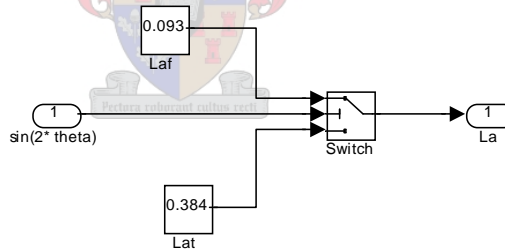
Fig. 5.14. Matlab simulation block diagram for the self inductance with L_{af} and L_{at} identified.
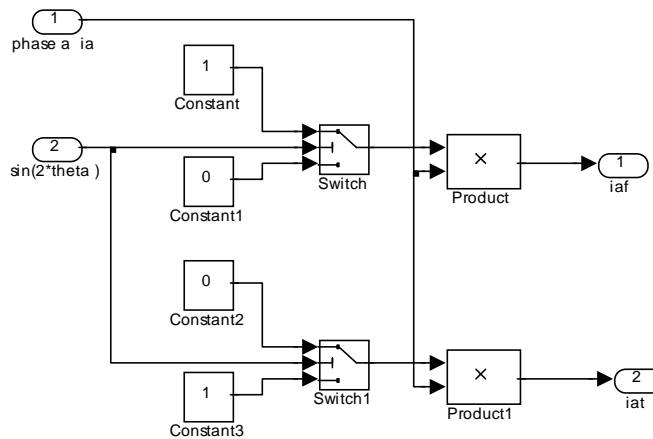
Fig. 5.15. Matlab simulation block diagram of field and torque current separation of phase *a*.
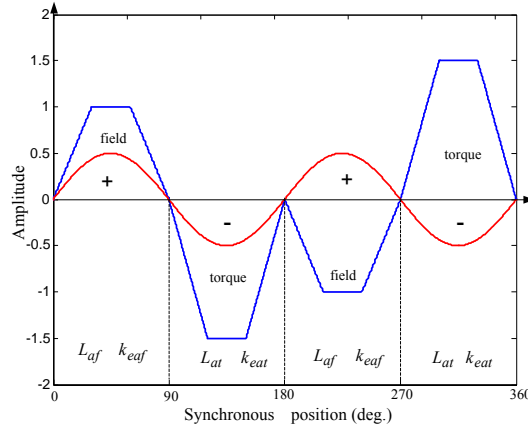
Fig. 5.16. Illustration of the separation of field and torque current using a sine waveform.

- Adding blocks for field and torque currents

The function of the field and torque current adding blocks shown in Fig. 5.10 is to add the absolute values of the six-phase field and torque currents. The resultant field and torque currents, *Res I_F* and *Res I_T* [see Fig. 5.10], are obtained as

$$Res \, I_F = \left| i_{af} \right| + \left| i_{bf} \right| + \left| i_{cf} \right| + \left| i_{df} \right| + \left| i_{ef} \right| + \left| i_{ff} \right| \tag{5.9}$$

$$Res \, I_T = \left| i_{at} \right| + \left| i_{bt} \right| + \left| i_{ct} \right| + \left| i_{dt} \right| + \left| i_{et} \right| + \left| i_{ft} \right| \tag{5.10}$$

- Electromagnetic torque calculation

In the last block of the machine simulation model of Fig. 5.10 the electromagnetic torque of the six-phase IDCM is calculated according to

$$T_e = 2 \times (7 \, N_r \, I_r) \, B \, l \, r \, . \tag{5.11}$$

As known, the relationship of $7 \, N_r \, I_r = 2 \, N_s \, I_T$ exists under the balanced MMF condition. Eqn (5.11), therefore, can be rewritten as

$$
\begin{aligned}
T_e &= 2 \times (2 N_s \, I_T) \, B \, l \, r \\
&= (2 \, I_T)(B)(2 \, N_s \, l \, r) \\
&= (2 \, I_T)(B)(2 \times 249 \times 128 \times 49 \times 10^{-6}) \\
&= (2 \, I_T)(B)(3.12)
\end{aligned}
\tag{5.12}
$$

The simulation block diagram of the electromagnetic torque product is shown in Fig. 5.17.
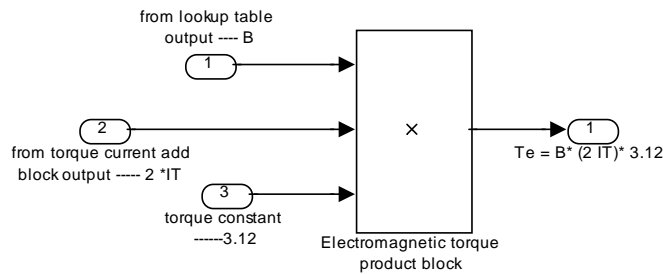
Fig. 5.17. Simulation block diagram in Matlab of the electromagnetic torque calculation.

5.1.6   Mechanical system

Finally, the simulation block diagram of the mechanical system in Fig. 5.1 is shown in Fig. 5.18, representing the function given in eqn (5.1).
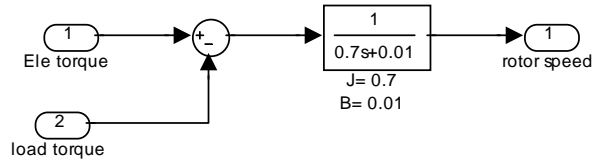
Fig. 5.18. Simulation block diagram in Matlab of the mechanical motion system.

5.2   Simulation results

In this section the six-phase IDCM drive's performance is simulated by using the drive system model of Fig. 5.1 in Matlab/Simulink.

5.2.1   Six-phase current waveforms

The special six-phase current waveforms form the foundation of the IDCM current control theory. It is important to verify, at first, that the current waveforms in the simulation are as proposed. The six-phase current waveforms are tested in the simulation and are shown in Fig. 5.19. It can be seen: (i) that the simulated motor stator phase currents follow the command currents and (ii) that the actual motor currents have a certain switching current band of 0.4 A due to hysteresis controller.
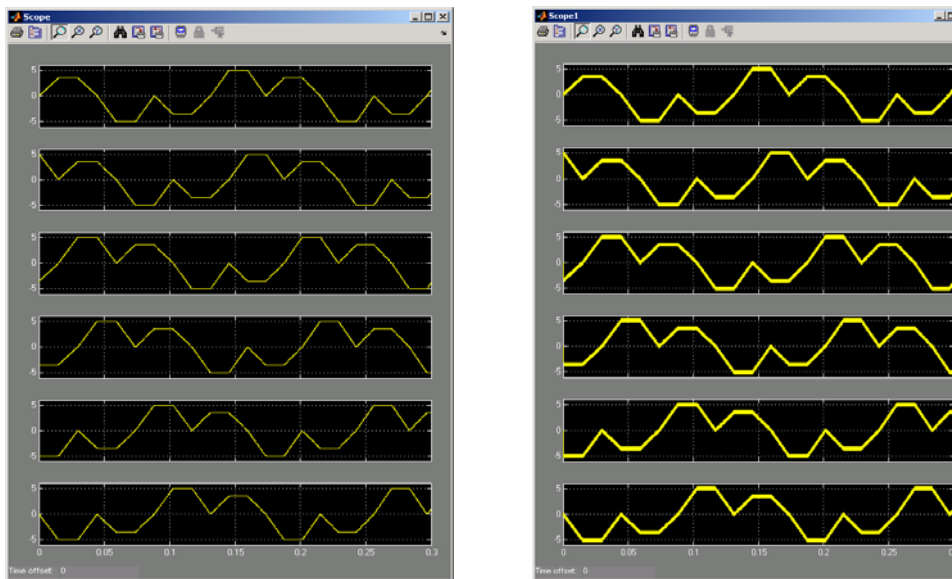
(a) Command current waveforms   (b) Motor current waveforms

Fig. 5.19. Six-phase current waveforms [from top to bottom: phases *a – f* respectively].

5.2.2   Static torque test

The static torque simulation test aims to investigate the electromagnetic torque performance of the IDCM at rotor standstill. To guarantee that the rotor is at standstill in the simulation, it is necessary to connect the load torque with the electromagnetic torque as shown in Fig. 5.20. The static torque is investigated by

- ramp up the torque current from 0 – 4.4 A by using a lookup table and
- ramp up the slip speed [also synchronous speed at standstill] from 0 – 300 rpm to reveal the slip speed versus torque current [Fig. 4.15], as shown in Fig. 5.20.

The static torque simulation results are shown in Fig. 5.21. It can be seen clearly that the phase current changes with frequency and torque current amplitude. The electromagnetic torque reveals a certain band due to the hysteresis controller. For clarity, Fig. 5.22 shows the simulated result of the electromagnetic torque versus torque current; this result is consistent with the result obtained in section 4.3.
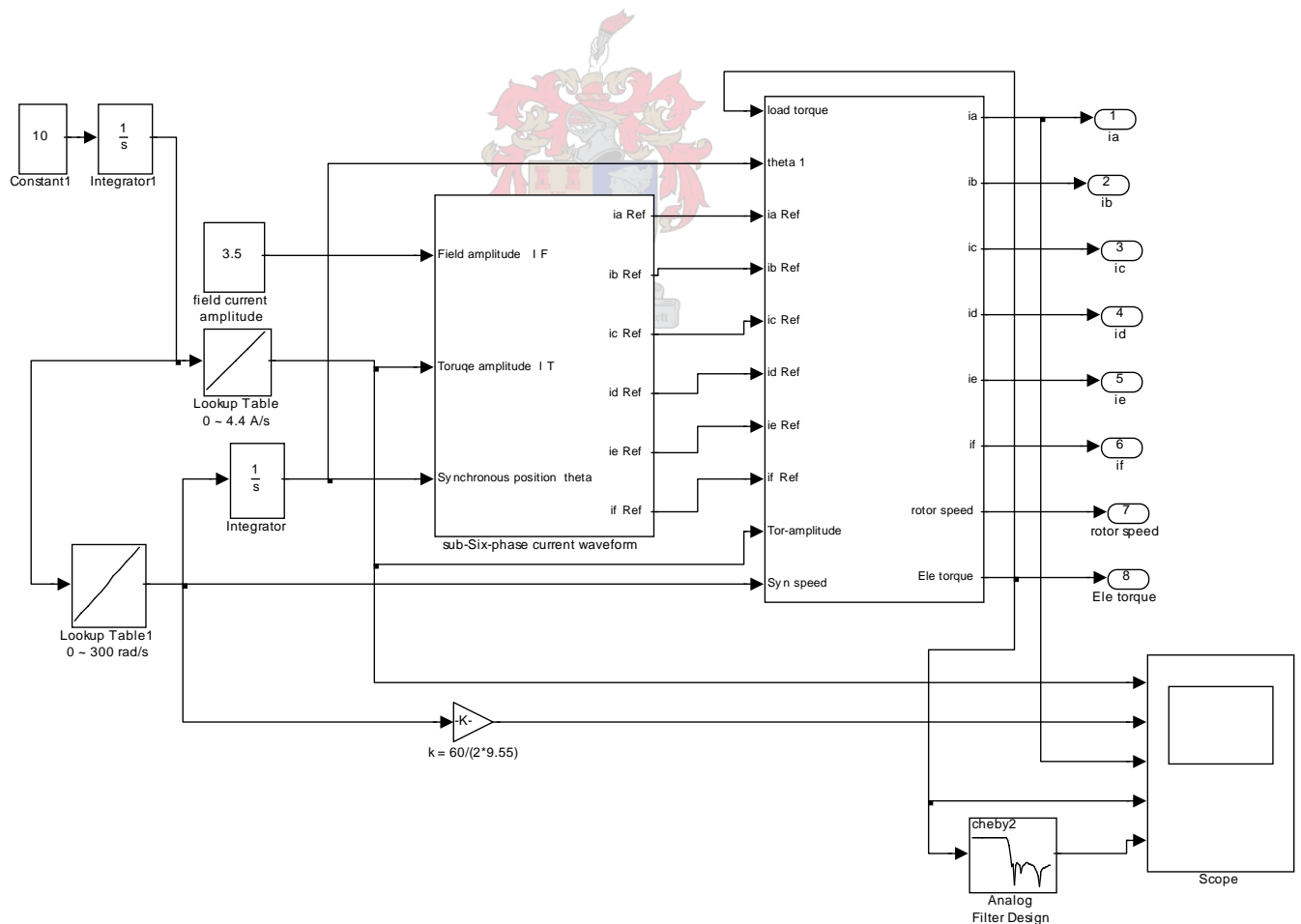
Fig. 5.20. Modified simulation block diagram for the static torque simulation test.
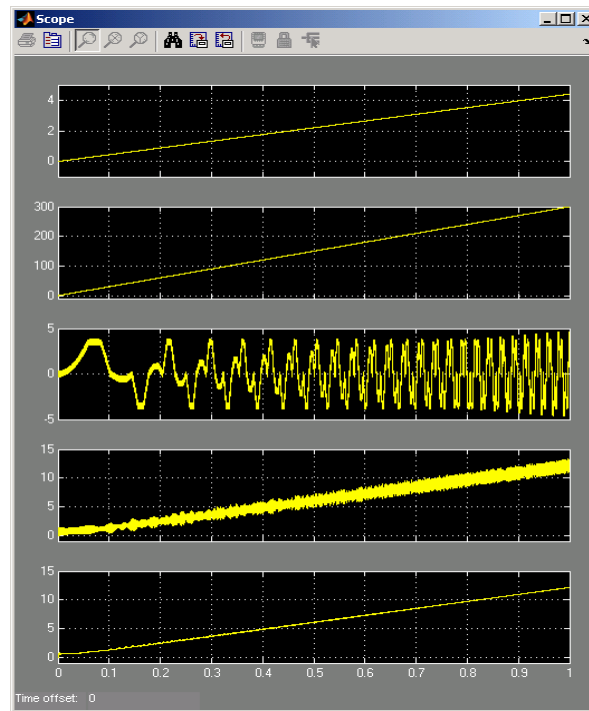
Fig. 5.21. Simulation results with rotor at standstill [from top to the bottom: torque current amplitude; slip speed or synchronous speed; phase *a* current waveform; electromagnetic torque without filter; electromagnetic torque with filter].
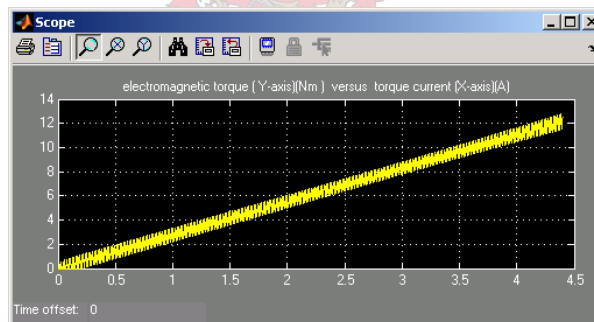
Fig. 5.22. Simulated result of electromagnetic torque versus torque current.

5.2.3   *Start up and steady state running performance test*

To investigate the start up performance of the IDCM drive a step speed command equal to 500 rpm is given in the simulation at time $t = 1$ s. During steady state at time $t = 10$ s and $t = 15$ s different amplitude step loads are supplied to the drive system. The results of this simulation are shown in Fig. 5.23. Note that Fig. 5.23 also shows the simulation results for a command speed of 800 rpm. From the results it is found that:

(i)   the start up time is around 4.5 s; this is consistent with the results given in Fig. 5.5;

(ii)   the torque current is limited at a value of 4.5A and furthermore the electromagnetic torque waveform follows the torque current waveform;

(iii)   the current waveform of phase *a* shows clearly that the frequency and torque current amplitude vary under transient conditions, but are constant in the steady state condition of the drive;

(iv)   there is only a slight overshoot in the rotor speed response.

5.2.4   *Torque response to step torque current command*

This simulated condition is almost similar to the static torque simulation test of section 5.2.2, except that a pulse torque current command is in this case applied to the system. The simulation results are shown in Fig. 5.24.

It can be seen that the electromagnetic torque has a very fast response to the torque current command, except for the torque ripple caused by the hysteresis controller. These results will be verified by practical results in Chapter 6.
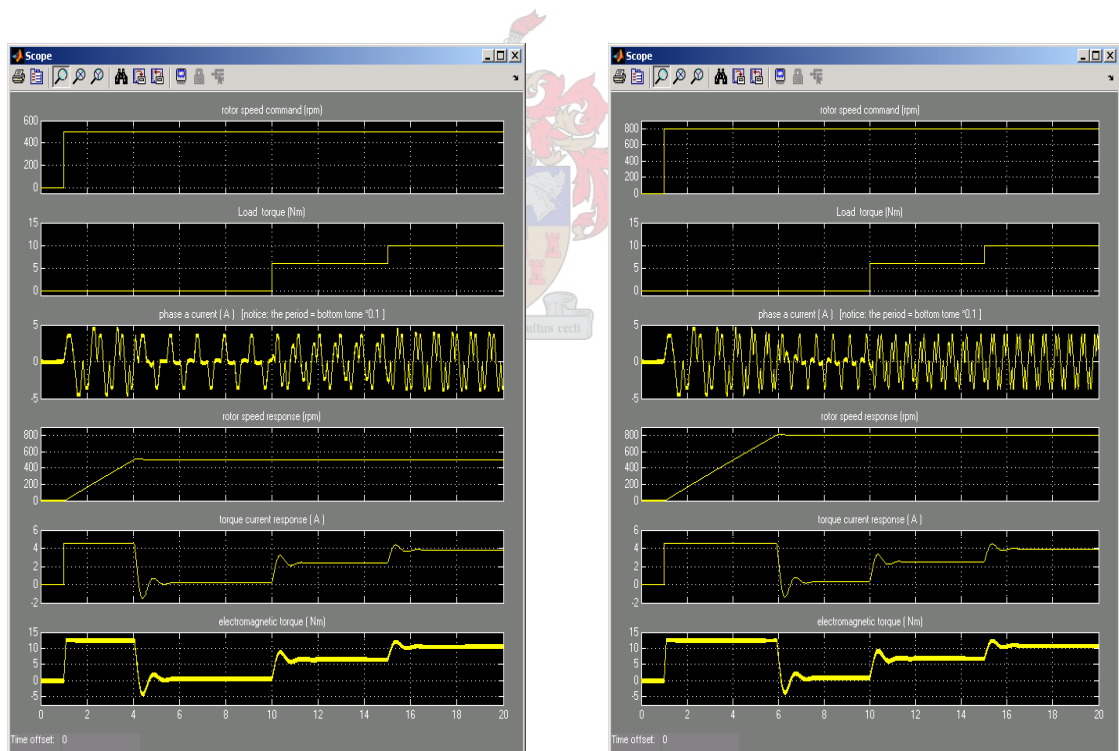
(a) speed command = 500 rpm   (b) speed command = 800 rpm

Fig. 5.23. Simulation results of speed and load torque commands.

[from top to bottom: rotor speed command; load torque; phase *a* current waveform; rotor speed response; torque current response; electromagnetic torque response].
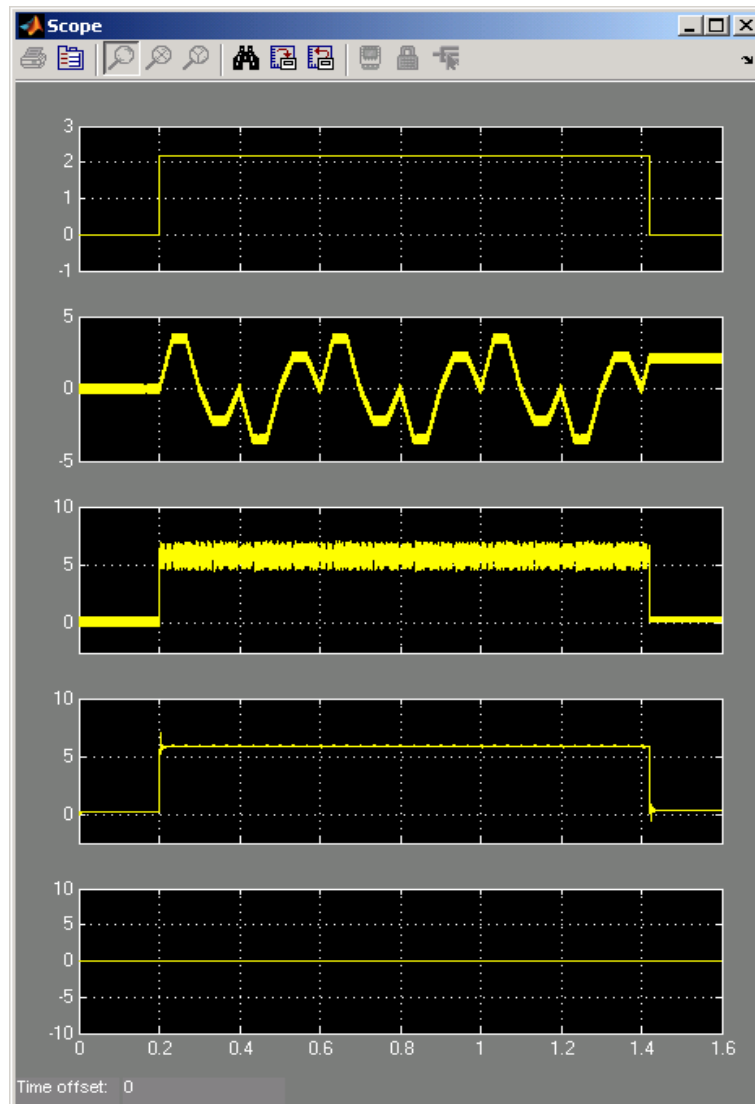
Fig. 5.24. Electromagnetic torque response to torque current command
[from top to bottom: the torque current command; phase *a* current waveform; electromagnetic torque without filter; electromagnetic torque with filter; rotor speed].

5.3   Conclusions

In this chapter the six-phase model of the IDCM drive system is built in the Matlab/Simulink software and the performance of the drive system is investigated under specific conditions. The simulation shows for the first time the operation of the complete six-phase IDCM drive system. The simulated results give background to the practical experiment that is explained in Chapter 6. It must be declared that all these simulated results are obtained under with the assumption that torque current MMF is balanced by rotor current MMF.

6   EXPERIMENTAL EVALUATION OF IDCM DRIVE

This chapter presents the experimental evaluation of the proposed IDCM drive system with a six-phase induction machine. The system is tested to validate the performance obtained from theoretical analysis and simulation results. Before the static and running torque tests of the IDCM are performed a number of basic tests are carried out. These are (i) the measurement of the air gap flux density versus field current; (ii) the performance measurement of the digital PI and hysteresis current controllers; (iii) the verification of the torque current polarity and (iv) the effect of the *k*-value [*k* is the slip speed versus torque current constant] on the control drive system. The rotor induced voltage is also tested with the rotor at standstill. Under running conditions the following are tested: (i) the performance of the PI speed controller, (ii) the start and stop performance of the drive and (iii) the rotor induced current.

6.1   Experimental setup

An experimental setup, as explained in Fig. 6.1, is built to test the proposed IDCM drive technique. This section describes the parts that compose the experimental setup. Firstly the machine test setup is introduced followed by a brief description of the six-phase power converter. Finally a brief description of the digital signal processor (DSP) controller is presented.
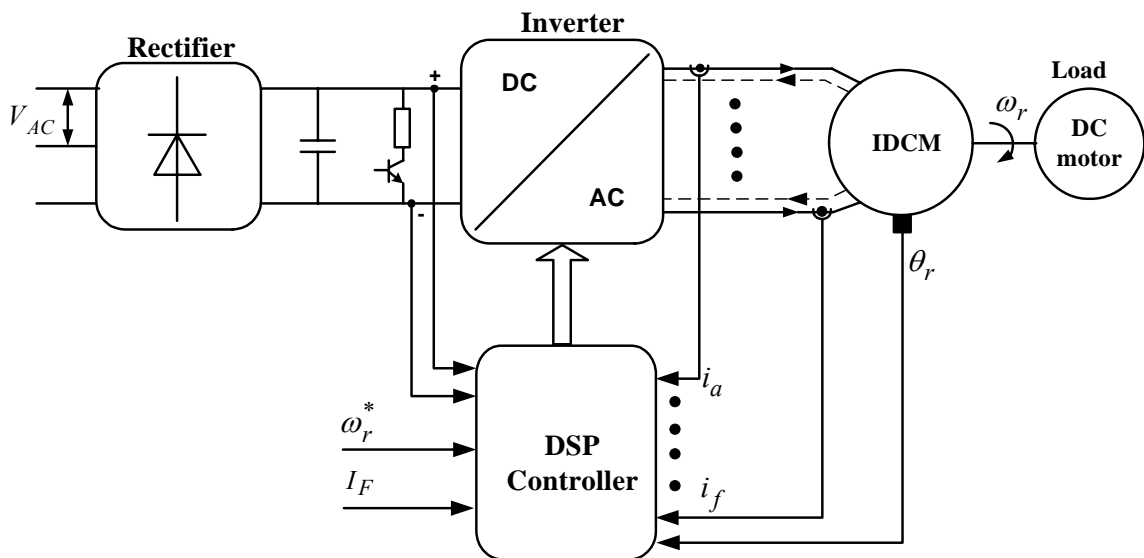
Fig. 6.1. Block diagram of six-phase IDCM drive system.

6.1.1   *Machine test setup*

The components of the machine test setup are shown in Fig. 6.2. This consists of the six-phase machine under test, which is a six-phase induction machine, a torque sensor, a resolver and a dc machine used as load or driving unit. The corresponding photos of the machine test setup and torque sensor are shown in Figs. D.1 – D.2 of Appendix D.1.
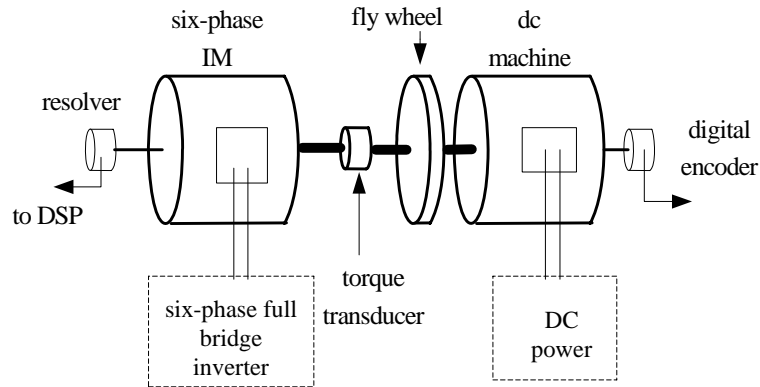
Fig. 6.2. Machine test setup.

6.1.2   *Power inverter*

Due to the fact that the special phase current waveforms as proposed in Chapter 3 are not balanced, which means that the sum of the six-phase currents is not zero, a six-phase full bridge inverter is necessary. The power circuit diagram of the inverter is shown in Fig. 6.3. For the inverter and corresponding photos refer to Appendix D.2.
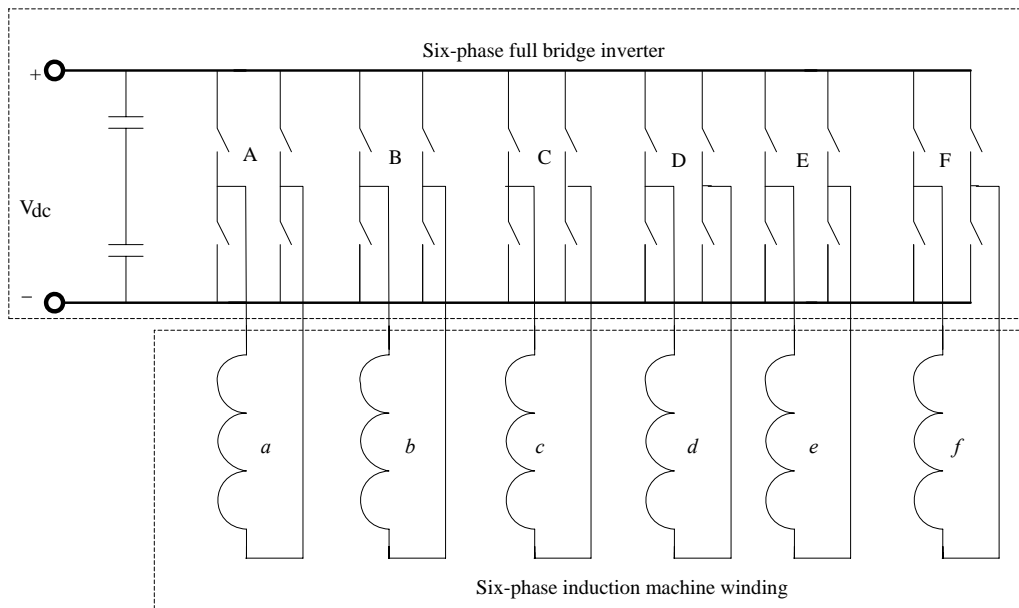
Fig. 6.3. Six-phase power inverter circuit.

6.1.3   DSP controller

The control of the IDCM drive is implemented by using a DSP controller [63 – 65]. The block diagram of the DSP controller used in this study is shown in Fig. 6.4. A brief description of the main parts of the DSP controller is given in Appendix D.3; the control software block diagrams are also explained in Appendix D.4.
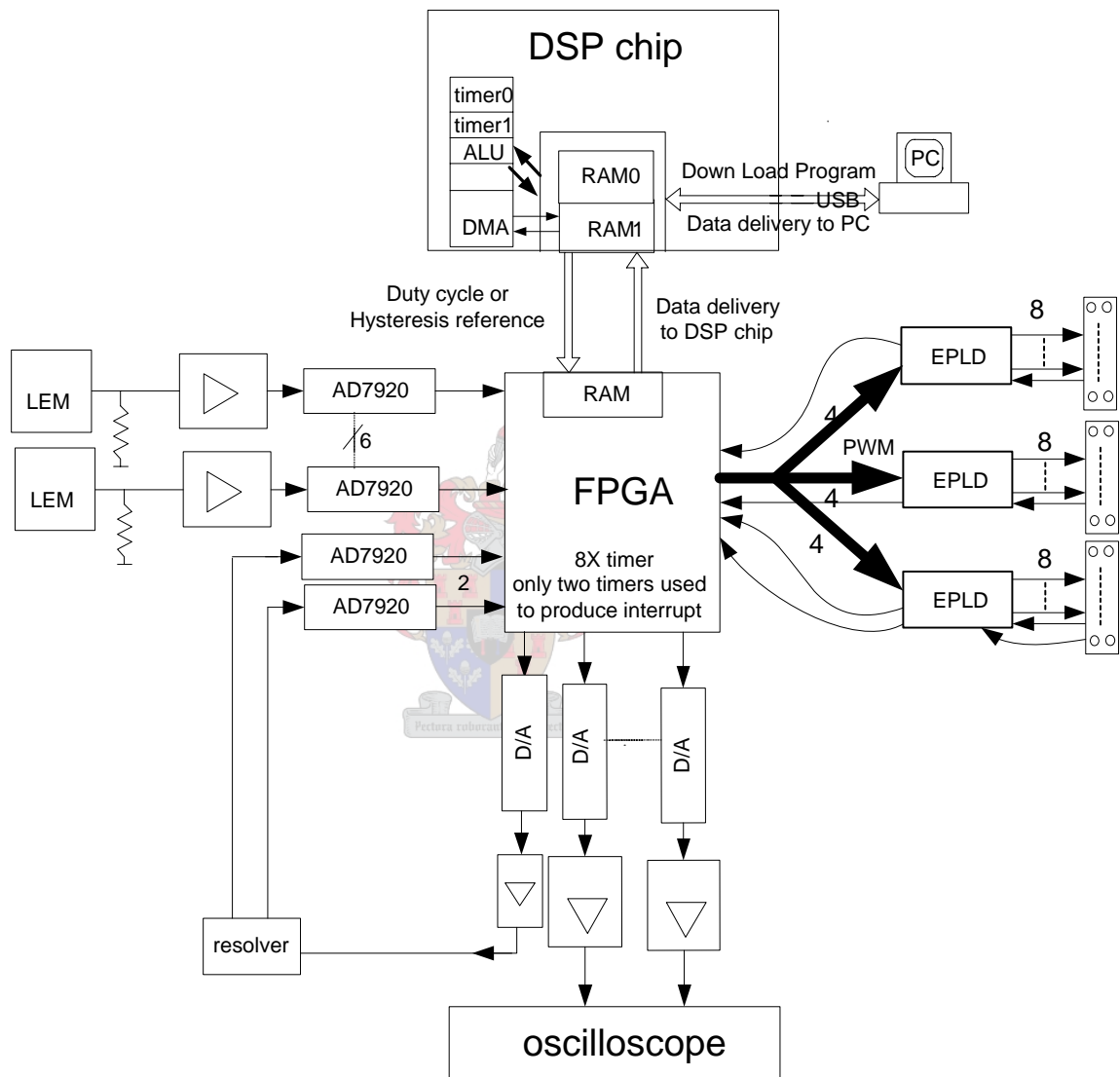
Fig. 6.4. Block diagram of DSP controller.

6.2   Air gap flux density versus field current

In order to investigate the flux density waveform distribution in the air gap and its amplitude the modified wound rotor of the IDCM described in Appendix B is used. Photos of the rotor, stator and the assembled motor are shown in Figs. A.6 – A.8 of Appendix A. For this

investigation three adjacent stator phases are supplied with dc currents as shown in Fig. 6.5. The phases are connected in order to get the phase current set up as $i_a = -i_c = -2i_d = I_F$ (from Fig. 3.3 at time $t = t_1/2$).

The rotor phase induced voltage is obtained by opening all the rotor phases, driving the induction motor with a dc motor at a speed of 120 rpm ($f = 2\,Hz$) and varying the stator field current. The induced voltage waveform in one case, with the stator current equal to 3A, is shown in Fig. 6.6. When the measured waveform of Fig. 6.6 is compared with the simulated results Fig. 4.20(b), good agreement is obtained. This confirms that the waveform of Fig. 4.20(b) from the FE analysis is correct. The flux density can be estimated by modifying eqn (3.11) as

$$B = \frac{E}{2\ N_r\ l\ \omega_{sl}\ r} \tag{6.1}$$

With E and ω_{sl} measured, the results of flux density versus field current are shown in Fig. 6.7. Also shown in Fig. 6.7 are the theoretical and FE calculated results which show fairly good agreement.
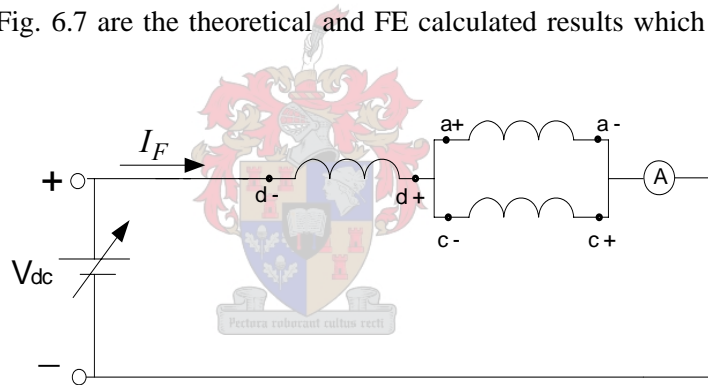
Fig. 6.5. Circuit of the stator phase setup.
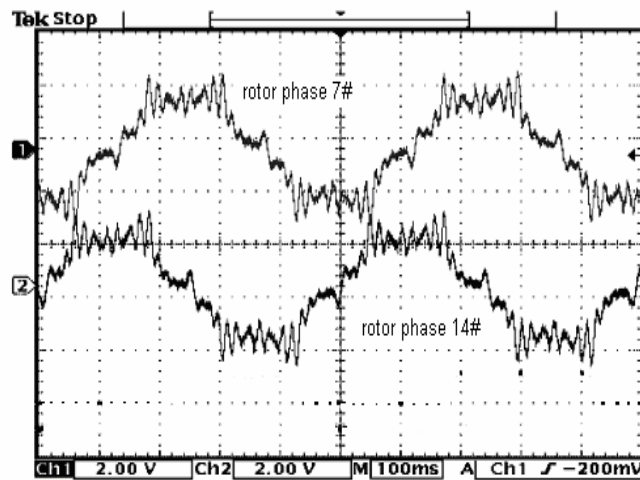
Fig. 6.6. Measured open-circuit rotor induced voltage waveforms (phases 7 and 14) with stator field at standstill.
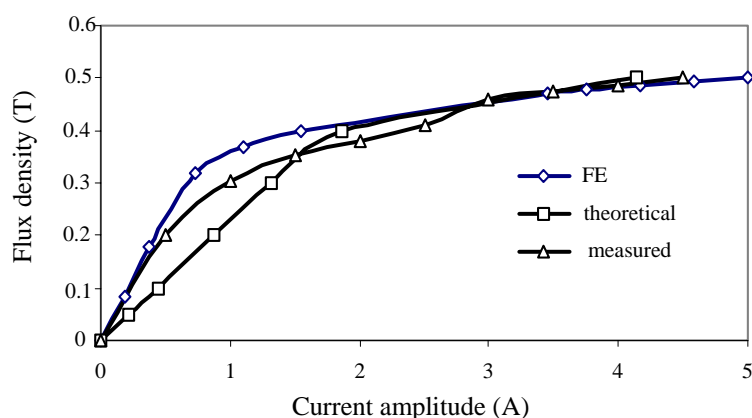
Fig. 6.7. Comparison of results of airgap flux density versus field current I_F.

From Fig. 6.7 it can be seen that with an approximated field current of 5 A an air gap flux density of 0.5 T is obtained. The rated value of the field current is selected to be 3.5 A so as to decrease the saturation to some extent.

6.3   Investigation of the PI and hysteresis current controller

The performance of the current controller is one of the most critical aspects of the IDCM drive in terms of its dynamic response [57 - 60]. The advantages of the PI current controller are that the frequency of the PWM signal is fixed and it is simple to implement. So the investigation of the current controller is first evaluated by using digital PI current controllers. Fig. 6.8 shows phase *a*'s reference and measured current waveforms under PI current control.

It is clear that the PI current controllers are not suitable for these desired current waveforms due to the inherent tracking errors, both in amplitude and phase. Furthermore, the PI controller is sensitive to motor parameters in addition to its poor transient performance. The current waveforms will become worse when the machine operates at high speed and at load condition.

Because of the above drawback of the PI controller used in this current control, a digital hysteresis controller [66 - 75] is utilized to realize the current control. Hysteresis current controllers have excellent transient response and are insensitive to dc bus voltage ripple due to load variations; the controllers are also relatively simple to implement. The function of the digital hysteresis controller used is implemented in the DSP controller by software. The procedure and the algorithm of the hysteresis current controller are given in Appendix D,

section D.5. The measured current waveforms using the digital hysteresis controller with a 0.2 A band are shown in Fig. 6.9. It is found that the phase current waveform can track the reference phase current waveform within a hysteresis band. This hysteresis band affects negatively the torque ripple and machine noise.

A block diagram of the control of the complete IDCM drive system with the hysteresis current controller is shown in Fig. 6.10. The drive comprises of three parts namely the DSP controller, inverter and induction machine.
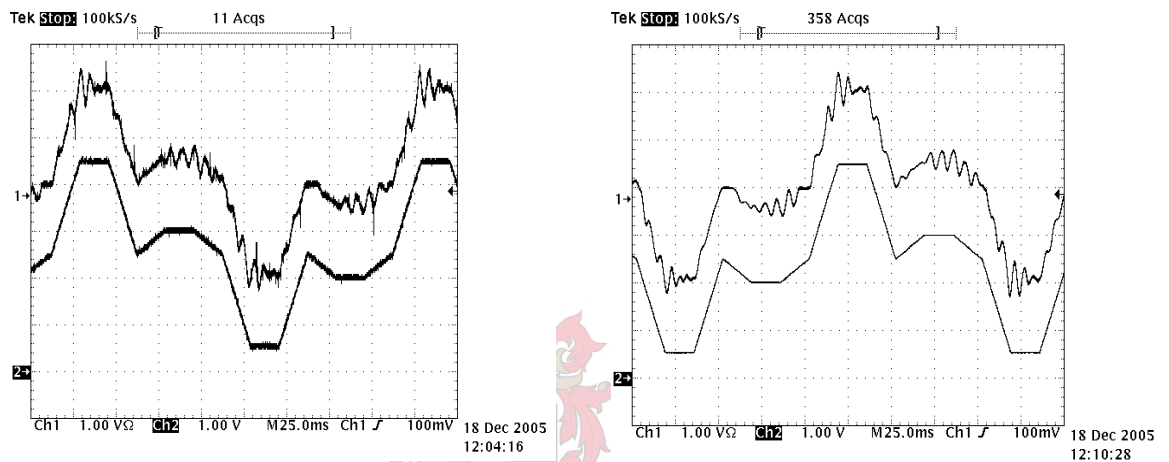
(a) Before filter   (b)   After filter
Fig. 6.8. Measured (trace 1) and reference (trace 2) current waveforms
with PI current control.
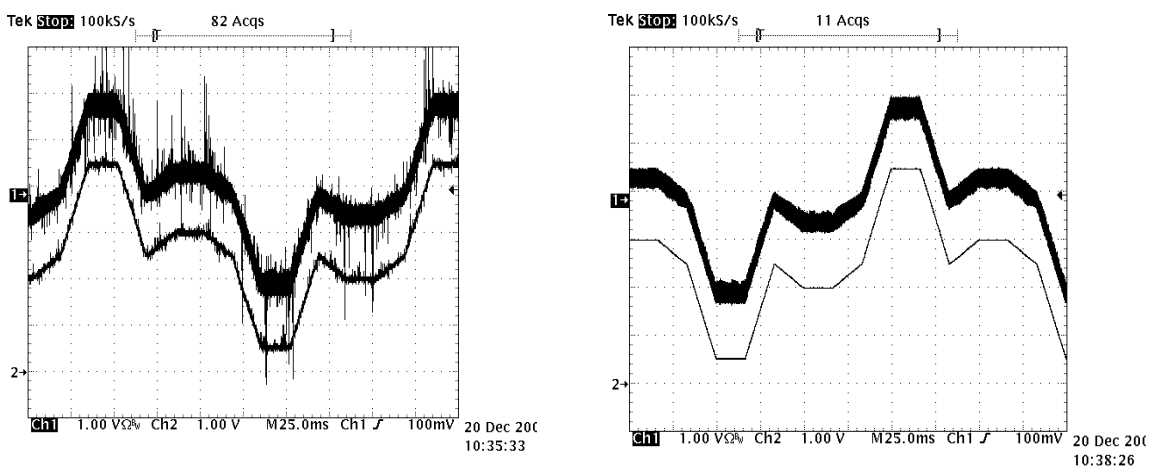
(a) Before filter   (b) After filter
Fig. 6.9. Measured (trace 1) and reference (trace 2) current waveforms with digital
hysteresis current control.
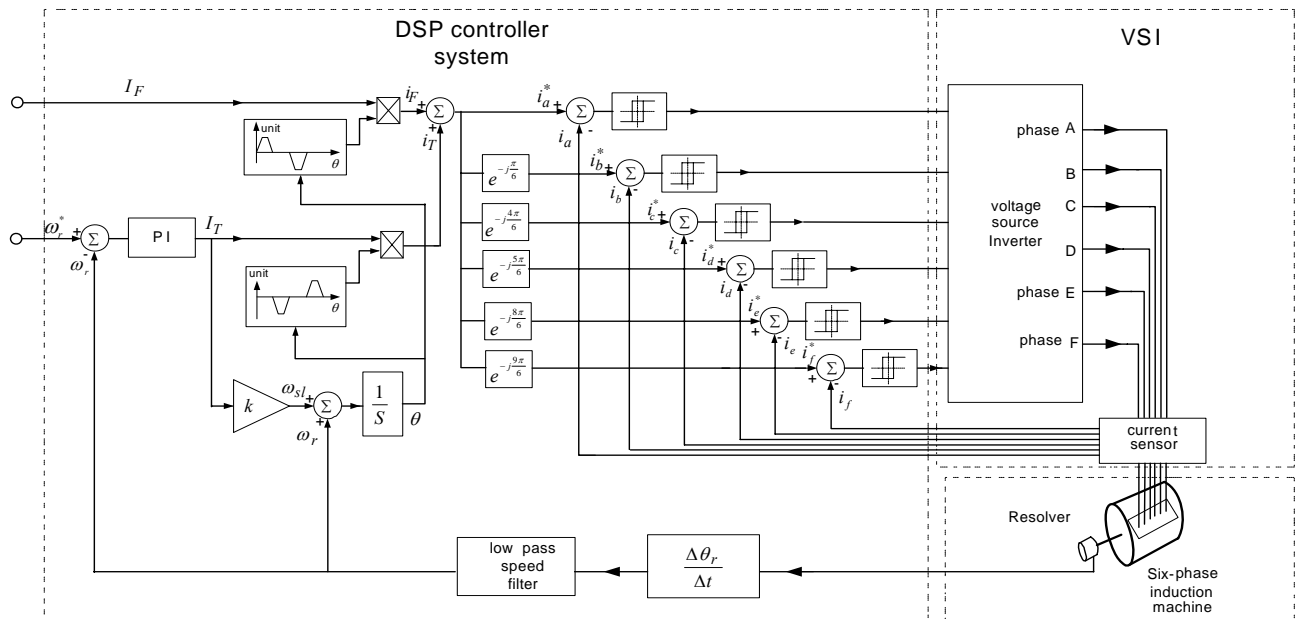
Fig. 6.10. Block diagram of the control of the IDCM drive system

6.4   Determination of the torque current polarity

To operate the IDCM drive correctly it is important to ensure that the field phases act as flux producing phases and the torque phases as torque producing phases in the IDCM, and not the other way round. From Chapter 4 it is known that the amplitude of the induced phase voltage [and thus the amplitude of the phase supply voltage] is higher during torque mode than during field mode. To check, thus, if the IDCM drive is working correctly, the supply voltage must be measured in comparison with the phase current. Fig. 6.11 shows the measured current and voltage (filtered) waveforms of phase *a* of the IDCM drive. It can be seen that in Fig. 6.11(a) the field current leads the torque current and in Fig. 6.11(b) the torque current leads the field current, as is also explained in Fig. 6.12. In effect the only difference between the two current waveforms is the difference in the torque current polarity. According to the IDCM operation principle, where the supply voltage is higher during torque mode, it is clear that the drive operates correctly in the case of Fig. 6.11(b), that is the case where the torque current leads the field current.

To further verify that the above is correct the torque of the IDCM drive is measured for the two cases of Fig. 6.11. The results are shown in Figs. 6.13 and 6.14 for respectively standstill and running conditions. It is clear that the drive produces more torque with the correct torque current polarity and there is also a much more linear relationship between the torque and torque current of the drive.

(a) Field current leading torque current.   (b) Field current lagging torque current.
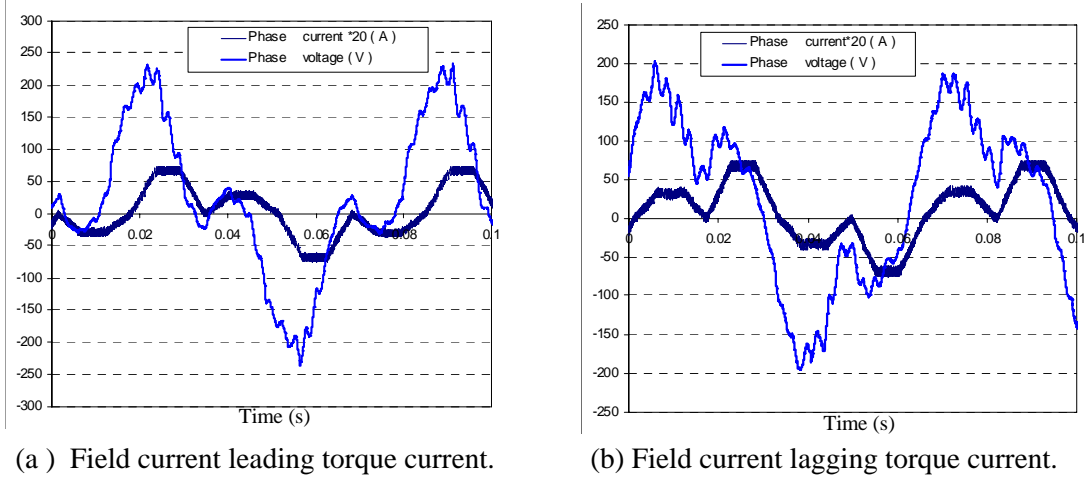
Fig. 6.11. Phase *a* current and filtered supply voltage waveforms.
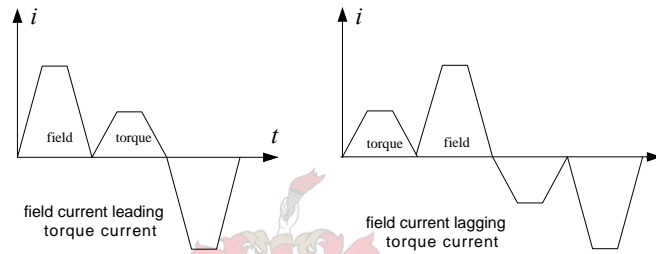
Fig. 6.12. Sequence of field and torque currents.
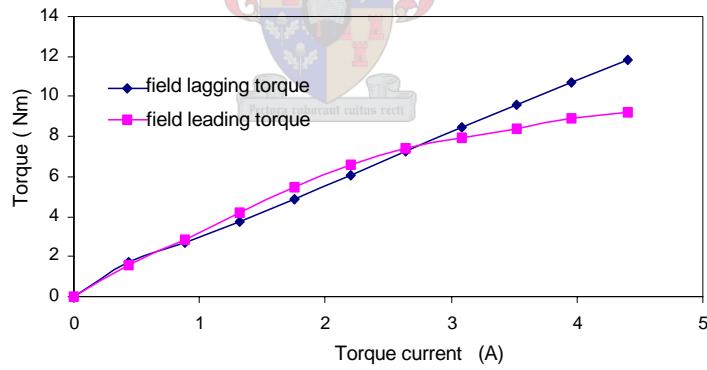
Fig. 6.13. Torque test with rotor at standstill.
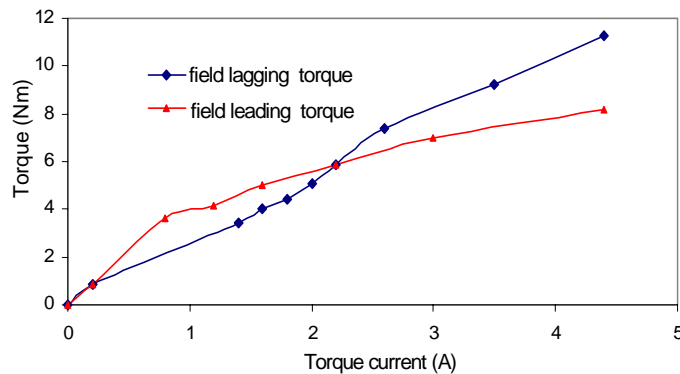
Fig. 6.14. Torque test at rotor speed of 800 rpm.

6.5   Static torque test

The static torque test is carried out at certain torque currents with rated field current and with the rotor at standstill. The measured results are shown in Fig. 6.15. For the purpose of comparison the results from the theoretical calculation and FE analysis are also shown in Fig. 6.15.

It can been seen from Fig. 6.15 that a very good agreement is shown between the theoretical and FE calculations, but a substantial lower torque is measured. The reason for the latter is that the waveform of the rotor induced phase winding current deviates from the assumed waveform of Fig. 3.9 of Chapter 3. The study of the rotor induced phase current is investigated through practical measurements in section 6.11. Also, it must be mentioned that the slip-ring-brush contacts cause considerable increase in the rotor phase resistance of the two measured rotor phase windings; the other rotor phase windings are short circuited within the rotor. This considerably reduces the induced currents in the measured rotor phase windings and negatively affects the generated torque.

Another important conclusion which can be drawn from Fig. 6.15 is that the measured results also reveal a linear relationship between the torque and torque current of the six-phase IDCM drive. This is very important as it shows that MMF balance or zero quadrature flux is maintained in the motor by the drive controller independent of the torque (load) current.
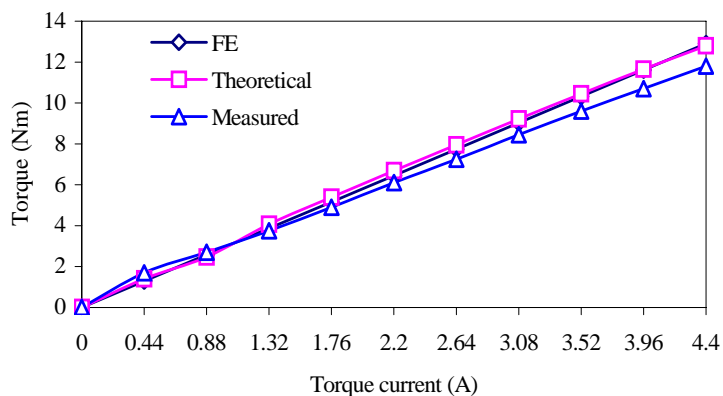
Fig. 6.15. Torque versus torque current I_T at rated field current and with a locked rotor.

6.6   Verification of *k* value

The value of *k* is a very important parameter in the torque and speed control of the drive system. This control parameter is the ratio between the slip speed and the torque current as shown in Fig. 6.10 and for clarity also shown in Fig. 6.16. In this section the influence of the

k value on the field and torque phase voltages is investigated. This is done by performing a locked rotor test with $I_T = 2.2$A and $I_F = 3.5$A. Different values of *k* are used in the test of the drive and the effects on the field and torque phase voltages are observed. Some of these voltage waveforms are shown in Fig. 6.17. For different *k* values, the ratios of the field voltage amplitude over the torque voltage amplitude, V_f / V_t, are investigated and the results are shown in Fig. 6.18.
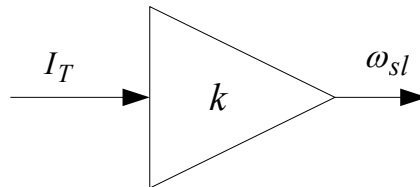
Fig. 6.16. Relationship between I_T and ω_{sl} .
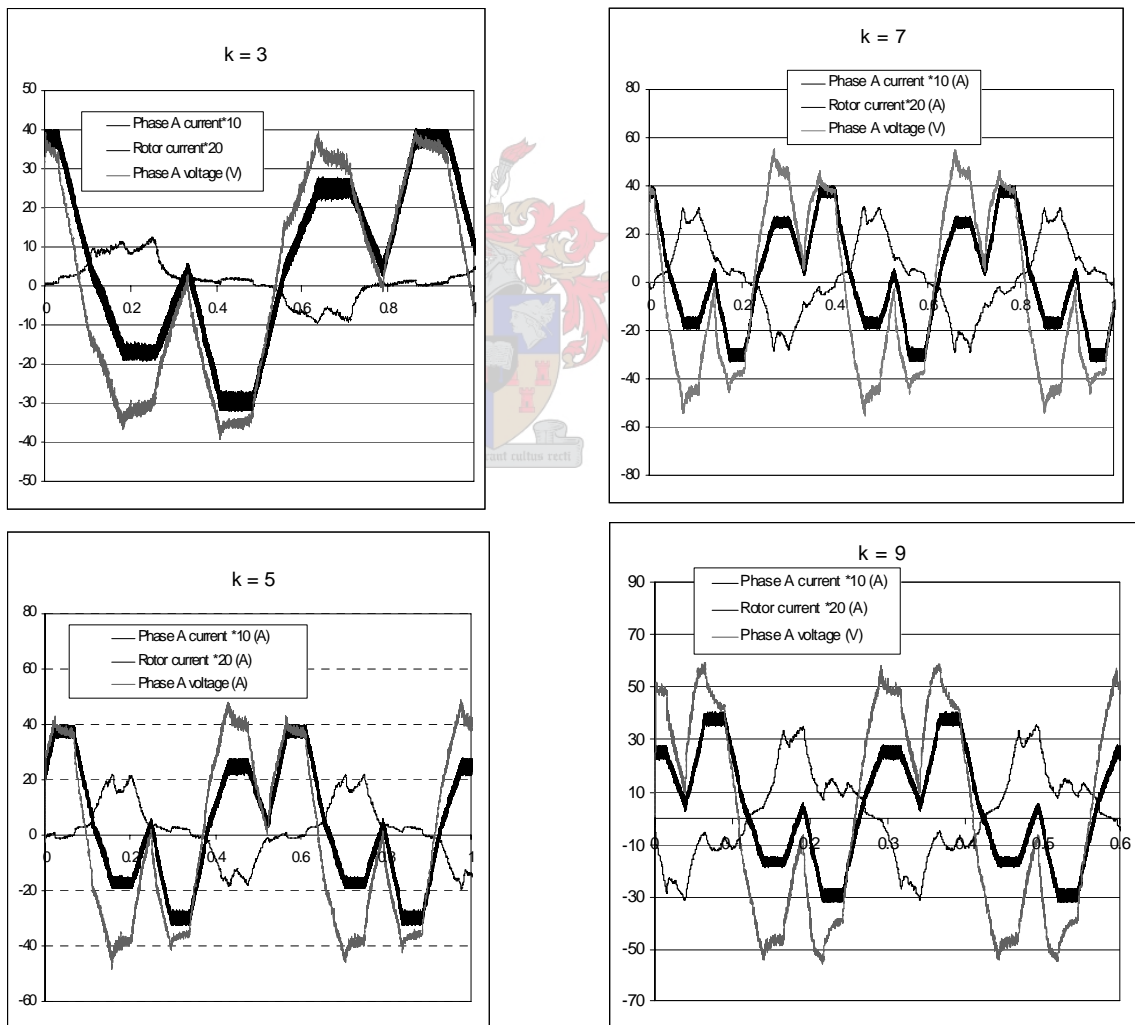
Fig. 6.17. Current and filtered supply voltage waveforms of stator and rotor phases for different *k* values.
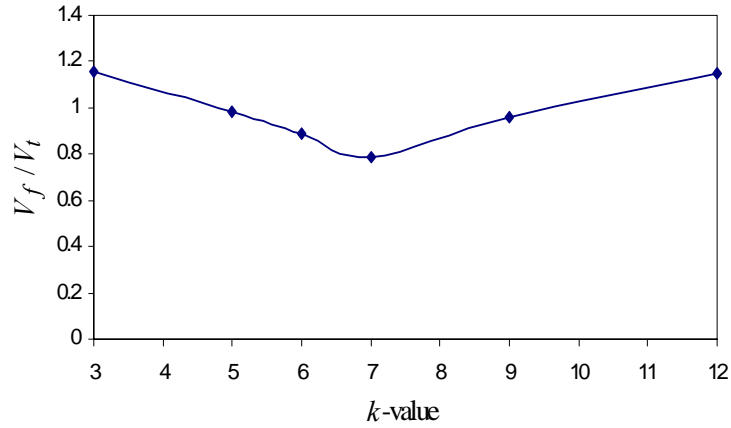
Fig. 6.18. Measured ratio of V_f / V_t versus k at locked rotor.

According the operation principle of the IDCM drive, the ratio V_f / V_t should be a minimum at the MMF balanced condition.   At the MMF balanced condition the value of the stator mutually induced voltage, as discussed in section 4.8, is a minimum in the field current region (ideally it is zero) and is a maximum in the torque current region. Hence, the MMF balanced condition will occur when V_f / V_t is a minimum. From Fig. 6.18 it is found that the V_f / V_t – ratio is a minimum when k is equal to 7.   This is in good agreement with the theoretical analysis of k as done in section 3.5.

Finally, it can be seen in Fig. 6.16 that the measured rotor phase current waveform shifts slightly (phase shift) as k increases, with the correct position and waveform at k between $k = 5 – 7$. This shift is due to a shift in the air gap flux density caused by the unbalanced MMF condition or non-zero quadrature flux condition. Furthermore, it can be seen that the induced rotor currents are high with high k-values. This can be explained from Fig. 6.16 that with high k-values the slip frequency is high, and thus according to eqns (3.11) and (3.12), the induced voltage and current will be high.

6.7   Torque versus torque current with the machine rotating

The relation between torque and torque current of the IDCM drive is investigated by operating the drive at 800 rpm and keeping the speed constant by means of the PI speed controller. The measurements of torque versus torque current are performed with different k-values [eqn (3.21)] used in the software as discussed in section 6.6. The measured results are shown in Fig. 6.19. The jitter in the results is due to measurement tolerance. Nevertheless, it can be seen that close results are found of torque versus torque current with $k = 7$ and $k = 10$. Also with $k = 7$ and $k = 10$ there is a more linear relationship between torque and torque

current of the drive. With these *k*-values there is good agreement with theoretical and FE calculations from previous chapters.

It can be seen from Fig.6.19 that with high *k*-values [like *k* = 15] the torque is higher. This can be explained, as earlier, that with high *k*-values the induced rotor currents are high, generating a high torque. However, it is observed that at high torque current values the torque drops. This aspect is difficult to explain and must be further investigated for good explanation. However, the difference in the torque versus torque current curves of Fig. 6.19 in general can be attributed to (i) the MMF unbalanced condition, thus, a disturbed air gap flux density condition and (ii) temperature effects. To conclude, it is important to mention that with too high or too low k-values decoupled control between the field and torque circuits is lost.
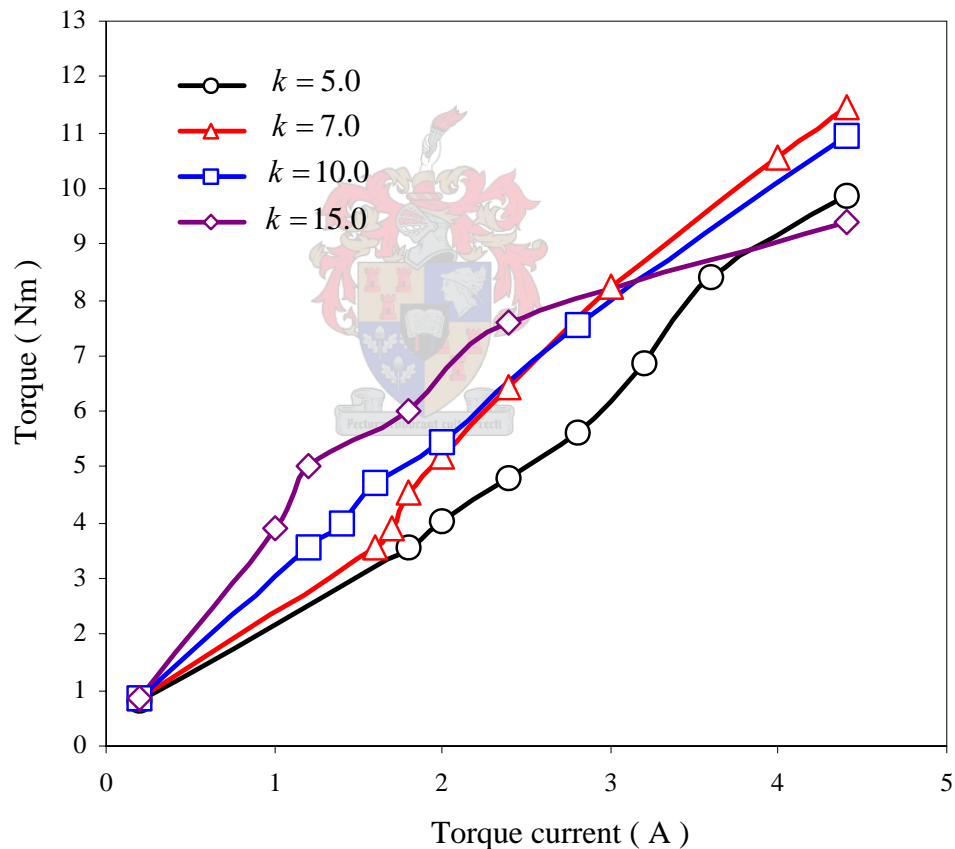
Fig. 6.19. Measured torque versus torque current I_T at rated field current and 800 rpm.

6.8   Torque response

The torque response of the IDCM drive to a step torque current command is investigated in this section. This is done by conducting a locked rotor test with I_F = 3.5 A and a step in the

torque current of 2.2 A. The results of the measured torque and measured stator phase current response for a step torque current command are shown in Fig. 6.20.

Fig. 6.20 shows that a fast torque response of the drive is obtained. The ripple torque is visible in the measured torque waveform. These measured results compare well with the simulation results of Fig. 5.24 in section 5.2.3.
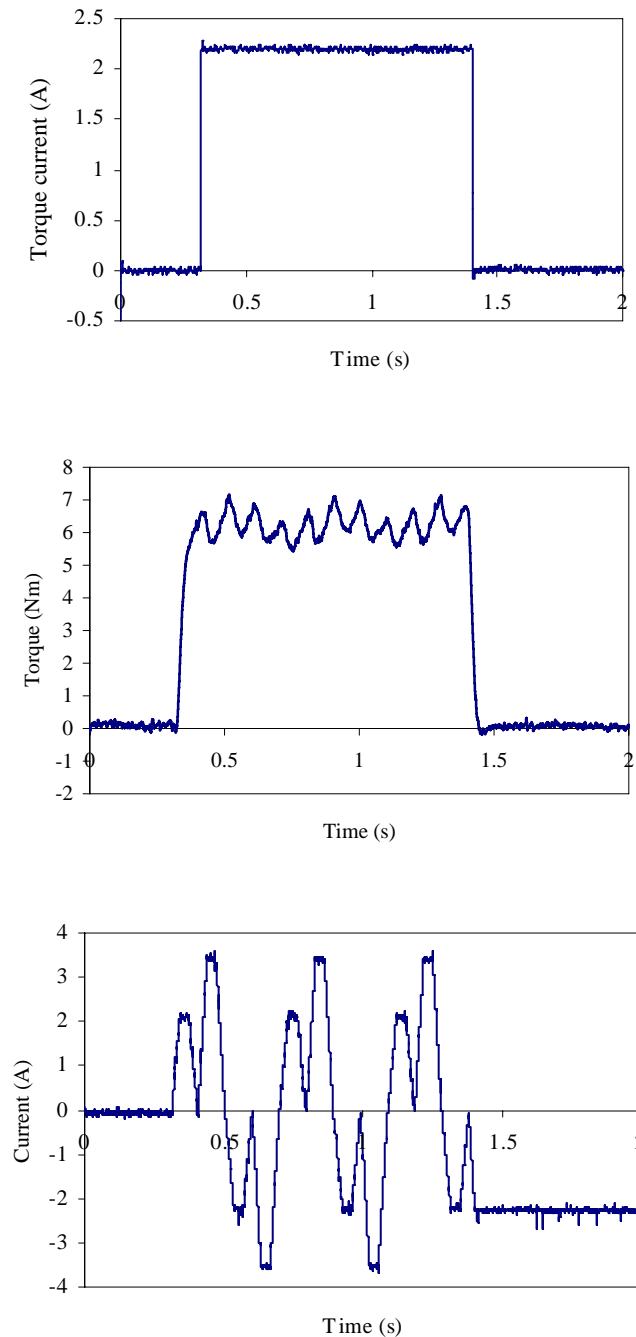
Fig. 6.20. Torque response to step torque current command (filtered)
(from top to bottom: step torque current command; measured torque response;
measured phase *a* current).

6.9   Dynamic performance test

The dynamic performance of a motor drive includes mainly the accelerate-decelerate (start-stop) performance of the drive and the speed response of the drive to load disturbances. In this section the measured dynamic performance of the six-phase IDCM drive is presented.

6.9.1   Start-stop performance test

This test is performed to investigate the responses of the actual rotor speed and torque current to a 500 rpm rectangular rotor speed command which means the motor is started-up and then stopped. The measured results of the start-stop test of the IDCM drive are shown in Fig. 6.21 and Fig. 6.22. It can be seen that the speed-up time is quite long (around 5 seconds). This is due to the fact that (i) the drive system has a heavy moment of inertia mainly from the flywheel, and (ii) the torque current, I_T, is limited at 4.5 A [see Fig. 6.22], which limits the rotor acceleration speed.
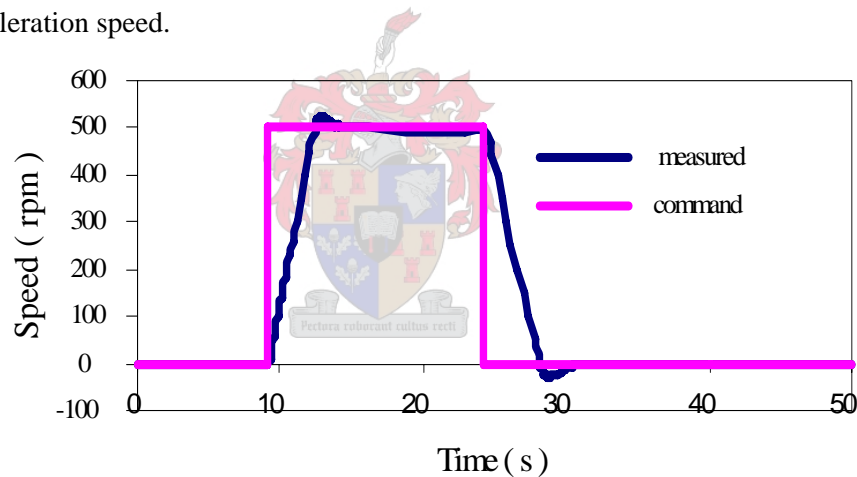
Fig. 6.21. Measured start-stop speed response of IDCM drive.
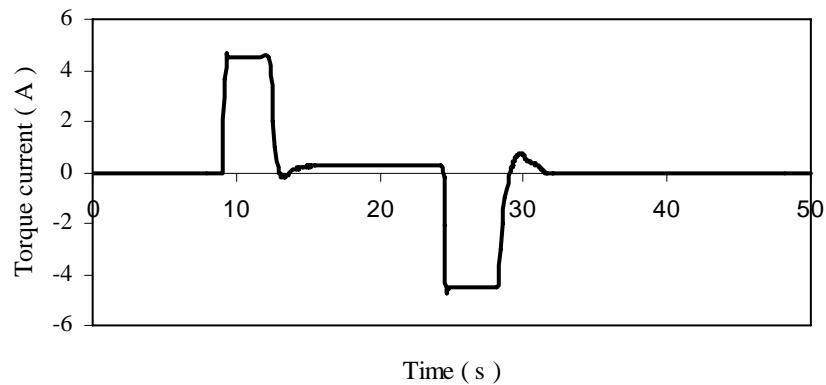
Fig. 6.22. Measured torque current of IDCM drive for start-stop speed command

100

6.9.2   Load disturbance test

The load disturbance test is conducted to investigate the sensitivity of the PI speed controller to an external load disturbance. The IDCM drive is set to operate at 800 rpm in the steady state. A sudden load is applied to the IDCM drive system and the speed and torque current response are recorded as shown in Fig. 6.23; two different proportional constant values are used in this test. It is clear that good performance is obtained with $Kp = 1$ and $Ki = 2$ of the PI speed controller as designed in section 5.1.1. These measured results are consistent with the simulated results of Fig. 5.23(a). The measured speed and torque current response prove that the proposed six-phase IDCM drive control system is robust and has good speed disturbance rejection.

6.10   Induced voltage evaluation

For the experimental IDCM two rotor phases are available to measure their induced voltages and currents. The induced voltage in the rotor windings is tested by open-circuiting all the rotor windings, supplying the desired stator current waveform at a certain slip frequency and making the torque current component equal to zero. Fig. 6.24 shows the measured stator phase *a* current and one rotor winding induced voltage of the IDCM drive. It can be seen that the induced voltage waveform has an approximately rectangle shape, similar to that of permanent magnet brushless DC motors. To some extent, the induced voltage waveform also represents the air gap flux density waveform, which means that the flux density distribution has the desired flat-top shape. The measured induced voltage waveform compares well with the FE calculated result of Fig. 4.18 in section 4.6. The measured average amplitude of the rotor induced voltage versus slip speed is shown in Fig. 6.25. For the purpose of comparison the results from theoretical and FE calculations are also shown. It can be seen that there is excellent agreement between measured and calculated results.

(a) $Kp = 1$, $Ki = 2$ (b) $Kp = 20$, $Ki = 2$
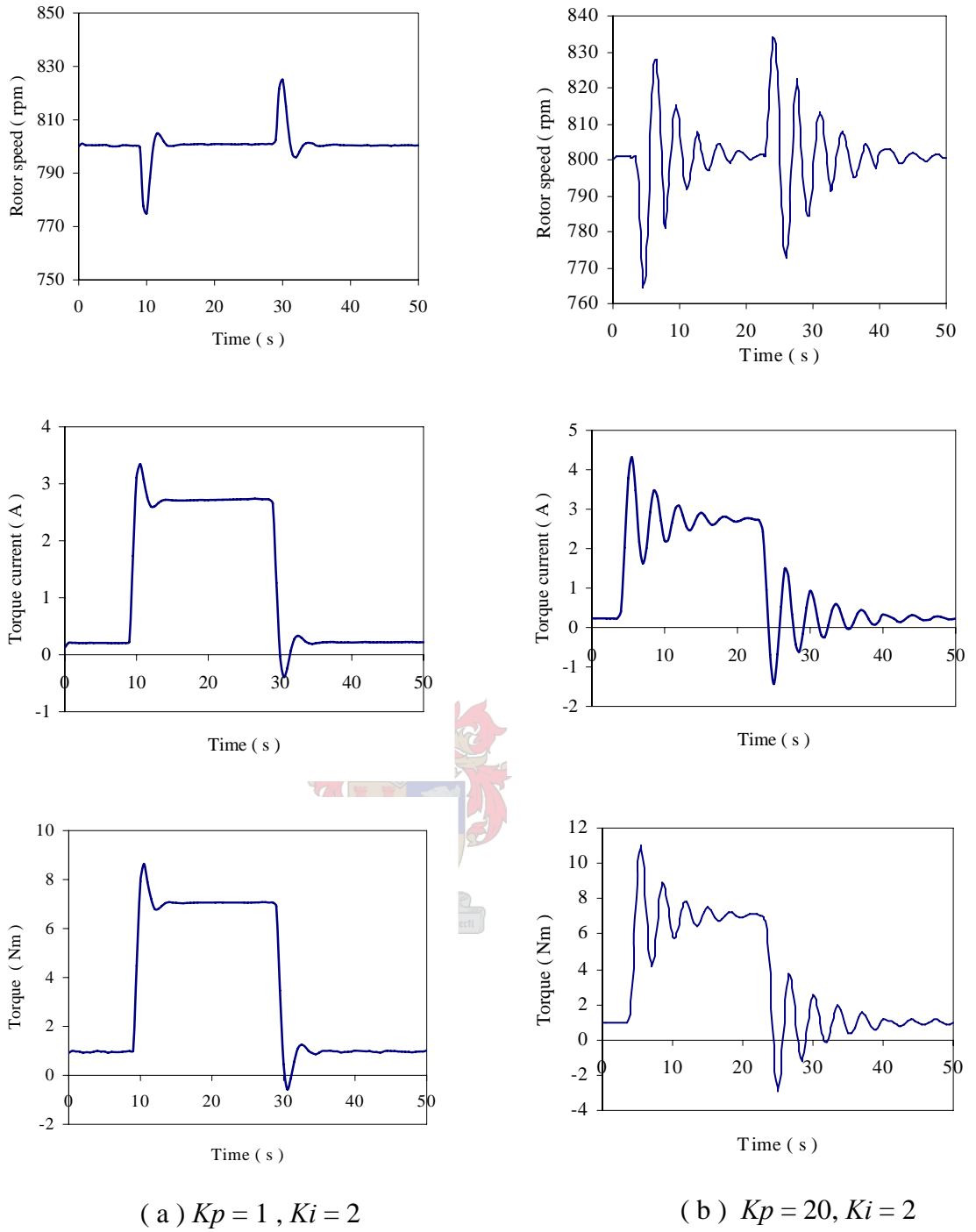
Fig. 6.23. Measured speed and torque current response of IDCM drive for a disturbance load
with proportional constant *Kp* parameter.
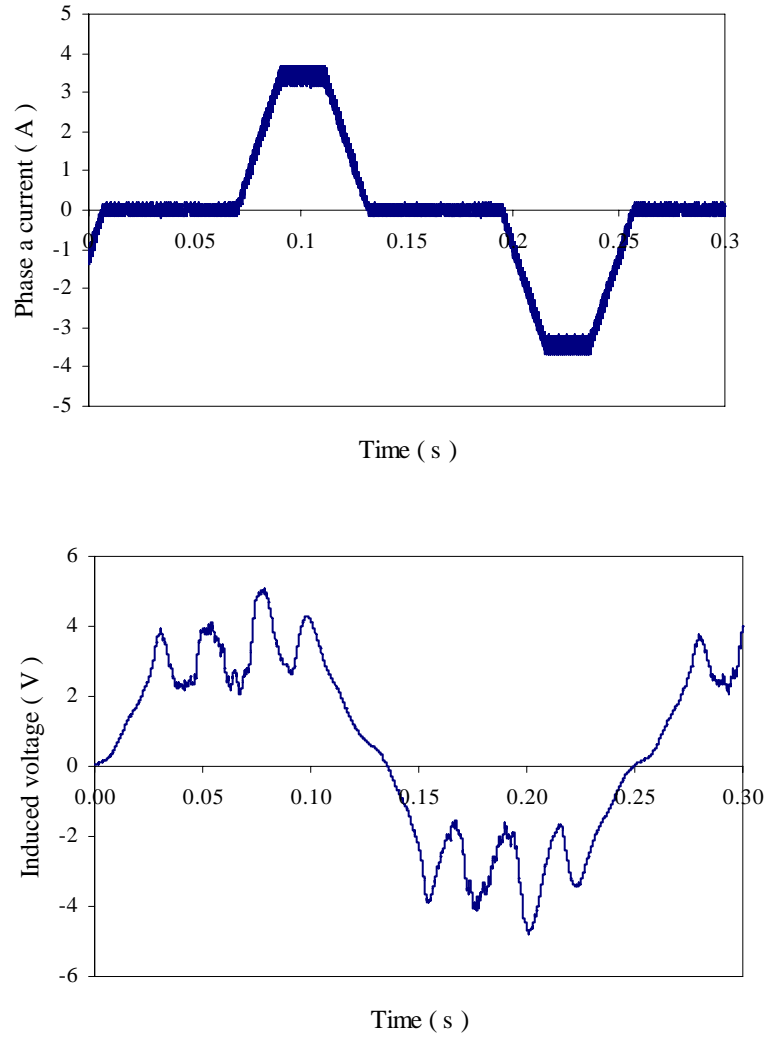
Fig. 6.24. Measured stator current and rotor induced voltage.
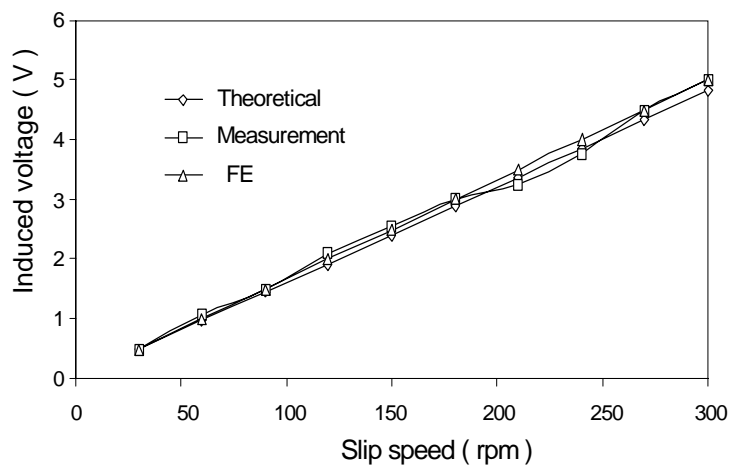
Fig. 6.25. Rotor induced voltage amplitude versus slip speed.

6.11   Rotor phase current waveform

The induced current of a rotor phase winding is measured under the conditions that the rotor is at standstill and the stator field is rotating at a certain slip speed. The measured stator and rotor phase current waveforms are shown in Fig. 6.26, with the average (filtered) rotor phase current waveform shown in Fig. 6.27. The waveform of Fig. 6.27 is of particular interest. It is clear that the waveform is quasi-square shaped, however, it deviates from the assumed ideal waveform of Fig. 3.9, with less net rotor current flowing; the latter will lead to a reduction in developed torque. The flat-topped amplitude of the measured rotor current is also quite low compared to the rated value of $I_r = 5.6$ A given in Appendix B. The reason for this is the relatively high slip-ring-brush contact resistance, which increases the net rotor phase resistance of the measured phase winding by a factor 4.67. The rotor is constructed in such a way that only 2 phases have slip rings and the rest have not as seen from Figure A.7 in Appendix A.2. The above mentioned ratio is thus given as the ratio of the rotor resistance with slip rings and the rotor resistance without.

The measured induced rotor current amplitude [multiplied by the factor of 4.67 to approximately compensate for the high slip-ring-brush resistance] versus the stator torque current is shown Fig. 6.28. Also shown in Fig. 6.28 are the theoretical calculated results, which show fairly good agreement.
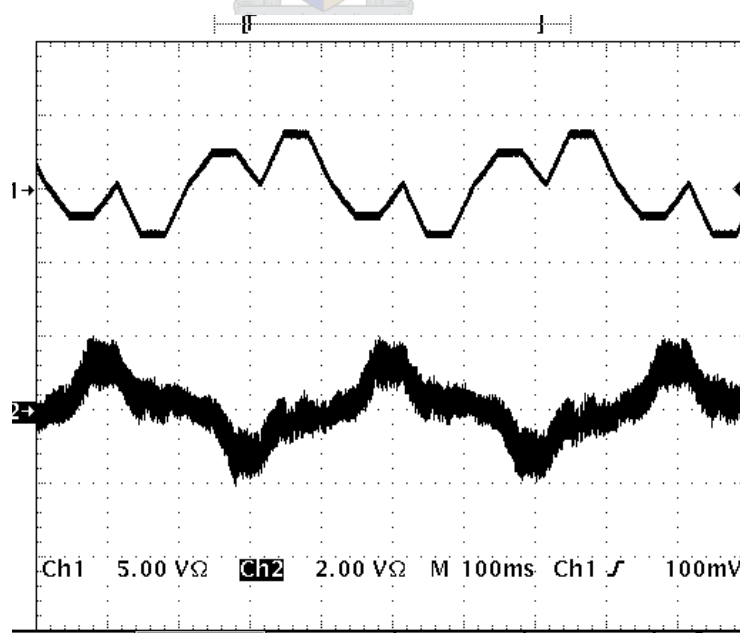
Fig. 6.26. Measured current waveforms of stator phase (trace 1) and rotor phase (trace2).
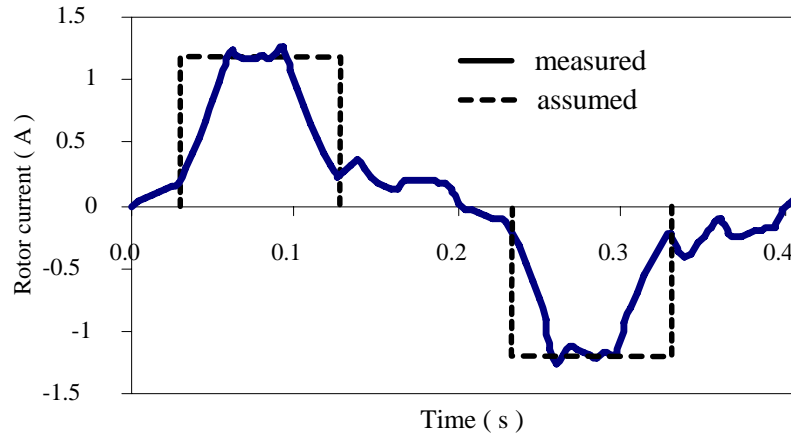
Fig. 6.27. Measured (filtered) rotor phase current waveform.
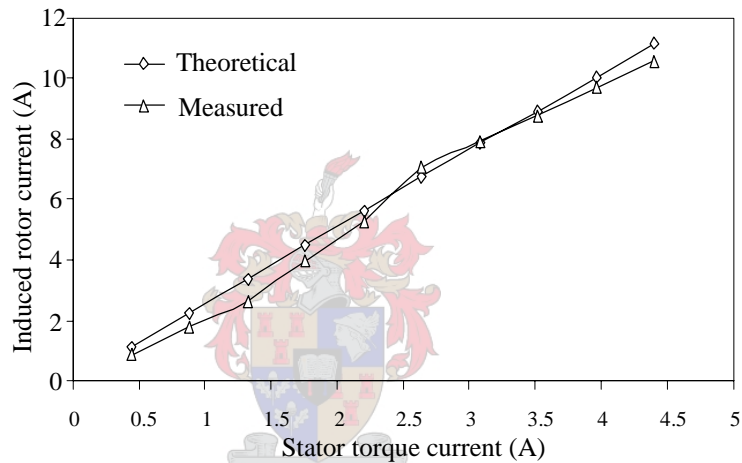
Fig. 6.28. Rotor phase current (I_r) versus torque current (I_T).

6.12   Conclusion

In general good agreement is found between calculated and measured results of the proposed six-phase IDCM drive with its novel phase current control. The measured rotor induced voltage and current also validate the IDCM principle, however, a substantial difference between assumed and actual rotor current waveform is found. It is shown experimentally that the field and torque current components can be controlled separately without any coordinate transformation, hence emulating separately excited dc motor control.

7   CONCLUSIONS AND RECOMMENDATIONS

Rotor flux linkage oriented control is widely used in induction motor drives rather than air gap flux linkage control. This is due to the fact that the flux linkage and slip speed can be decoupled in this control strategy. Air gap flux linkage orientated control should not be disregarded as it has major advantages such as that the airgap flux can be measured directly which gives an indication of the saturation level of the machine. This advantage is, however, outweighed by disadvantages. It would be of great benefit to overcome these disadvantages. This is where the new control strategy proposed in this thesis comes from.

A novel strategy for the direct control of the torque and field currents applied to the six-phase induction motor drive was proposed. This novel current control strategy benefits the developed torque of the motor as well as simplifying the control algorithm by removing the complex transformations used in flux orientated control. The first part of the thesis deals with the theoretical work that includes the machine modelling, FE analysis and the simulation of the drive system. After theoretical analysis was done, a six-phase IDCM drive system was built and the control strategy was experimentally verified.

This chapter gives a brief summary of the findings, contributions and recommendations of the project.
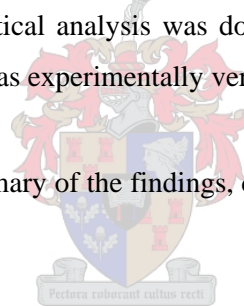
7.1   Electromagnetic torque and flux oriented control of induction motor

An important aspect is the mechanism of torque production in electrical motors. This has been explained and three expressions for the developed torque of an induction motor were derived. Each of these expressions corresponds to a flux oriented control strategy. A motor model for the six-phase induction motor was furthermore obtained from literature. A control strategy for the six-phase motor was also obtained to show the complexity of controlling such a machine. After reviewing the literature and studying the motor model as well as the control of the six-phase induction motor, the following findings were made:

- It was found that if a special reference frame is chosen, i.e. fixed to the rotor flux linkage or the air gap flux linkage or the stator flux linkage space phasor, the expression for the torque is similar to that of the expression for the torque of a separately excited dc motor. Therefore by selecting the appropriate reference frame as well as the type of flux-

orientated control, field and torque current control for an induction motor can be performed as in a separately exited dc motor.

- Among the three flux oriented control strategies, the rotor flux oriented control (RFOC) is usually employed in induction motor control. This is due to the fact that with RFOC the slip and the flux are decoupled. Furthermore, RFOC is relatively simple to implement compared to the stator and air gap flux oriented control strategies. However, the stator and air gap flux oriented systems have the advantage that the air gap flux and stator flux can be measured directly. Air gap flux control has the added advantage that the saturation level is known through the measured air gap flux. If the issues of the control algorithm complexity and the coupling of the slip and flux can be solved, air gap flux oriented control can be considered as a viable control strategy.

- Rotor flux oriented control can be extended to the six-phase induction motor. However, the extra transformations needed, increase the complexity of the control system considerably.

- As mentioned, flux oriented control can be used to make the operation of the induction motor emulate that of the separately excited dc motor. This, however, increases the complexity of the control especially when implemented in a six-phase induction motor. The control strategy proposed by the author deals with this problem by using a novel field and torque control strategy.

7.2   Novel current control theory for six-phase induction machine

In this thesis a control strategy was proposed based on the control principle of a separately excited dc motor. This strategy led to a special current waveform, adding the advantage of a rectangular flux density waveform in the air gap of the induction motor. By using this strategy the field and torque currents can be controlled directly.

The important results obtained from the use of the proposed special current waveform are as follows:

- The resultant field intensity due to the field MMF in the air gap is approximately trapezoidal, which is similar to the air gap field intensity in a dc motor.

- The amplitude of the resultant field intensity is constant. This is due to the fact that the amplitude of the resultant MMF is constant as given by eqn (3.5).

- The plateau angle of the resultant air gap field intensity waveform was found to have a minimum value of $\pi/2$ electrical.

- The phase displacement between H_{tf} (total field intensity produced by field currents) and H_{tt} (total field intensity produced by torque currents) was found to be $\pi/2$. This verifies that the special current waveform configuration produces perpendicular field and torque magnetic fields.

The rotor current waveform was assumed to have the same shape as the air gap flux. With this assumption it is found that the rotor current field intensity, H_{tr}, is opposite to that of the torque current intensity, H_{tt}. This means that it is possible that the field intensities in the air gap due to the rotor MMF and the stator torque current MMF can cancel each other out.

The significant aspects that arose from the use of the special phase current waveforms are as follows:

- The electromagnetic torque production principle was described and the torque equation for the machine was derived. With this torque equation, the torque was calculated for the specific six phase IDCM.

- An approximate magnetic circuit (AMC) was developed to calculate the field current amplitude for a certain air gap flux density. It was found that, with a field current amplitude of 4.14 A, the air gap flux density equals 0.5 *T*. However, for the specific two-pole machine investigated the saturation level in the stator and rotor iron yokes is high with an airgap flux density of 0.5 T. The field current therefore was reduced to 3.5 A in the analysis. The use of the proposed AMC method proved to be worthwhile.

- The field MMF harmonics in the air gap with time and space were analysed with the use of an approximate method. It was found that the amplitude of the harmonics decreases with the increase of the harmonic order.

- The per-phase inductance of the IDCM was calculated using the approximate winding function. These results were compared to the results obtained from finite element analyses. The calculated results do not match the finite element analyses. The reason for this is that the saturation effect was not taken into account when using the winding function.

7.3   Finite element analysis

The six-phase IDCM per phase equivalent circuit parameters were determined as well as the performance parameters calculated using finite element analysis. The following results were obtained:

- The air gap flux density was evaluated and it was found that (i) the flux density versus field current shows that for a flux density of $B = 0.5$ T saturation occurs in the core of stator and rotor, (ii) the air gap flux density has a quasi square waveform like in a dc motor, and rotates synchronously with the supply of the special phase current waveforms. However, the amplitude and the plateau angle of the air gap flux density are not very constant. (iii) The air gap flux density is little affected by the balanced stator torque and rotor currents; the balance stator torque and rotor currents used in the FE analysis are from theoretical calculations.

- The investigation of the torque performance of the IDCM drive shows that the static torque versus torque current has a near linear relationship. It was also found that the torque ripple is due to the stator phase current commutation.

- The vector method is used through FE analysis to determine the stator torque to rotor current ratio to obtain zero quadrature flux linkage in the machine. Good agreement is found between theoretical and FE calculations of this current ratio.

- The waveform of the stator mutually induced phase voltage determined through time-stepping FE analysis shows clearly that this voltage is high in the torque mode region but practically zero in the field mode region. The study of the IDCM principle, thus, shows that the developed torque can be calculated by

$$T_e = \frac{\sum_{j=a}^{f} (e_{mj}\, i_j)}{\omega_e}, \qquad (7.1)$$

where e_{mj} is the jth stator phase instantaneous mutually induced voltage and i_j is the jth stator phase instantaneous current.

- The FE calculated results of the stator per phase induced voltage show that the stator torque current has little effect on the waveform of this voltage. This proves that the flux linkages of the stator torque and active rotor phases are effectively cancelled, which simplifies the per phase equivalent circuit of the IDCM. This also simplifies the modelling and simulation of the IDCM drive.

7.4   Matlab Simulation of IDCM drive system

A simulation model of the six-phase IDCM drive was developed in this thesis using the Matlab/Simulink software. This simulation model includes, amongst other things, a six-phase hysteresis current controller, a PI speed regulator and a complete model of the IDCM. The torque and speed-control performance of the drive system was simulated according to specified conditions. These simulated results show that the IDCM drive can have fast dynamic response.

7.5   Experimental evaluation of IDCM drive

In this research a small (around 2 kW) six-phase induction machine drive system with its control software was developed, built and tested.

The laboratory experiments were performed by using the proposed special phase current waveforms. The IDCM drive torque performance was investigated for the static and running tests. The measured results show a good agreement to the theoretical and FE calculated results. The dynamic performance of the IDCM drive system including the speed PI controller and start up characteristic was also investigated, and the results were consistent with Matlab results. The measured rotor induced voltage and current validate the IDCM principle.

In summary, it was proven experimentally that the field and torque current components of the IDCM drive can be controlled separately without any coordinate transformation, as such, emulating separately excited dc motor control.

To conclude, the thesis demonstrates for the first time a novel control strategy with direct flux and torque control of a six-phase induction motor. This will open a new door in the field of multiphase induction motor drives with simple control and without scarification of drive performance.

7.6   Recommendations

Further in-depth investigation is necessary on the proposed IDCM drive with its special phase current waveforms. In this regard it is recommended that the following research be undertaken:

- One of the important components of the six-phase induction motor drive system is the machine itself. It is, therefore, necessary in further research to design the six-phase induction motor optimally specifically for IDCM operation. It must be noted again that the IDCM used in this research was a 4-pole machine that has been modified to a 2-pole machine; hence, from a design point of view the practical machine is not as good.

- It is necessary to investigate the optimum ratio of the number of field phases to the number of the torque phases of the IDCM. It is possible e.g. to use 5-phase or 7-phase IDCMs. Aspects that must be considered in such an investigation are, amongst other things, (i) stator current waveforms and stator current commutation and (ii) the better use of the rotor phase windings [e.g. in a six phase IDCM with three field and three torque phases, only 50% of the rotor phase windings are active at any time].

- The rotor phase current waveform under IDCM operation should be evaluated theoretically as well as through FE time-stepping analysis. This is important as the rotor current waveform directly affects the performance of the IDCM. The calculated results should be validated practically with wound or cage rotors.

- As the six-phase IDCM drive is applicable to large (megawatt) drives, an in-depth investigation should be conducted into the development and evaluation of a large IDCM drive in comparison to other conventional drives.

REFERENCES

[1]   A. M. Trzynadlowski, *Control of Induction Motor*, Academic Press. London. 2001.

[2]   Sakae and Yamamura, *Ac Motors for High-Performance Applications*, Marcel Dekker Inc., New York and Basel 1986.

[3]   I. Boldea and S. A. Nasar, *Vector Control of AC drives*, CRC Press, Inc., Blvd., New York, Boca Raton, 2000.

[4]   W. Leonhard, *Control of Electrical Drives*. Springer Verlag. Berlin. 1985.

[5]   P. Vas, *Vector control of AC machines*. Clarendon Press. Oxford. 1990.

[6]   T. J. E. Miller, *Brushless Permanent Magnet and reluctance Motor Drives*, Oxford, 1989.

[7]   B. K. Boss, *Modern Power Electronics and AC Drives*, Prentice-Hall, Inc. Upper Saddle River, NJ 07458. 2002.

[8]   F. Blaschke, "The principle of the field-orientation as applied to the new 'transvektor' closed-loop control system for rotating-field machines", siemens review. vol.34. pp. 217-220. (1972).

[9]   G. Griva, T. G. Habetler, F. Profumo, "Performance evaluation of a direct torque controlled drive in continuous PWM square wave transition range", IEEE Trans. on Power Electronics. 10(4), pp. 464-471, (1995).

[10]   T. G. Habetler, F. Profumo, M. Pastorelli and L. M. Tolbert, "Direct torque control of induction machines using space vector model", IEEE Trans. IAS. 28(5), pp. 1045-1053, (1992).

[11]   B. Heber, L. Xu and Y. Tang, "Fuzzy logic enhanced speed control of an indirect field-oriented induction motor drive" IEEE Trans on Power Electronics, 12(5), pp. 772-778, (1997).

[12]   J. O. P. Pinto, B. K. Boss, L. E. Borges and M. P. Kazmierkowski, "A neural network based space vector PWM controller for voltage-fed inverter induction motor drives", IEEE Trans. IAS. 36 (6), pp. 1628-1636, (2000).

[13]   M. G. Simoes and B. K. Boss, "Neural network based estimation of feedback signals for vector controlled induction motor drive", IEEE Trans. IAS. 31(3), pp. 620-629, (1995).

[14]   E. E. Ward and H. Harea, "Preliminary investigation of an inverter fed 5-phase induction motor", Proc. IEE 116(6), pp. 980-984, (1969).

[15]   R. H. Nelson and P. C. Krause, "Induction machine analysis for arbitrary displacement between multiple winding sets", IEEE Trans. on Power App. and Syst. PAS-93, pp. 841-848, (1974).

[16]   E. A. Klingshirn, "High phase order induction motors Part–I: description and theoretical consideration", IEEE Trans. on Power App. and Syst. PAS-102 (1), pp. 47-53, (1983).

[17]   E. A. Klingshirn, "High phase order induction motors Part–II: experimental results", IEEE Trans. on Power App. and Syst.. PAS-102 (1), pp. 54-59, (1983).

[18]   T. A. Lipo, "A d-q model for six-phase induction machine", Proceeding on International Conference on Electric Machines (ICEM), Athens (Greece), pp. 860-867, (1980).

[19]   M. A. Abbas, R. Christen and T. M. Hahns, "Six-phase voltage source inverter driven induction motor" IEEE Trans. IAS. 20 (5). pp. 1251-1259. (1984).

[20]   K. Gopakumar, V. T. Ranganathan, and S. R. Bhat, "Split-phase induction motor operation from PWM voltage source inverter", IEEE Trans. IAS. 29(5), pp. 929-932, (1993).

[21]   L. Xu and L. Ye, "Analysis of a Novel Stator Winding Structure Minimizing harmonic Current and Torque Ripple for Dual Six-Step Converter-Fed High Power AC Machines", IEEE Trans. IAS. 31(1), pp. 84-90, (1995).

[22]   D. Hadiouche, H, Razik and A. Rezzoug, "On the modelling and design of dual-stator windings to minimize circulating harmonic currents for VSI fed machine", IEEE Trans. IAS. 40(2), pp. 506-515, (2004).

[23]   A. R. Munoz and T. A. Lipo, "Dual stator winding induction machine drive", IEEE Trans. IAS. 36(5), pp. 1369-1379, (2000).

[24]   Y. Zhao and T. A. Lipo, "Space vector PWM control of dual three-phase induction machine using vector space decomposition", IEEE Trans. IAS. 31(5), pp. 1100-1109, (1995).

[25]   Y. Zhao and T. A. Lipo, "Modelling and control of multi-phase induction machine with structural unbalance, Part I: Machine modelling and multi-dimensional current regulation", IEEE Trans. Energy Conv., 11(3), pp. 570-577, (1996).

[26]   Y. Zhao and T. A. Lipo, "Modelling and control of multi-phase induction machine with structural unbalance, Part II: Field oriented control and experimental verification", IEEE Trans. Energy Conv., 11(3), pp. 578-584, (1996).

[27]   R. Bojoi, M. Lazzari, F. Profumo, and A. Tenconi, "digital field oriented control for dual three-phase induction motors drives", IEEE Trans. IAS. 39(3), pp. 752-759, (2003).

[28]   G. K. Singh, K. Nam, and S. K. Lim, "A simple indirect field oriented control scheme for multiphase induction machine", IEEE Trans. Industrial electronics, 52(4), pp. 1177-1184, (2005).

[29]   H. A. Toliyat and H. Xu "A novel direct torque control (DTC) method for five-phase induction machines", Proceedings of the 2000 applied power electronics Conference. APEC'00. Fifteenth Annual IEEE. vol. 1, pp. 162-168, (2000).

[30]   H. A. Toliyat and H. Xu, "DSP-based direct torque control (DTC) for five phase induction machines", IPEC 2000, Tokyo, Japan, pp. 1195-1200, (2000).

[31]   H. Xu, H. A. Toliyat, and L. J. Petersen, " Rotor Field Oriented Control of Five-Phase Induction Motor with the combined Fundamental and Third Harmonic Currents", Proceedings of 2001 Applied Power Electronics Conference, APEC'01, Sixteenth Annual IEEE, Vol.1, pp.392-398, (2001).

[32]   R. O. C. Lyra and T. A. Lipo, "Torque density improvement in a six-phase induction motor with third harmonic current injection", IEEE Trans. IAS. 38(5), pp. 1351-1360, (2002).

[33]   A. F. Volschenk, "Finite element analysis of a salient-pole generator feeding a rectifier load", Ph.D. dissertation. University of Cambridge, March 1993.

[34]   D. W. Novotny, T. A. Lipo. *Vector Control and Dynamics of AC Drives*. Oxford University Press Inc., New York, (1997).

[35]   X. Xu and D. W. Novotny, "Implementation of direct stator flux orientation control on a versatile DSP based system", IEEE Trans. IAS. 27 (4), pp. 694-700, (1991).

[36]   J. S. Lee, T. Takeshita and N. Matsui, "Stator-flux-oriented sensorless induction motor drive for optimum low-speed performance", IEEE Trans. IAS. 33 (5), pp. 1170-1176, (1997).

[37]   R. E. Betz. Notes on *Vector control of induction machines*. Department of Electrical and Computer Engineering, University of Newcastle, Australia, (1997).

[38]   P. C. Krause, O. Wasynczuk, S. D. Sudhoff, *Analysis of electric machinery and drive systems*. IEEE press. Wiley interscience. 2002.

[39]   Z. Chen and A. C. Williamson, "Simulation study of a double three phase electric machine", Proceedings of ICEM'98. Istanbul Turkey, vol.1, pp.215-220, (1998).

[40]   J. C. Salmon and B. W. Williams, "A split-wound induction motor design to improve the reliability of PWM inverter", IEEE Trans. IAS. 26 (1), pp.143-150, (1990).

[41]   O. Ojo and I. E. Davidson, "PWM-VSI inverter-assisted stand-alone dual stator winding induction generator", IEEE Trans. IAS. 36(6), pp. 1604-1610, (2000).

[42]   L. Hou, L. Zhou and L. Chen, "Modelling and simulation research of six-phase induction machine drive", Journal of system simulation (China)*,* vol. 16, pp. 1249-1253, (2004).

[43]   L. Chen, Research on the control strategy of the multiphase induction machine variable frequency drive, Ph.D. dissertation, Huazhong University of Science and technology, Wuhan, China, March 2003.

[44]   T. Mizuno, K. Tsuboi, I. Hirotsuka, S. Suzuki, I. Matsuda, and T.Kobayashi, "Basic Principle and Maximum Torque Characteristics of A Six-Phase Pole Change Induction Motor for Electric Vehicles", T. IEE. Japan, 116-D (3), pp. 256-264. March (1996).

[45]   T. Ashikaga, T. Mizuno, M. Mori, K. Nagayama, I, Matsuda and M. Date, "A control Method of an Inverter-Fed Six-phase Pole Change Induction motor for Electric vehicle", T. IEE. Japan, 117-D (6), pp. 511-517, June (1997).

[46]   C. Chan, J. Jiang, G. Chen and K. Chau, "A Novel Polyphase Multipole Squeare Wave Permanent Magnet Machine Drive for Electric Vehicles", IEEE Trans. IAS. 30 (5), pp. 1258-1266, (1994),

[47]   T. M. Roman, R. J. Kerkman, and D. leggate, "A simple on-line adoption for indirect field orientation of an induction machine", IEEE Trans. IAS. 27 (4), pp. 720-727, (1991).

[48]   P. C. Sen, *Principle of Electric Machine and Power Electronic*s, 2nd , John Wiley & Sons, Inc., Canada. (1997).

[49]   Y. Ai, M.J. Kamper, Y. Wang, and S. Yuan, "Torque performance investigation of double three-phase motor using special current waveform", Proc. 4th Int. Conf. on Power Electronics and Motion Control (IPEMC), Xian (China), pp. 1673-1678. Aug. 2004,

[50]   Y. Ai, M.J. Kamper and Y. Wang, "Investigation of air gap flux density and torque performance of six-phase induction motor with special phase current waveform", Proc. 8th Int. Conf. on Electrical Machines and Systems (ICEMS), Nanjing (China), pp 99-104, Sept. 2005,

[51]   N. Mohan, *Electric Drives* (an integrative approach), Mnpere, Minneapolis, MN 55414, USA, 2001.

[52]   M. J. Kamper, "Design optimisation of cageless flux barrier rotor reluctance synchronous machine", Ph.D. dissertation, University of Stellenbosch. Stellenbosch. (1996).

[53]   B, Heller and V. Hamata, *Harmonic field effects in the induction machines*, Elsevier (Amsterdam), 1997.

[54]   H. A. Toliyat, T. A. Lipo and J. White, "Analysis of a Concentrated Winding Induction Machine for Adjustable Speed Drive Applications – part I (Machine Analysis)", IEEE Trans. Energy Conv. vol. 6, pp. 679-683, (1991)

[55]   H. A. Toliyat and T. A. Lipo and J. White, "Analysis of a Concentrated Winding Induction Machine for Adjustable Speed Drive Applications – part II (Machine Design and Performance)", IEEE Trans. Energy Conv. vol. 6, pp. 684-692, (1991)

[56]   Dec. 1991, H. A. Toliyat and T. A. Lipo, "Analysis of Concentrated Winding Induction Machines for Adjustable Speed Drive Applications-Experimental Results", IEEE Trans. Energy Conv. vol. 9, pp. 695-700, (1994).

[57]   H. A. Toliyat, "Analysis and Simulation of Five-Phase Variable Speed Induction Motor Drives Under Asymmetrical Connections", IEEE Trans. Power Electronics, vol. 13, pp. 748-756, (1998).

[58]   M. Osama, T. A. Lipo, "Modelling and Analysis of a Wide-Speed-Range Induction Motor Drive Based on Electronic Pole Changing", IEEE Trans. IAS. 33 (5), pp. 1177- 1184, (1997).

[59]   S. Williamson, T. J. Flack and A. F. Volchenk, "Representation of Skew in Time-Stepped Two-Dimension Finite Element Models of Electrical Machines", IEEE Trans. IAS., 31 (5), pp. 1009-1015, (1995).

[60]   A. A. Abdel-razek, J. L. Coulomb and J. C. Sabonnadiere, "Conception of an air-gap element for the dynamic analysis of the electromagnetic field in electric machine", IEEE trans. on Magnetics. 18(2), pp. 655-659, (1982).

[61]   T. J. Flack, A. F. Volschenk, "Computational aspects of time-stepping finite-element analysis using airgap element", ICEM (1994).

[62]   R. O. C. Lyra, Torque density improvement in a six-phase induction motor with third harmonic current injection, Ph.D. dissertation, University of Wisconsin-Madison, 2002.

[63]   User's Guide of TMS320c3x Floating-point DSP, Houston, Texas Instruments Inc., 1997.

[64]   http://dsp.ti.com/ Texas instruments DSP village, October 2005

[65]   http://www.altera.com/literature/lit-cyc.jsp Altera Cyclone FPGA. October 2005

[66]   V. Ambrozic, R. Fiser and D. Nedeljkovic, "Direct Current Control- A New Current Regulation Principle", IEEE Trans, Power Electronics, 18 (1), pp. 495-503, Jan. (2003).

[67]   J. Holtz, B. Beyer, "The Trajectory Approach-A New Method for Minimum Distortion PWM in Dynamic High-Power Drives", IEEE Trans, IAS. 30 (4), pp. 1048-1057, (1994).

[68]   J. Holtz, B. Beyer, "Fast Current Trajectory Tracking Control Based on Synchronous Optimal Pulsewidth Modulation", IEEE Trans, IAS. 31 (5), pp. 1110-1120, (1994).

[69]   M. P. Kazmierkowski and L. Malesani, "Current Control techniques for Three-phase Voltage-Source PWM Converters: A Survey", IEEE Trans, Industrial Electronics, 45 (5), pp. 691-703, (1998).

[70]   S. Buso, L. Malesani and P. Mattavelli, "Comparison of Current Control Techniques for Active Filter Application", IEEE Trans, Industrial Electronics, 45(5), pp. 722-729, (1998).

[71]   S. Buso, S. Fasolo, L. Malesani and P. Mattavelli, "A Deat-Beat Adaptive Hysteresis Current Control", IEEE Trans, IAS, 36 (4), pp. 1174-1180, (2000).

[72]   D. M. Brod and D. W. Novotny, "Current Control of VSI-PWM Inverters", IEEE Trans. IAS. vol. IA-21 (4), pp.562-570, May/June (1985).

[73]   B. Kwon, T. Kim and J. Youm, "A Novel SVM-Based Hysteresis Current Controller", ", IEEE Trans, Power Electronics, 13 (2), pp. 297-307, March. (1998).

[74]   Ch. Pan and T. Chang, "An Improved Hysteresis Current Controller for Reducing Switching Frequency", IEEE Trans, Power Electronics, 9 (1), pp. 97-104, Jan. (1994)

[75]   P. Wipasuramonton, Z. Zhu and D. Howe, "Improved Current-Regulated Delta Modulator for Reducing Switch Frequency and Low-Frequency Current Error in

Permanent Magnet Brushless AC Drives", IEEE Trans, Power Electronics, 20 (2), pp. 475-484, March. (2005).

[76]   M. G. Say, Alternating circuit machines, IBM press, Roman, 1976.
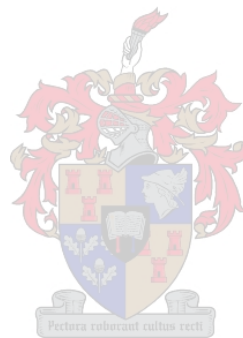
A   DESIGN SPECIFICATIONS OF THE SIX-PHASE INDUCTION MOTOR

A.1   Design of the stator winding

A standard 4-pole, 2.2 kW, 3-phase cage induction machine with 36 stator slots and 28 rotor slots is used in the study. The 3-phase, 4-pole stator winding of this machine has been modified to a 6-phase, 2-pole stator winding. The cage winding has been replaced by a 14-phase wound rotor winding.

A.1.1   *Number of slots of per pole per phase*

The number of stator slots per pole per phase is 3 ($36/(6 \times 2)$). The per phase circuit diagram with three coils per phase is shown in Fig. A.1. The winding layout is shown in Fig. A.2.
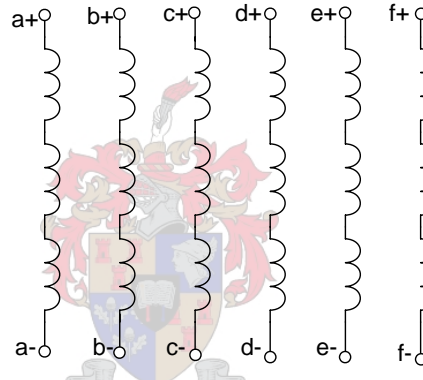

Fig. A.1. Per phase circuit diagram.
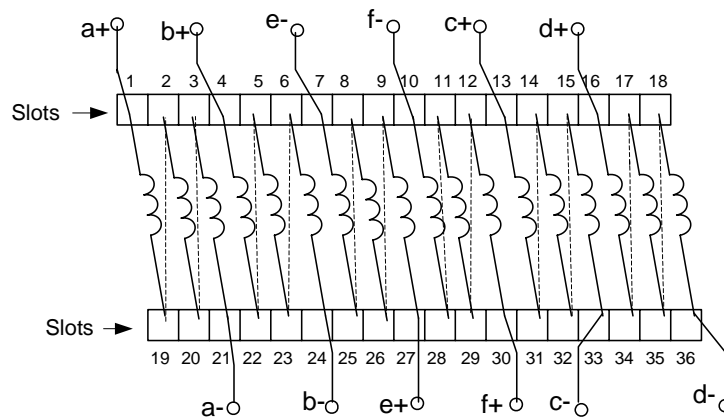

Fig. A.2. Six-phase stator winding layout in 36 slots.

A.1.2   *Turns per coil*

The turns per coil, N_{coil}, can be determined by using the following formula [76]:

$$E = 4.44 f \cdot N_{coil} \cdot K_w \cdot \phi_p , \qquad (A.1)$$

where: E is the rms value of the induced voltage, normally close to the supply voltage;

f is the stator voltage frequency;

K_w is the winding factor, which normally is between 0.85 – 0.95;

ϕ_p is the air gap flux per pole which is calculated by

$$\phi_p = \int_{-\frac{\pi}{2}}^{\frac{\pi}{2}} B(\theta)lr \cdot d\theta \ , \tag{A.2}$$

where $B(\theta) = B_m \cos\theta$.

For the specific induction machine the parameters and dimensions are given in Table A.1. The flux density B_m is the peak value of the assumed sinusoidal air gap flux density.

Table A.1. Parameters and dimensions of 6-phase induction machine.

	f	r	l	B_m	K_w
Value	50 Hz	0.049 m	0.128 m	0.57 T	0.9

Hence the flux per pole can be calculated as

$$\phi_p = 2 \cdot B_m \cdot r \cdot l = 2 \times 0.57 \times 0.049 \times 0.128 = 0.00715 \text{ Wb.}$$

As the sum of the six-phase currents of the IDCM is not zero at any time, each phase winding needs to be supplied and controlled by a full bridge power converter as shown in Fig. A.3. From this, thus, the rated rms supply voltage across a phase coil is $500/3 \ /\sqrt{2} = 117.9$V, which is assumed to be equal to the rms induced voltage E.
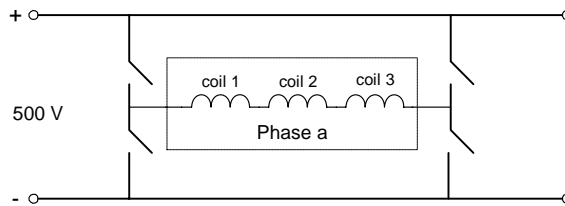

Fig. A.3. Phase winding *a* of six-phase induction motor supplied by a full bridge converter.

From eqn (A.1),
$$N_{coil} = \frac{E}{4.44\,fK_w\phi_p} \ .$$

(A.3)

Therefore, the number of turns per coil is

$$N_{coil} = \frac{E}{4.44 f\, K_w\, \phi_p} = \frac{117.9}{4.44 \times 50 \times 0.9 \times 0.00715} = 82.5 \approx 83 \text{ turns.}$$

A.1.3 *Cross-section area of stator slot*

The shape and dimensions of the stator slot are shown in Fig. A.4.
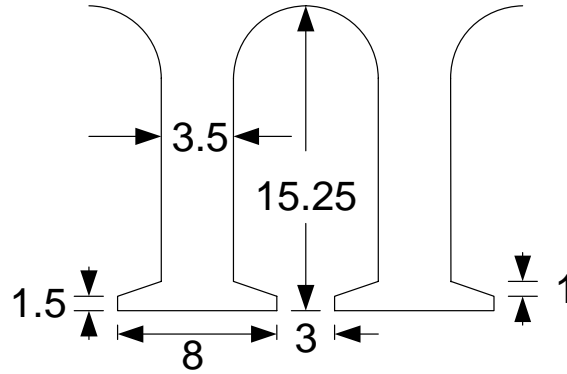

Fig. A.4. Shape of stator slot and dimensions in mm.

By subtracting the slot insulation thickness of 0.5 mm, the cross-section area of the slot can be roughly calculated as

$$S_{slot} = 6 \times 8.75 \times 10^{-6} + \frac{\pi}{2} \cdot (3 \times 10^{-3})^2 = 66.6 \times 10^{-6} m^2 \quad .$$

A.1.4 *Calculation of diameter of stator conductor*

With a fill factor of 0.5 and the number of turns per coil in a slot equal to 83, the diameter of the stator conductor can be determined by eqn (A.4)

$$d^2 \cdot n = S_{slot} \cdot k_{fill\ factor} \tag{A.4}$$

Therefore

$$d = \sqrt{\frac{S_{slot} \cdot K_{fillfactor}}{N_s}} = \sqrt{\frac{66.6 \times 10^{-6} \times 0.5}{83}} = 0.63 \times 10^{-3} \approx 0.6 \times 10^{-3} m$$

$$= 0.6 \text{ mm} .$$

From the above, some design parameters of the stator are thus:

Number of stator slots = 36

Number of coils per phase = 3

Number of turns of per coil = 83

Diameter of stator conductor = 0.6 mm

A.2   **Design of rotor winding**

In order to measure the induced voltage and current of the rotor winding, a special wound rotor is designed and built. Two rotor phases are connected to slip rings for the purpose of measurement. There are 28 slots in the rotor. Fig. A.5 shows the dimensions of these slots.
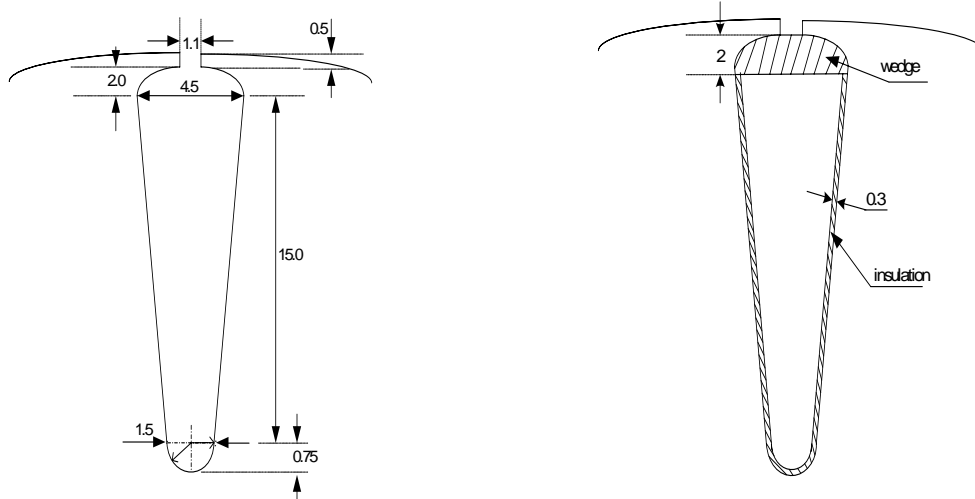

Fig. A.5. Rotor slot dimensions in mm.

According to the dimensions given in Fig. A.5, the cross-section area of the rotor slot is calculated as

$$S_{rslot} = 3.14 \times (1.5 - 2 \times 0.3)^2 \times \frac{1}{2} + \frac{(4.5 - 2 \times 0.3) + (1.5 - 2 \times 0.3)}{2} \times 15$$
$$= 36.3 \quad mm^2 .$$

The number of turns per coil of the rotor, N_r, is determined from eqn (A.4) by selecting the diameter of the rotor conductor. The results are shown in Table A.2.

Table A.2. Coil turns for per slot.

d (mm)	N_r (turn)
0.6	50
0.7	37
0.8	28
0.9	22
1.0	18
1.1	15

Some of the rotor design parameters are thus:

   Number of rotor slots = 28

   Number of turns per coil = 28

   Diameter of the rotor conductor = 0.8 mm

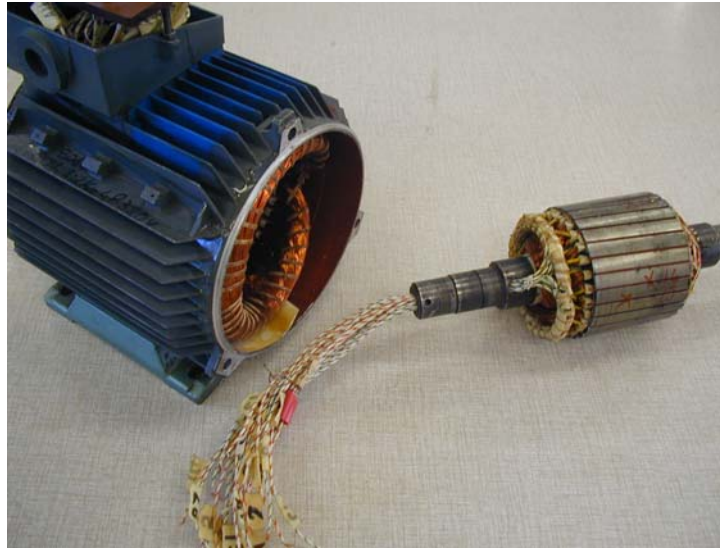Photos of the stator, rotor and assembled motor are shown in Figs. A.6 – A.8.
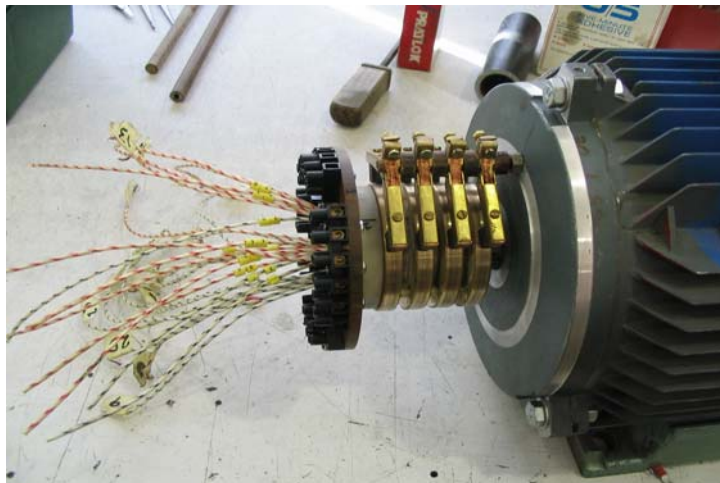

Fig. A.6. Stator and rotor of six-phase IDCM.

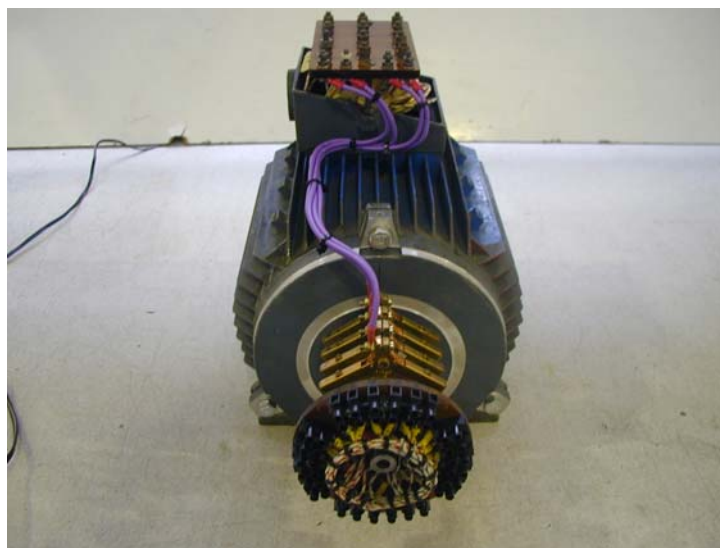Fig. A.7. Assembled six-phase IDCM (1).

Fig. A.8. Assembled six-phase IDCM (2).

B   CALCULATION OF STATOR TORQUE CURRENT AND ROTOR CURRENT

According to the rotor winding design in Appendix A the values used to calculate the rotor phase induced voltage are given in Table B.1. The rotor per phase induced voltage can be calculated by eqn (3.11) and the results are shown in Fig. 3.14.

Table B.1. Values used to calculate the rotor phase induced voltage.

B (T)	N_r (turn)	l (mm)	r (mm)
0.47	28	128	49

In order to calculate the flat-topped amplitude of the induced rotor current, I_r, it is necessary to know the rotor phase resistance. The shape of one rotor coil is shown in Fig. B.1.
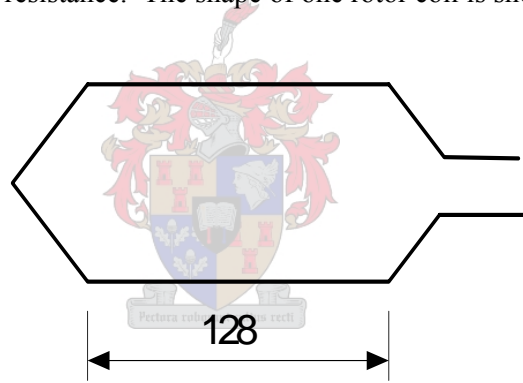

Fig. B.1. Shape of rotor phase coil.

The total length of one turn of the rotor phase coil of Fig. B.1 is estimated as 456 mm. The resistance per turn is calculated by using eqn (B.1)

$$r = \rho \frac{l'}{S},$$ (B.1)

where, l' is the length per turn of the rotor coil;

   S is the cross-sectional area of the rotor conductor equal 0.5024 mm^2;

   ρ is the resistivity for copper equal to 1.69×10^{-8} Ωm at 25 °C.

The per phase rotor resistance, r_{eq}, is thus calculated as

$$r_{eq} = N_r \ r = 28 \ r \ .$$ (B.2)

The value of this resistance is calculated as $r_{eq} = 0.46$ Ω.

The rotor induced current amplitude, I_r, and the stator torque current are calculated by using eqns (3.12) and (3.20), with the results given in Table B.2.

Table B.2. Torque current and rotor current versus slip speed.

Slip speed (rpm)	Torque current (I_T) (A)	Rotor current (I_r) (A)
30	0.44	1.12
60	0.88	2.24
90	1.32	3.36
120	1.76	4.48
150	2.2	5.6
180	2.64	6.72
210	3.08	7.84
240	3.52	8.96
270	3.96	10.08
300	4.4	11.2

C CALCULATION OF FIELD CURRENT

C.1 Dimensions of the six-phase induction motor

The dimensions of the six-phase induction motor are shown in Figs.C.1 – C.3.

Fig. C.1. Dimensions of stator and rotor core.

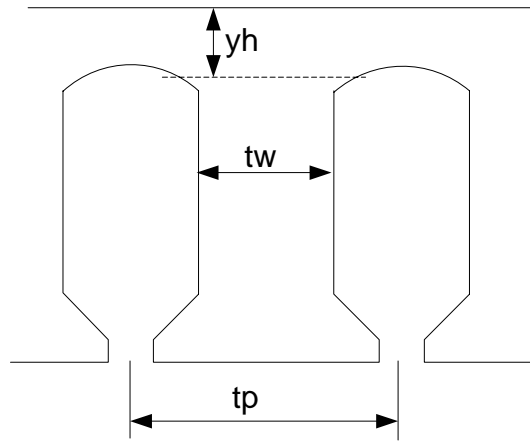

Fig. C.2. Shape of the stator slot.
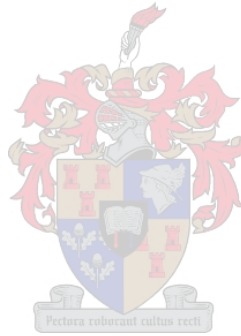
Fig. C.3. Stator slot dimension parameters.

C.2 Calculation of field current versus airgap flux density

To calculate the field current versus air gap flux density, the magnetic circuit is divided into nine regions as shown in Fig. 3.15. In the following analysis the MMF-drops in the different regions are calculated.

- Air gap

REGION 5

Region 5 is the air gap as shown in Fig. 3.15. If the air gap flux density is B, then the MMF drop in the air gap is

$$F_{air} = \frac{B \, k_c \, l_g}{\mu_0},$$ (C.1)

where k_c is the Carter factor;

l_g is the length of the airgap, which is equal to 0.5 mm;

μ_0 is the absolute permeability.

- Stator side

REGION 4

Region 4 as shown in Fig. 3.15 is the stator tooth. The MMF drop is determined first by calculating the flux density in region 4 as

$$B_4 = B(\frac{t_{ps}}{t_{ws} K_s}) \; .$$ (C.2)

where K_s is stacking factor

With B_4 known, the magnetic field strength, H_4, can be obtained from the B/H – curve of the lamination steel. The tooth MMF drop is then calculated as

$$F_4 = H_4 \, l_4 \ , \tag{C.3}$$

where l_4 is the tooth length.

REGION 3

Region 3 as shown in Fig. 3.15 is at the top of the stator tooth. The flux density is

$$B_3 = B \ . \tag{C.4}$$

The MMF drop can be calculated using the same procedure as for region 4 as

$$F_3 = H_3 \, l_3 \ , \tag{C.5}$$

where l_3 is the magnetic route length of region 3.

REGION 2

Region 2 as shown in Fig. 3.15 is the yoke region. In this region the flux increases linearly from $\phi/4$ to $\phi/2$, and the average value is $3\phi/8$. The flux per pole is determined by

$$\phi = B \, \tau_p \, l_{stack} \ , \tag{C.6}$$

where τ_p is pole pitch in the air gap and is given by

$$\tau_p = \frac{d_r \, \pi}{4} \ , \tag{C.7}$$

where d_r is the rotor outside diameter and l_{stack} is the motor stack length. The flux density, B_2, is given by

$$B_2 = \frac{3\phi/8}{yh \, l_{stack} \, K_s} = \frac{3B\tau_p \, l_{stack}}{8 \, yh \, l_{stack} \, K_s} = \frac{3B \, \tau_p}{8 \, yh \, K_s} \ , \tag{C.8}$$

where yh is the yoke height. The MMF drop can then be calculated using the same procedure as for region 4 namely

$$F_2 = H_2 \, l_2 \ , \tag{C.9}$$

where l_2 is the yoke magnetic route length of region 2.

REGION 1

Region 1 as shown in Fig. 3.15 is also the stator yoke. The flux density is given by

$$B_1 = \frac{\phi/2}{yh \, l_{stack} \, K_s} = \frac{B \, l_{stack} \tau_p}{2 \, yh \, l_{stack} \, K_s} = \frac{B \, \tau_p}{2 \, yh \, K_s} \ . \tag{C.10}$$

The MMF drop can be calculated using the same procedure as for region 4 namely

$$F_1 = H_1 \, l_1 \ , \tag{C.11}$$

where l_1 is magnetic route length of region 1.

- Rotor side

REGION 6

Region 6 as shown in Fig. 3.15 is the rotor tooth. The flux density is calculated by

$$B_6 = B\left(\frac{t_{pr}}{t_{wr} K_s}\right) \ . \tag{C.12}$$

The MMF drop can be calculated using the same procedure as for region 4 namely

$$F_6 = H_6 l_6 , \tag{C.13}$$

where l_6 is the length of region 6.

REGION 7

Region 7 as shown in Fig. 3.15 is below the rotor tooth. The flux density is

$$B_7 = B \ . \tag{C.14}$$

The MMF drop can be calculated using the same procedure as for region 4 namely

$$F_7 = H_7 l_7 , \tag{C.15}$$

where l_7 is the magnetic route length of region 7.

REGION 8

Region 8 as shown in Fig. 3.15 is the rotor yoke region. The flux density is the same as in region 2 and is given by

$$B_8 = \frac{3\phi/8}{yhr \, l_{stack} K_s} = \frac{3B\tau_p \, l_{stack}}{8 \, yhr \, l_{stck} \, K_s} = \frac{3B \, \tau_p}{8 \, yhr K_s} , \tag{C.16}$$

where *yhr* is the height of the rotor yoke. The MMF drop can be calculated using the same procedure as for region 4 namely

$$F_8 = H_8 \, l_8 , \tag{C.17}$$

where l_8 is the yoke length of region 8.

REGION 9

Region 9 as shown in Fig. 3.15 is also part of the rotor yoke region. The flux density is the same as in region 1 and is given by

$$B_9 = \frac{\phi/2}{yhr \, l_{stack} \, K_s} = \frac{B \, l_{stack} \, \tau_p}{2 \, yhr \, l_{stack} \, K_s} = \frac{B \, \tau_p}{2 \, yhr \, K_s} , \tag{C.18}$$

where *yhr* is the height of the rotor yoke. The MMF drop can be calculated using the same procedure as for region 4 namely

$$F_9 = H_9 \, l_9 , \tag{C.19}$$

where l_9 is yoke length of region 9.

The total MMF drop, F_{tot}, is given by

$$F_{tot} = \sum_{i=1}^{9} F_i \quad . \tag{C.20}$$

- Calculation of total MMF

The total MMF produced by the field windings is

$$F'_{tot} = 2 \times N_s \, I_f \, K_w \tag{C.21}$$

where, N_s is the number of turns per stator phase (249);

   I_f is the field current amplitude;

   K_w is winding factor; with three phases used as field phases and with full-pitch coils,
   it can be determined by

$$K_w = \frac{\sin(na/2)}{n \, \sin(a/2)} \quad , \tag{C.22}$$

where a is the angle between two adjacent slots, i.e. $a = 10°$, and n is slots per pole per phase,
i.e. $n = 9$. From this the winding factor is

$$K_w = \frac{\sin(9 \times 10° / 2)}{9 \sin(10° / 2)} = \frac{0.707}{9 \times 0.087} = 0.903 \; .$$

From eqn (C.21), thus, $F'_{tot} = 2 \times 3 \times 83 \times 0.903 \times I_f = 449.7 I_f$.

The field current can be determined from eqn (C.20) and by using

$$F_{tot} = F'_{tot} \quad . \tag{C.23}$$

- Calculation of Carter's factor

Carter's factor, k_c, in eqn (C.1) is given by [53]

$$k_c = k_{cs} \, k_{cr} \quad , \tag{C.24}$$

where

$$k_{cs} = \frac{t_{ps}}{t_{ps} - \gamma_s \, l_g} \quad \text{(stator)} \tag{C.25}$$

$$k_{cr} = \frac{t_{pr}}{t_{pr} - \gamma_r \, l_g} \quad \text{(rotor)} \; . \tag{C.26}$$

The parameters used in eqns (C.25) and (C.26) are shown in Figs. C.1, C. 2, C. 3 and C.4, and

$$\gamma = \frac{4}{\pi}\{ \frac{t_w}{2l_g} \tan^{-1} \frac{t_w}{2l_g} - \ln \sqrt{[1+(\frac{t_w}{2l_g})^2]} \} \ . \tag{C.27}$$

For the stator side, k_{cs} is calculated as follows:

$t_{ws} = 6$ mm and $l_g = 0.5$ mm

$$\frac{t_w}{l_g} = \frac{6}{0.5} = 12 > 1$$

$$\gamma = \frac{(\frac{t_w}{l_g})^2}{5+\frac{t_w}{l_g}} = \frac{10^2}{5+10} = 6.67$$

$t_{ps} = 10$ mm

$$k_{cs} = \frac{t_{ps}}{t_{ps} - \gamma_s \ l_g} = \frac{10}{10 - 6.67 \times 0.6} = 1.67 \ .$$

For the rotor side, k_{cr} is calculated as follows:

$$\frac{t_w}{l_g} = \frac{3.75}{0.6} = 6.25 > 1$$

$$\gamma = \frac{(\frac{t_w}{l_g})^2}{5+\frac{t_w}{l_g}} = \frac{3.75^2}{5+3.75} = 1.61$$

$t_{pr} = 5 + 3.73 = 8.75$ mm

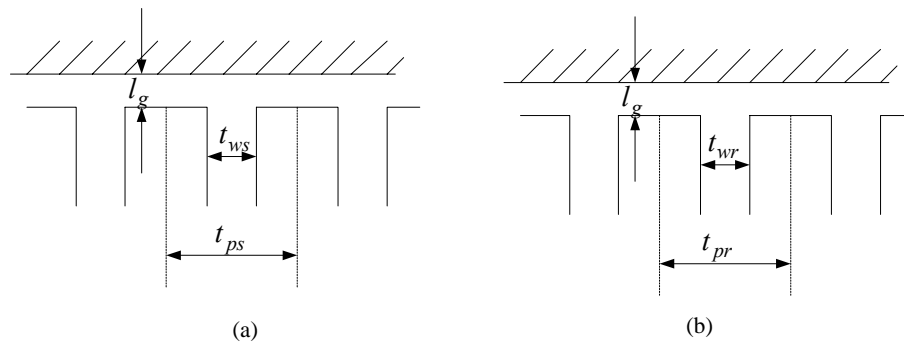$$k_{cr} = \frac{t_{ps}}{t_{ps} - \gamma_s \ l_g} = \frac{8.75}{8.75 - 1.61 \times 0.6} = 0.90 \ .$$

Fig. C. 4. Parameters of stator and rotor sides: (a) stator side and (b) rotor side.

D   EXPERIMENTAL SYSTEM SETUP

An experimental setup is built to test the proposed IDCM technique.

D.1   Machine test setup

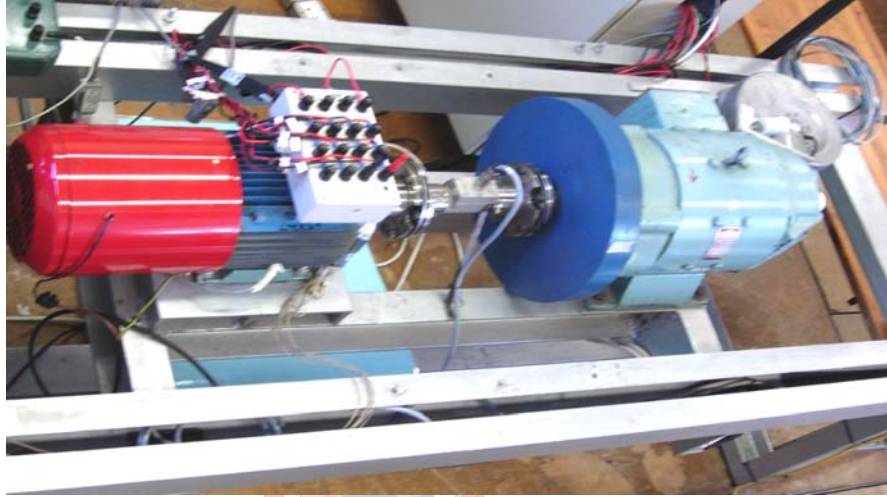A photo of the six-phase IDCM test setup is shown in Fig. D. 1.

Fig. D.1. Six-phase IDCM test setup.

The equivalent inertia can be evaluated by considering the flywheel and rotors of the six-phase
IDCM and dc motor as shown in Fig. D.1. The flywheel is the major part in this rotating system,
so the inertia of the flywheel is calculated as

$$J_{flywheel} = \frac{1}{2}[M_{flywheel}(r_{flywheel})^2]$$

$$M_{flywheel} = pv = p\pi r_{flywheel}^2\, l_{stack\ flywheel} = 7850 \times \pi \times (0.184)^2 \times 0.084 = 39.25\, kg$$

$$J_{flywheel} = \frac{1}{2}39.25 \times (0.184)^2 = 0.66\, kg\ m^2$$

When taking the rotors of the six-phase IDCM and the dc motor into consideration, the equivalent
inertia is estimated as J = 0.7 Kg m² and the friction coefficient as β_{eq}=0.01 Nm/(rad/sec).

Photos of the torque measurement hardware used are shown in Fig. D.2.

|(a) Torque transducer|(b) Signal amplifier|

Fig. D.2. Torque measurement.

D.2   Power inverter

A photo of the PS21867 module used for the six-phase full bridge is shown in Fig. D.3. The application circuit of the PS21867 module is shown in Fig. D.4.
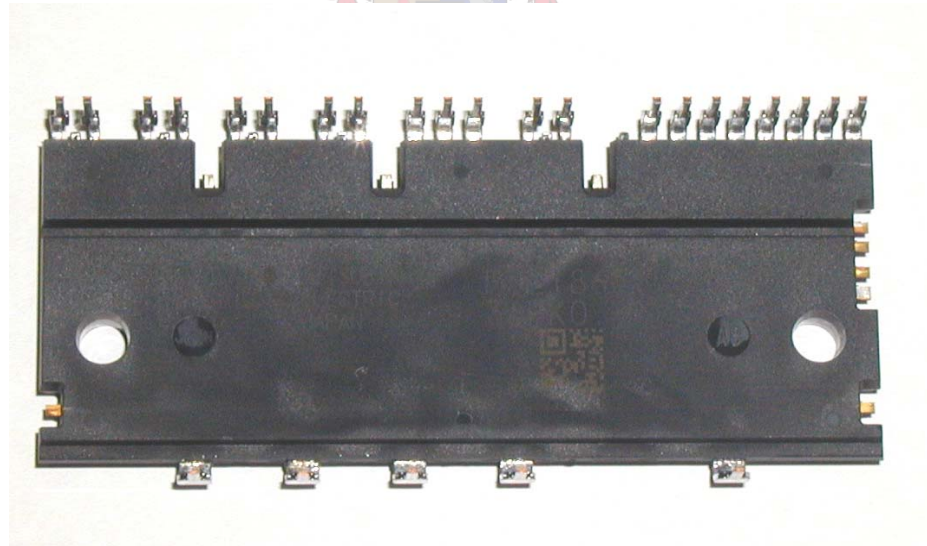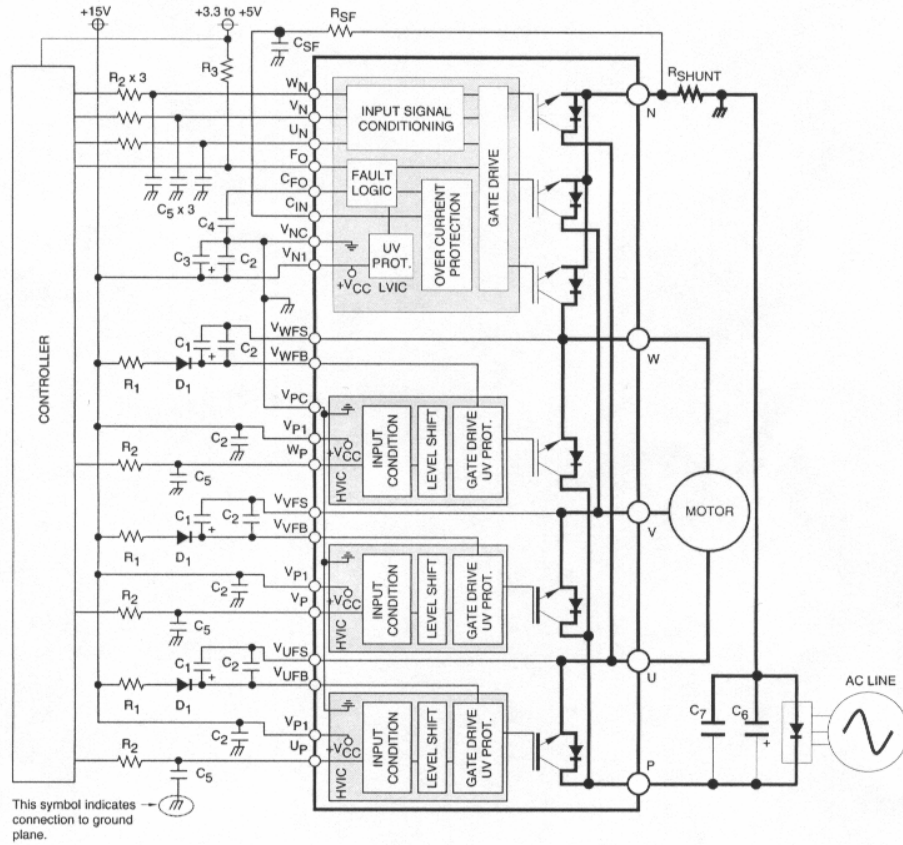

Fig. D.3. PS21867 three-phase module.

Fig. D. 4. Application circuit of the PS21867 module.

A photo of the driver circuit board with its components is shown in Fig. D.5. Photos of the six-phase full bridge inverter are shown in Fig. D.6.
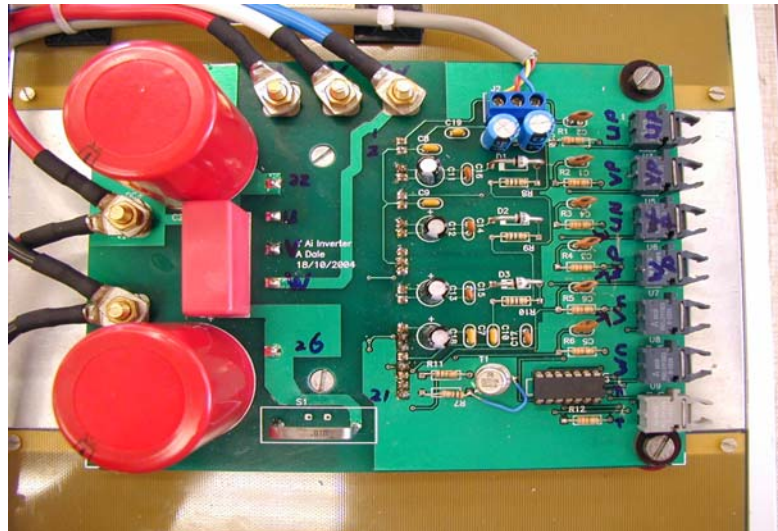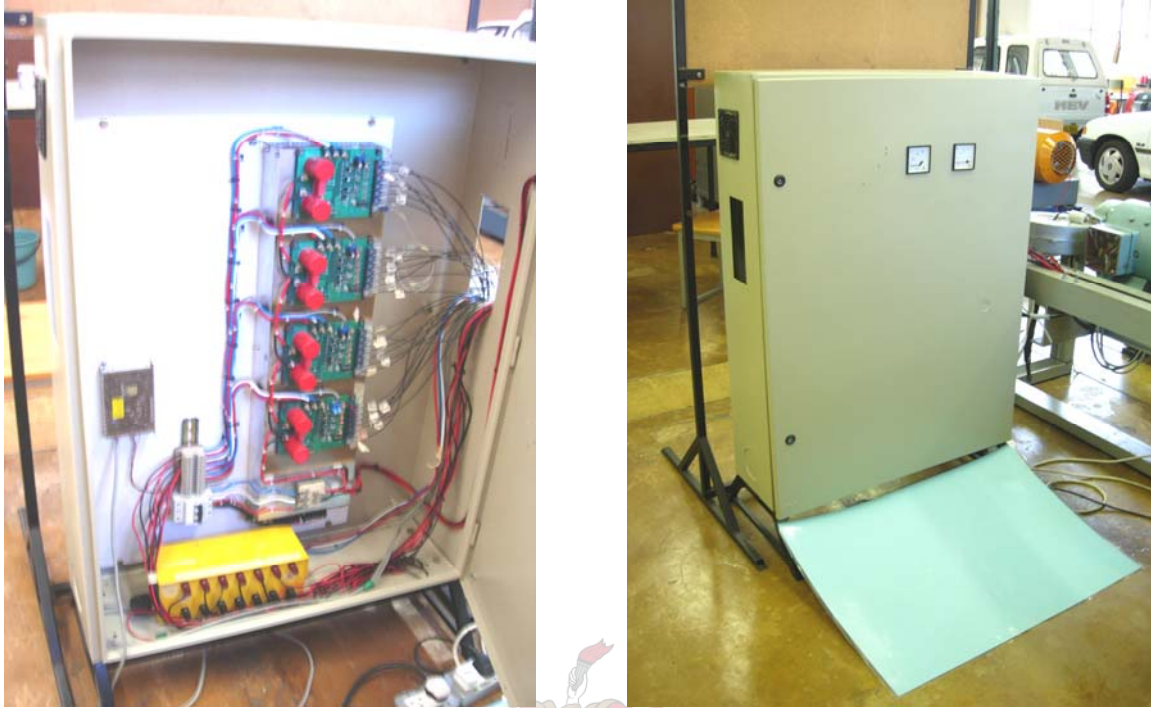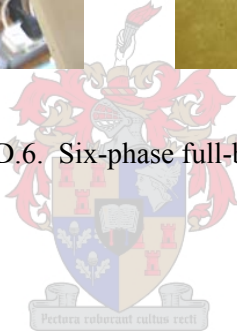

Fig. D.5. Driver circuit board.

133

(a) Inverter core   (b) Inverter outline

Fig. D.6. Six-phase full-bridge inverter.

D.3   DSP controller

The IDCM control is implemented on a digital signal processor (DSP) controller [63 - 65]. A brief description of the main parts of the DSP controller is as follows.

D.3.1   DSP chip

The DSP chip selected is the TMS320 VC33 DSP, which is a 32–bit, floating-point processor manufactured in 0.18-µm four-level-metal CMOS technology. It can execute up to 150 million floating-points per second (MFLOPS) and it can also perform parallel multiplication and ALU operations on integer or floating-point data in a single cycle. In this specific DSP controller, the DSP chip mainly performs those functions that are to produce the six-phase current waveforms, execute the speed PI controller and deliver/receive data to and from the computer.

D.3.2   FPGA chip

The FPGA chip selected is the Altera Cyclone EP1c60240CB chip, which is based on a 1.5V, 0.13-μm, all-layer copper SRAM process, with densities up to 20060 logic elements (LE's) and up to 288 Kbits of RAM. In this specific DSP controller, the FPGA chip mainly performs the following functions: reads the six-phase current data from the A/D converter; executes the hysteresis controller; calculates the duty cycle of the PWM signals and writes the PWM signals to the EPLD.

D.3.3   EPLD chip

The EPLD chip selected is the EPM3064 chip, which has programmable I/O architecture with up to 36 inputs and 24 outputs. In the DSP controller, the EPLD chip mainly performs the function of increasing the PWM signals output pins because the FPGA does not have enough pins for assigning the PWM signals to every power switch device. The EPLD also receives error signals from the inverter [over-voltage and over-current signals] in order to protect the power inverter by locking the PWM signals.
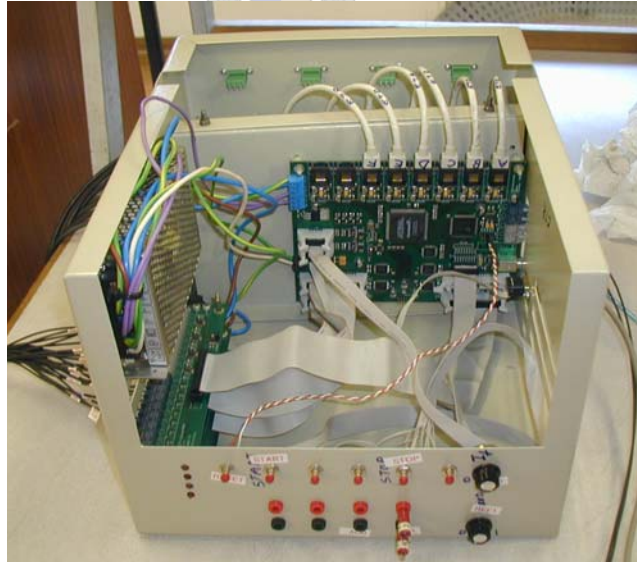
A photo of the DSP controller is shown in Fig. D.7.

Fig. D.7. DSP controller.

D.4   Control algorithm

To develop the control software a C-language compiler is used to generate the code. Although a high level language is used, the knowledge of the processor's architecture is also important to generate an acceptable code. Fortunately, the DSP chip chosen is a floating point processor; with floating point it is very convenient to deal with variables with fractional numbers, and these variables can directly be used in the programming and do not need any translation.

Based to the control block diagram of Fig. D.8, the flowchart of the control block diagram is composed basically of three modules as shown in Fig. D.9. Module one is the main program responsible for the initialisation of all variables and the monitoring of the control process. Module two, which is a subroutine namely *isr_co*, is responsible for the sampling data of the rotor position and six-phase currents, and output data to the DAC for display. Module three, which is a subroutine namely *isr_c1*, is also responsible for the sampling data of the rotor position and six-phase currents, but without the function of outputting data to the DAC. These two modules sample data every 100 μs alternatively for the control calculation.
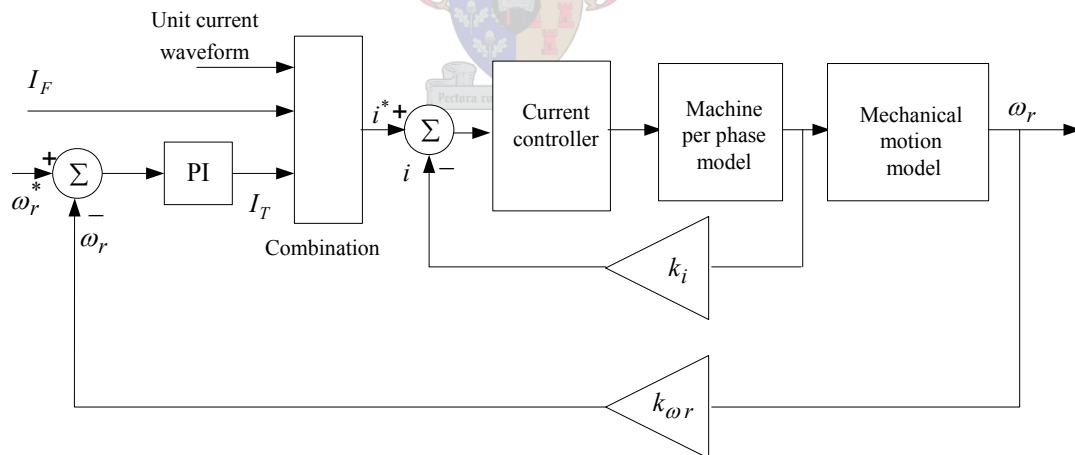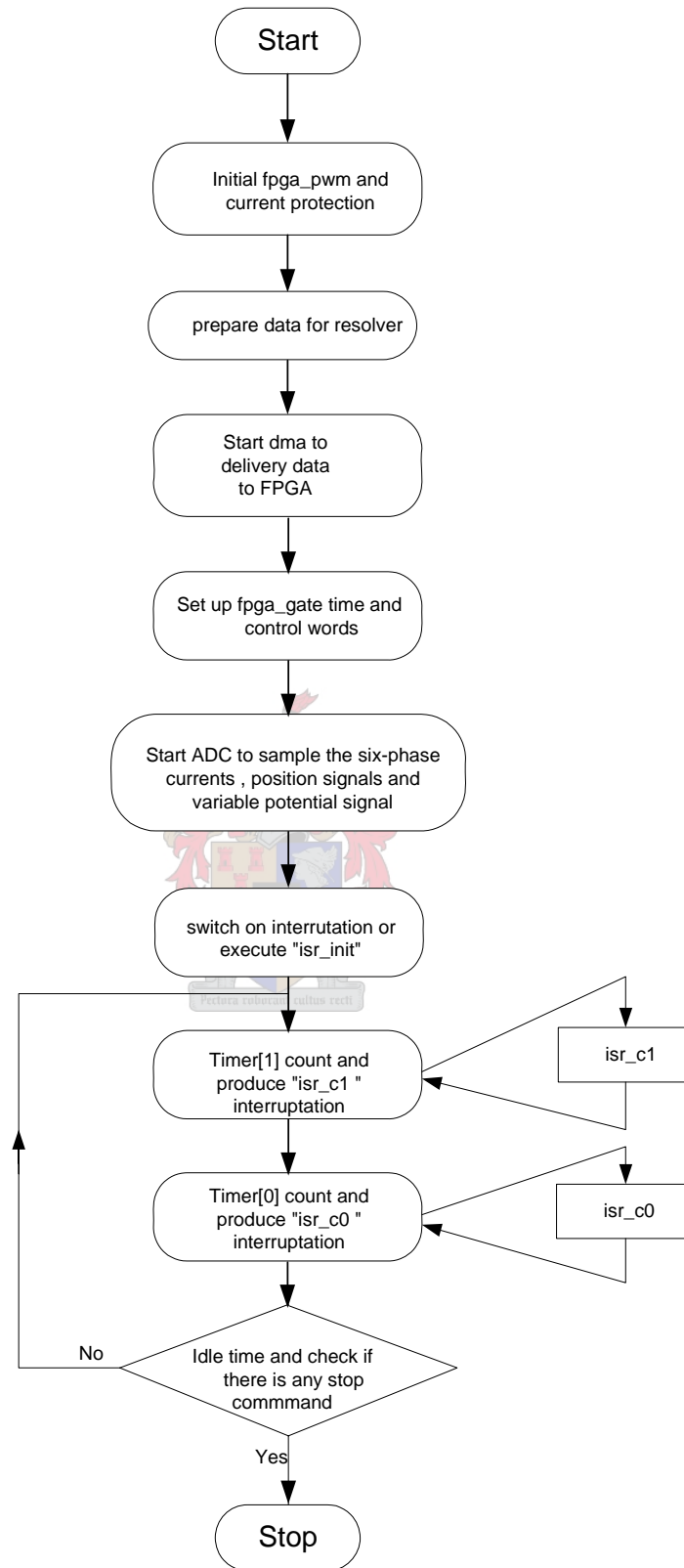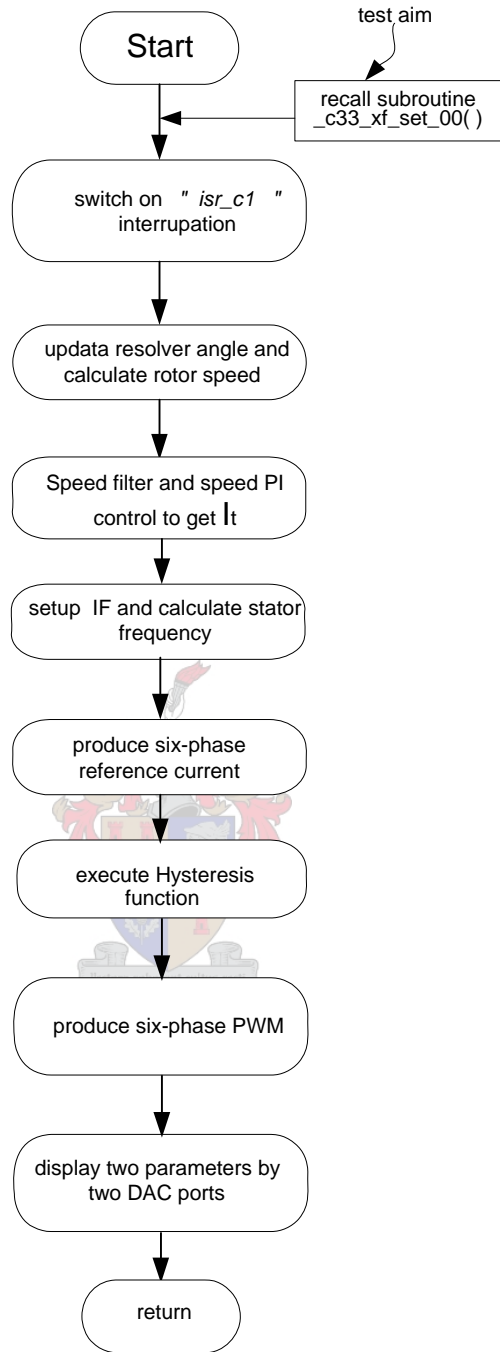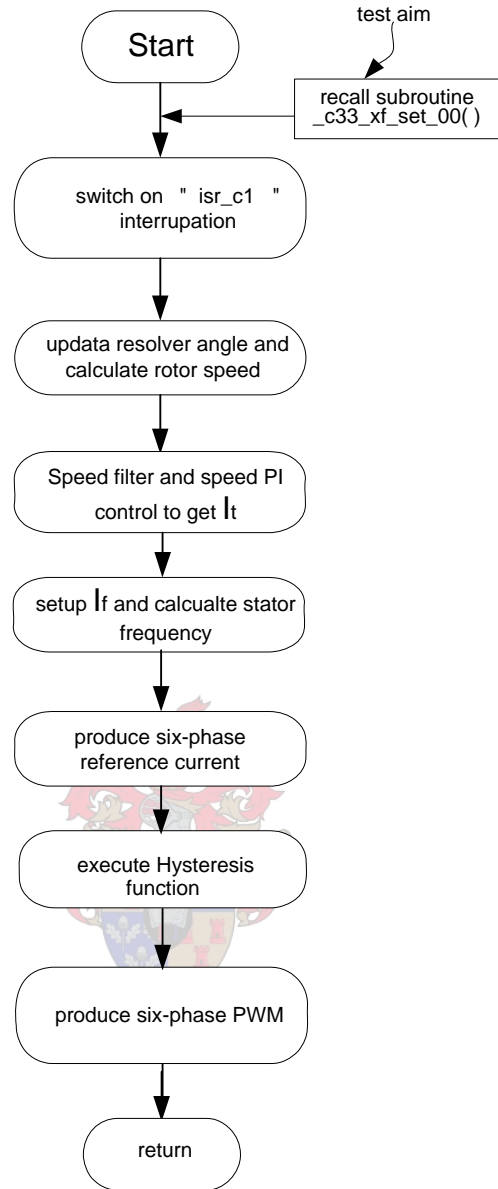

Fig. D. 8. Control block diagram.

(a) Module one – main program.

137

Start

test aim

recall subroutine
_c33_xf_set_00( )

switch on *" isr_c1 "*
interrupation

updata resolver angle and
calculate rotor speed

Speed filter and speed PI
control to get It

setup IF and calculate stator
frequency

produce six-phase
reference current

execute Hysteresis
function

produce six-phase PWM

display two parameters by
two DAC ports

return

(b) Module two - subroutine *isr_c0* flow chart

(c) Module three - subroutine *isr_c1* flow chart

Fig. D. 9. Control block diagram for the IDCM drive.

D.5   Digital hysteresis current controller

A per phase power circuit of the IDCM drive is shown in Fig. D.10. Bipolar switching control is used in the six-phase power inverter. The control of the per phase full bridge inverter allows the motor winding current to flow in both directions.

The function of the digital hysteresis controller is implemented in the DSP controller by software. The current waveform with the hysteresis band is shown in Fig. D.11. The procedure and the algorithm of the hysteresis current controller are as follows:

(i)   The FPGA samples at 250 kHz (4 µs) the real six-phase IDCM currents*;*

(ii)   The FPGA then compares the real sampled motor current with an upper band current and/or lower band current to make a decision:

- if the real current exceeds the upper band current, switches S_1 and S_2 of Fig. D.10 are turned off and switches S_3 and S_4 are turned on after an interval of dead time.

- if the real current crosses the lower band current, switches S_3 and S_4 are turned off and switches S_1 and S_2 are turned on after an interval of dead time;

- if the real current is between the upper band and lower band currents, the switches remain in their previous switching states.
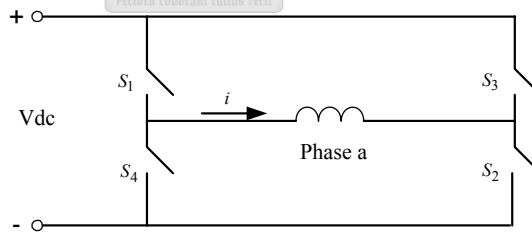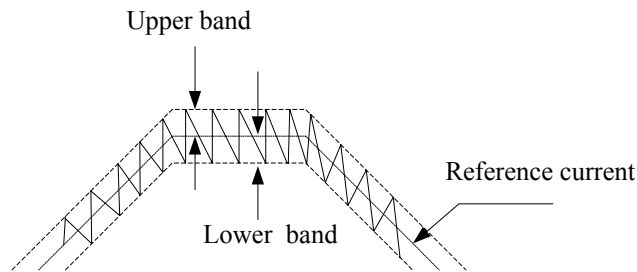

Fig. D.10. Per phase power inverter circuit.

Fig. D.11. Reference current waveform with hysteresis band.